elektronisches dokument
ULB Sachsen-Anhalt

Single Molecule Fluorescence Detection in Nanoscale Confinement

Dissertation

zur Erlangung des akademischen Grades

Doctor rerum naturalium (Dr. rer. nat.)

vorgelegt der
Mathematisch-Naturwissenschaftlich-Technischen Fakultät
(mathematisch-naturwissenschaftlicher Bereich)
der Martin-Luther-Universität Halle-Wittenberg

von Herrn Johannes Hohlbein

geb.: 20. 05. 1980 in: Wippra, Deutschland

Gutachter:

1. Prof. Dr. U. Gösele
2. Prof. Dr. C. Hübner
3. Prof. Dr. J. Lupton

Halle (Saale), am 31. 03. 2008

urn:nbn:de:gbv:3-000013420
[http://nbn-resolving.de/urn/resolver.pl?urn=nbn%3Ade%3Agbv%3A3-000013420]

Contents

Nomenclature **1**

1 Introduction **2**

2 Single molecule spectroscopy: fundamentals and beyond **5**

2.1 The photophysics of single molecules 5

2.2 Single molecule detection in solution 7

2.3 Scanning confocal optical microscopy 8

2.4 Single pair fluorescence resonance energy transfer 10

2.5 Fluorescence correlation spectroscopy 14

2.6 Orientation determination: from 2-D to 3-D 18

2.7 Geometrical confinement of diffusion 20

3 Materials and methods **22**

3.1 Self-ordered porous alumina 22

3.2 The scanning confocal optical microscopy set-up 23

3.3 Fluorescent probes 25

3.4 Monte-Carlo simulations 25

4 Fluorescent molecules diffusing in confinement **29**

4.1 One dimensional diffusion in porous alumina 29

4.2 Objectives: water-immersion versus oil-immersion 35

4.3 1D-diffusion of eGFP: Changing pH-value 44

4.4 Monte-Carlo simulations of 1D and 3D diffusion 46

4.5 FRET in porous alumina 54

5 3D-orientation determination of single molecules **59**

5.1 Models and methods 59

5.2 Results of simulations 64

5.3 Experimental results 73

5.4 Discussion 84

6 Conclusion and outlook **86**

Bibliography **97**

Eidesstaatliche Erkärung 98

Curriculum vitae 99

Scientific contributions 100

Acknowledgment 102

Nomenclature

1D	one-dimensional
3D	three-dimensional
ACF	auto-correlation function
ALEX	alternating laser excitation
BSA	bovine serum albumine
CCD	charge coupled device
CCF	cross-correlation function
DNA	deoxyribonucleic acid
eGFP	enhanced green fluorescent protein
FCS	fluorescence correlation spectroscopy
IEP	isoelectric point
MC	Monte-Carlo
PDA	polydiacetylene
PMI	perylene monoimide
PMMA	poly(methylmethacrylate)
SCOM	scanning confocal optical microscopy
SMD	single molecule detection
spFRET	single pair fluorescence resonance energy transfer
STED	stimulated emission depletion
TIRF	total internal reflection fluorescence
TRFCS	time resolved fluorescence correlation spectroscopy
TTTR	time-tagged time-resolved

Chapter 1

Introduction

Searching the ISI Web of Knowledge for the term ”single molecule” reveals about 8500 hits (as of September 2007). Moreover, plotting the number of publications as a function of the year of publication reveals an exponential growth rate as shown in figure 1.1. In contrast to ensemble measurements, where sub-populations of molecules with different properties might be hidden due to the averaging over all populations, single molecule experiments offer an access to the properties of individual molecules. Whereas the term ”single molecule” does not explicitly refer to single molecule fluorescence or single molecule spectroscopy, these areas represent two of the main driving forces for the increasing number of publications. Many excellent reviews deal with the unique opportunities associated with the use of single fluorescent molecules as probes in biological or chemical environments [68, 104, 98]. However, before discussing their properties, the two main requirements for a successful detection of single molecules should be mentioned. The first requirement is that a sufficiently large number of detectable photons should be emitted during the (finite) time a single fluorophore stays within an excitation/detection focus. Secondly, the feasibility of detecting single photons using objectives with high numerical aperture and thus a large detection angle, appropriate filter sets and photo-detectors with high quantum yields is mandatory. For the experiments reported in this thesis, a variety of single molecule features will be used. In the simplest case, the diffusion of fluorescent molecules as, for example, dyes or auto-fluorescent proteins causes fluctuations in the detected intensity [61, 80]. These fluctuations can be used to determine, for example, the concentration and the diffusion coefficients of the fluorescent molecules. In general, photophysical properties play an important role. Whereas the fluorescent lifetime, which is accessible by using pulsed lasers with repetition rates in the megahertz range [95], can be used to measure the refractive index in the vicinity of the fluorophore [94, 96], the anisotropic emission of photons may reveal the three-dimensional orientation of the emission dipole of a single molecule [20, 2].

Beside using an isolated fluorophore, fluorophores can be attached to all kinds of nonfluorescent (macro-)molecules such as DNA and proteins [104]. The attached fluorophore enables monitoring the diffusivity of the macromolecule. Moreover, if a high energy fluorophore (in the following referred to as donor) and a low energy fluorophore (in the following referred to as acceptor) are attached to one and the same molecule of interest, the energy of the donor after excitation can be transfered non-radiatively to the acceptor. Due to the strong distance depen-

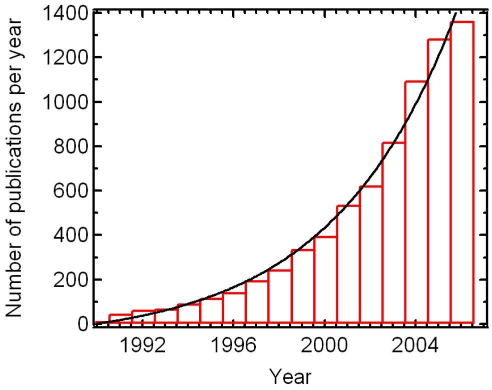

Figure 1.1: Number of publications per year (according to the ISI Web of Knowledge) for the term ”single molecule” (as of September 2007). The black solid line represents an exponential fit.

dency of the transfer probability, such systems are commonly used to detect conformational changes in the nanometer range [28, 87].

It is the main scope of this thesis to evaluate these well-characterized features of single fluorescent molecules within nanoporous membranes by optical confocal microscopy. The pores of the membranes are aligned along the long axis of the detection focus and feature pore diameters one order of magnitude smaller than the size of the diffraction-limited focus. Using this scheme, unprecedented experimental designs can be realized. Replacing the solution of freely diffusing fluorophores by a defined nanoporous solid enables higher analyte concentrations. Additionally, the diffusive behavior of the fluorophores is constrained by single pores and is expected to change dramatically. Analyzing the detected multi-parameter intensity time traces will allow probing the nanoporous system in terms of porosity, refractive index, and analyte - pore wall interactions on a single molecule level. Moreover, first steps towards orientation determination of molecules within nanoporous systems will be realized.

The structure of this thesis is as follows: Chapter 2 introduces the fundamentals in single molecules spectroscopy (SMS) as far as they are related to this work. After presenting the basic photophysical principles of fluorescence, the historical and current development of single molecule detection (SMD) in solution and three-dimensional orientation determination of single emission dipoles is outlined. Moreover, experimental techniques and appropriate tools for analyzing the data such as fluorescence correlation spectroscopy (FCS) are discussed. The materials and methods part of this thesis (chapter 3) deals with self-ordered porous alumina, which is introduced as a matrix for confining the diffusion. The fluorescent analytes are described briefly and details of the experimental set-up are discussed. An important part of this chapter is the description of the Monte-Carlo simulations, which are used to characterize the influence of the geometrical confinement within the pores on the diffusive behavior of single molecules in comparison with the results obtained experimentally. The presentation of results starts in chapter 4. Here, the diffusive behavior of different probes is analyzed within the membranes and, for comparison, in free solution. The experimental configurations are varied by changing the objectives, the lasers and the sample mounting in order to find appropriate experimental conditions. Chapter 5 deals with the three-dimensional orientation determination of the emission dipole of single molecules. The chapter describes a completly new approach for

the orientation determination. Therefore, the part of describing the proposed method theoretically and experimentally is included directly in this chapter. For the evaluation of this method, Monte-Carlo simulations and experiments of fluorescent latex beads and single fluorophores immobilized on the cover slide are performed. To span the bridge to the usage of nanoporous membranes for confinement, the orientational properties of pores filled with fluorescent polymers are investigated.
Chapter 6 summarizes the results and gives a short overview of potential applications in the future.

Chapter 2

Single molecule spectroscopy: fundamentals and beyond

Overview

In section 2.1, the photophysics of fluorescent molecules and the current state of knowledge in selected areas of single molecule spectroscopy (SMS) relevant to the scope of this thesis will be covered. After giving a short overview of the history of single molecule detection (SMD) in solution in section 2.2 and discussing the scanning confocal optical microscopy (SCOM) and its scientific relevance in section 2.3, I will concentrate on several applications, namely the single pair fluorescence resonance energy transfer (spFRET) in section 2.4, the fluorescence correlation spectroscopy (FCS) in section 2.5, and the 3D-orientation determination of single molecules in section 2.6. Section 2.7 will deal with methods, which have been suggested to geometrically confine molecules yielding smaller detection volumes.

2.1 The photophysics of single molecules

This section deals with the photophysics of single molecule experiments and follows the lines of references [77, 99, 112].
The photophysics of fluorescent molecules is usually illustrated using a Jablonski diagram. Figure 2.1 shows a simplified version of a three level system neglecting possible vibronic states. By absorbing a photon from a laser source with a rate constant of k_{exc} the molecule is excited from the ground state S_0 to the first excited singlet state S_1. The rate constant k_{exc} is defined as $k_{exc} = \sigma I/\hbar\omega$, where σ represents the absorption cross section of the molecule, I the applied laser intensity and $\hbar\omega$ the photon energy. A molecule in the S_1 state can undergo different relaxation processes:

- the singlet state S_1 can relax to S_0 by emitting a photon at a radiative rate constant k_{10}
- S_1 can relax to S_0 by *internal conversion* with a non-radiative rate constant k_{ic}
- the molecule can *bleach* with a rate constant k_{bl}

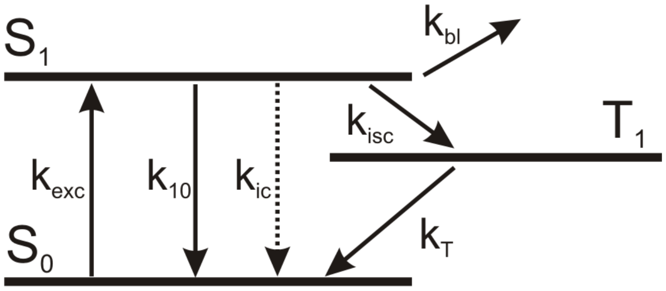

Figure 2.1: Simplified Jablonski diagram showing the transition pathways for a fluorescent molecule. The three level system consists of a ground state S_0, an excited singlet state S_1 and a triplet state T_1. The rate constants k_i are explained in the text.

- S_1 can undergo a spin-forbidden *intersystem crossing* to the first triplet state T_1 with non-radiative rate constant k_{isc}

An occupied triplet state T_1 can relax to S_0 with the rate constant k_T. In most cases, this process is non-radiative for single fluorescent molecules. Taking these relations into account, one can formulate a system of differential equations, which describes the occupancy of the different states as a function of time. If the probability of occupancy for the i-th state is given by ρ_i then the rate equation system reads

$$\begin{aligned}
\frac{d}{dt}\rho_{S_0} &= -k_{exc}\rho_{S_0}+k_{10}\rho_{S_1}+k_{ic}\rho_{S_1}+k_T\rho_{T_1} \\
\frac{d}{dt}\rho_{S_1} &= k_{exc}\rho_{S_0}-k_{10}\rho_{S_1}-k_{ic}\rho_{S_1}-k_{isc}\rho_{S_1}-k_{bl}\rho_{S_1} \\
\frac{d}{dt}\rho_{T_1} &= k_{isc}\rho_{S_1}-k_T\rho_{T_1}.
\end{aligned} \tag{2.1}$$

The term $k_{bl}\rho_{S_1}$ is often neglected for the calculations, but still remains a limiting factor for single molecule experiments. Still, the solution of the rate equation system is quite complicated. A less complex approach is the stationary case, where the derivatives are set to $\frac{d}{dt}\rho_{S_0}=\frac{d}{dt}\rho_{S_1}=\frac{d}{dt}\rho_{T_1}=0$ and the normalization condition is $1=\rho_{S_0}+\rho_{S_1}+\rho_{T_1}$. If the photon emission rate is defined as $R=k_{10}\rho_{S_1}$, then R reads

$$R=\frac{k_{10}}{1+\frac{k_{isc}}{k_T}+\frac{k_{10}+k_{ic}+k_{isc}}{k_{exc}}}. \tag{2.2}$$

It is obvious that the photon emission R saturates for $k_{exc}\rightarrow\infty$

$$R_{exc\rightarrow\infty}=\frac{k_{10}}{1+\frac{k_{isc}}{k_T}}. \tag{2.3}$$

Moreover, if one introduces the saturation intensity I_S as

$$I_S=\frac{Ik_T}{k_{exc}}\frac{k_{10}+k_{ic}+k_{isc}}{k_T+k_{isc}}, \tag{2.4}$$

the photon emission rate R can be rewritten as

$$R=R_\infty\frac{1}{\left(1+\frac{I_S}{I}\right)}. \tag{2.5}$$

In order to determine the fluorescence quantum yield Φ_f, which relates the number of absorbed photons to the number of emitted photons, the transition $I \to 0$ or at least $I \ll I_S$ leads to

$$R_{exc\to 0} = \frac{R_\infty I}{I_S} = k_{exc}\frac{k_{10}}{k_{10}+k_{ic}+k_{isc}} = k_{exc}\Phi_f = \frac{I\sigma}{\hbar\omega}\Phi_f. \tag{2.6}$$

Φ_f consists of radiative and non-radiative components. The fluorescence lifetime τ_{Fl} is related to the rate coefficients k_{10}, k_{ic} and k_{isc} and the fluorescence quantum yield Φ_f according to

$$\tau_{Fl} = \frac{1}{k_{10}+k_{ic}+k_{isc}} = \frac{\Phi_f}{k_{10}}. \tag{2.7}$$

Based on this relations, the fluorescence lifetime is an important parameter to characterize both the intrinsic behavior of single molecules and the interactions between the molecule and its chemical and physical environment. For applications see section 2.3.

2.2 Single molecule detection in solution

The main motivation of detecting single molecules is to circumvent the averaging effect of ensemble measurements. For example, if the overall fluorescence intensity from a sample containing ten fluorescent particles is detected, the potential presence of two different species with different brightness cannot be resolved. The following section outlines the progress in the field of single molecule detection (SMD) starting from the first experiments, which raised up a lot of requirements and notes for forthcoming single molecule experiments. These considerations gave the starting signal for a very fast development in the field of SMD [104].

The first detection of a multiply labeled single molecule was reported by Hirschfeld in 1976 [42]. He used proteins labeled with 80-100 chromophores which were excited by an Argon laser operating at a wavelength of 488 nm using a total internal reflection scheme. In such a scheme, the angle of the incident laser light is sufficiently large to reflect the laser light totally at the interface between cover glass and sample volume. Only the evanescent field can enter the sample volume. Therefore, the small penetration depth of the evanescent field provided a excitation/detection volume of about 24 fl. For each labeled protein which entered the volume, the fluorescence signal was counted by a photomultiplier until a complete bleaching of the attached chromophores occurred. In another publication, Hirschfeld described the theoretical concept of time-gated fluorescence detection using pulsed lasers, which will be explained more in detail in section 2.3, and the pre-bleaching of perturbing fluorescent compounds [44]. Hirschfeld's considerations can be summarized as follows: 1) the excitation/detection volume has to be as small as possible to discriminate the fluorescence from the molecule of interest from the background luminescence; 2) SMD suffers from photo-bleaching of fluorescent molecules; 3) time-gating may provide a tool for discrimination of different fluorescent species; 4) quantum efficiencies and fluorescence lifetimes are important detection parameters [43]. Interestingly, already in 1976 Koppel and coworkers introduced a confocal detection scheme (as it will be described in section 2.3) for studying the molecular and structural mobility of fluorescent probes without going to the single molecule level [55].

It took almost 15 years until the detection of single fluorophores in solution was realized. In 1990 Shera and coworkers successfully showed the detection of single Rhodamine-6G molecules in solution [90]. They used a mode-locked frequency-doubled Nd:YAG laser with short pulses (70 ps) and high repetition rate (82 Mhz) for exciting the molecules. The light was focused into a flow cell were the excitation of the Rhodamine-6G molecules occurred. The fluorescence was collected by a microscope objective and then spatially filtered by a slit. After passing an appropriate band pass filter, the light was detected by a microchannel-plate photomultiplier. With this set-up, it was possible to reach sufficient signal-to-noise ratios even if the applied laser intensity was so high that the Rhodamine-6G molecules were photo bleached before traveling the whole way through the detection volume. At the same time, Rigler and Widengren published the detection of single Rhodamine-6G molecules using a confocal set-up in a book chapter [81]. The main advantage of the confocal set-up was demonstrated in 1993, when Rigler and coworkers showed its superior performance in terms of the obtainable signal-to-noise ratio [80]. One year later Eigen and Rigler expanded the range of applications by showing that the binding of a labeled DNA primer to a defined or undefined DNA sequence can be monitored by using fluorescence correlation spectroscopy [18].

In 1996 Edman and coworkers showed that conformational transitions of single tetramethyl-rhodaminemolecules linked to a DNA sequence can be resolved using single molecule time-resolved detection [16].

2.3 Scanning confocal optical microscopy

Since the first description of a scanning confocal optical microscope (SCOM) by M. Minsky in 1955 (he filled a patent instead of publishing a scientific publication) the SCOM had become a versatile tool with well known properties in the field of fluorescence microscopy [103]. Every confocal microscope is characterized by the use of the objective both for illumination of a focal volume and for detection out of the focal volume making the basic set-up as simple as possible. A schematic diagram of a state-of-the-art SCOM as it is used for this work is shown in figure 2.2. The main principles of the set-up will be discussed in this section, whereas technical details will be discussed in section 3.2. The set-up is used with pulsed lasers instead of continuous-wave lasers to gain additional information about the fluorescent species such as the fluorescence lifetime. The repetition rates of the lasers (MHz range) are adjusted to the fluorescence lifetime in such a way that the detection of a photon can be attributed to the last laser pulse. If more than one laser is used at the same time, the synchronized laser pulses alternate and are combined into one beam using a first dichroic mirror. After adjusting the polarization by a $\lambda/2$ and a $\lambda/4$ filter, the laser light is coupled into a polarization maintaining fiber in order to obtain a point source at the end of the fiber. A lens or better an apochromatic objective with low magnification is used to obtain a parallel beam, which than reaches the second dichroic mirror. This dichroic mirror reflects the laser light to the overfilled objective (overfilled: the beam diameter of the laser is larger than the aperture of the objective), which normally has a high numerical aperture and a high magnification to realize a small, diffraction-limited volume for the excitation of the fluorophores. The objective itself is mounted to a piezo drive to change the position of the focal volume in the z-direction. To perform the scanning, the whole sample holder can be moved by additional piezo drives in the x- and/or y-direction.

Caused by the Stokes shift, the excited fluorophores emit light with a higher wavelength, which

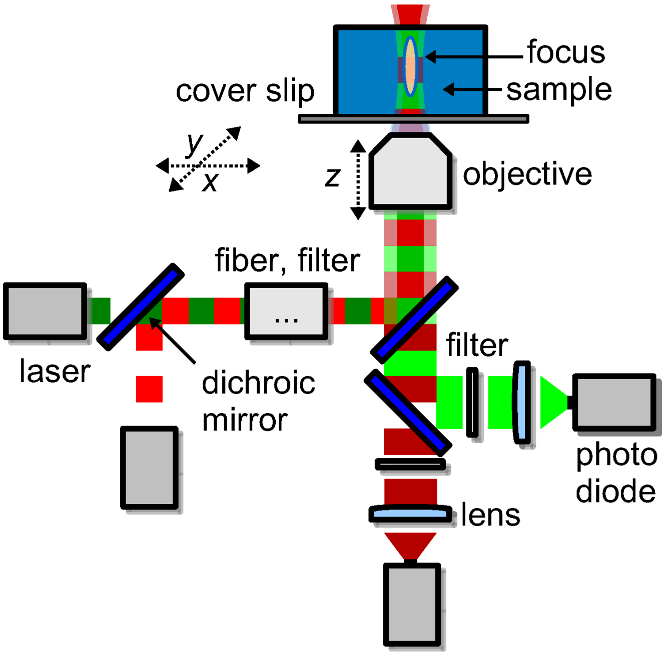

Figure 2.2: Schematic diagram of an advanced confocal microscope. Two pulsed lasers with different emission wavelengths are used for interleaved excitation of the fluorophores. The objective is used both for illumination of the focal volume and for detection out of the focal volume. The avalanche photodiode is acting as a pin-hole.

is collected by the objective and can now pass the second dichroic mirror. Further on, the wavelength range of the detected light can be either separated by a third dichroic mirror or tuned with different filter sets in order to get rid of remaining laser light or inelastic raman scattering. Afterwards, the light is focused by a lens onto the very small effective detection area of single photon counting modules (avalanche photo diodes). In this scheme, the detectors are acting as pin-holes and supress the light which is not originating from the focal plane of the microscope objective.

Time-Correlated Single Photon Counting

One of the major improvements in scanning confocal optical microscopy during the last decade was the availability of relatively cheap pulsed diode-laser sources and fast hardware for detecting the photons, whose combination allows performing time-correlated single photon counting (TCSPC). The TCSPC as it is used in this thesis works in the so-called time-tagged time-resolved (TTTR) data acquisition mode which is sketched in figure 2.3 and described in more detail in reference [102]. A pulsed laser with a sufficiently high repetition rate and a short pulse duration is used to excite a fluorescent molecule in the confocal volume. The laser and the first timer are triggered by an external source providing the possibility to measure the TCSPC-time between the arrival of a photon and the last laser pulse with a time resolution in the picosecond range. The time resolution is given by the channel width of the hardware. Additionally, the time at which a photon is detected is recorded with a resolution on the nanosecond scale on a continuous time trace to obtain the information required for Fluorescence Correlation Spectroscopy (see chapter 2.5). Even more sophisticated TCSPC-techniques provide full correlation from a picosecond to second range as described in reference [23].

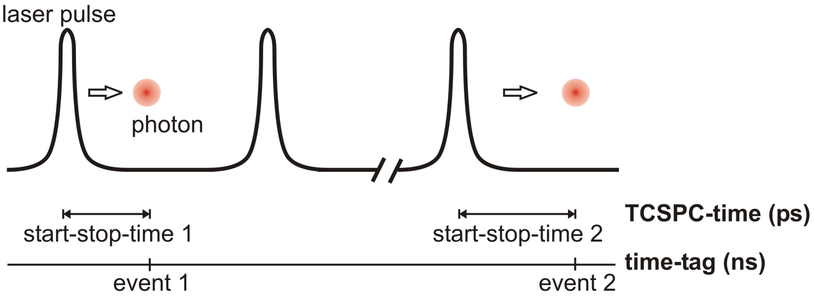

Figure 2.3: Principle of the time-tagged time-resolved (TTTR) data acquisition mode. For every photon two times are stored: a) TCSPC-time which counts the time between the last laser pulse and the detection of a photon with picosecond resolution, and b) the time-tag of every photon on a continuous time trace with nanosecond resolution.

The fluorescence lifetime (see chapter 2.1) of individual molecules can be calculated from the recorded TCSPC-times and provides thereby a versatile tool for studying different photophysical phenomena:

local environment Strickler and Berg reported in 1962 that the fluorescence lifetime of a fluorophore is proportional to $1/n^2$, where n is the environmental refractive index [94]. Thus, the fluorescence lifetime can be used to probe the environmental conditions as for example described by Suhling and coworkers [96]. They used the green fluorescent protein (GFP) as a probe in environments with different refractive indices adjusted by different concentrations of glycerol.

TRFCS The time-resolved fluorescence correlation spectroscopy (TRFCS) can be used to separate the intensity of two fluorescent species as long as the fluorescent lifetimes of the species sufficiently differ [8]. TRFCS is explained in more detail in section 2.5.

sp-FRET If a donor molecule is closer than 10 nm to an acceptor molecule, then the donor can transfer energy to the acceptor. This process decreases the fluorescence lifetime of the donor and can thereby give a quantitative value for the energy transfer. For further information see section 2.4.

rotational mobility The rotational mobility of a fluorophore can be calculated from polarization-resolved fluorescence decays [10, 92]. Thereby, one can monitor the viscosity in the vicinity of the fluorophor or binding events, which change the rotational mobility. For further information see reference [56].

For a more comprehensive review of the field see reference [95]. It is obvious that TCSPC dramatically increases the number of accessible parameters to characterize single fluorophores and there nearby chemical, physical, and biological environment.

2.4 Single pair fluorescence resonance energy transfer

One of the most frequently used techniques in the area of single molecules is the (single pair) Förster resonance energy transfer or (single pair) fluorescence resonance energy transfer (spFRET), which allows the study of conformational changes of proteins with high accuracy and a resolution in the nanometer range [66, 89, 104, 105]. Here, emphasized by the term ”single pair”, we are mainly interested in the detection of only one single molecular system at the same time within the focus of the confocal microscope.

Förster published in 1948 that a distance-dependent, non-radiative energy transfer between two fluorophores can occur, as long as two preconditions are fulfilled [28]: 1) the fluorophores are in close proximity ($< 10\,\mathrm{nm}$), 2) the emission spectrum of the high energy fluorophore (*donor*) overlaps the absorption spectrum of the lower energy fluorophore (*acceptor*).

Conventionally, the used microscope consists of one laser for excitation (pulsed or continuous operating mode) of the donor and two photo diodes for a wavelength-dependent detection of the donor and the acceptor emission, respectively.

The energy transfer rate k_{fret} between the excited states $S_{1,D} \rightarrow S_{1,A}$ can be expressed using $k_{F_0,D}$ as the fluorescence rate constant of the donor in absence of the acceptor and r as the distance between the fluorophores according to

$$k_{fret} = k_{F_0,D} \left(\frac{R_0}{r} \right)^6 . \tag{2.8}$$

The distance of the fluorophores, where the probability of energy transfer by a non-radiative dipole-dipole interaction from the donor to the acceptor is 50%, is called the Förster radius R_0 reading

$$R_0 = \sqrt[6]{\frac{\kappa^2 J(\lambda)\, \Phi_D K}{n^4}}, \tag{2.9}$$

with κ as the orientation factor ($\kappa = 2/3$ for isotropic rotating systems), Φ_D as the donor quantum yield in absence of the acceptor, K as an constant ($K = 8.8 \cdot 10^{-23}\,\mathrm{mol}$), n as the refractive index of the surrounding solution and J as the overlap integral of the donor emission spectra and the acceptor absorption spectra. The overlap integral is calculated as a function of the wavelength λ

$$J = \int_0^\infty f_D(\lambda)\varepsilon_A(\lambda)\lambda^4 d\lambda, \tag{2.10}$$

with $\varepsilon_A(\lambda)$ as the molar extinction coefficient of the acceptor and f_D as the normalized emission spectrum of the donor ($\int f_D(\lambda) d\lambda = 1$).

The energy transfer efficiency E can be either determined by the change in donor lifetime $\tau_{F_1,D}$

$$E = \frac{k_{fret}}{k_{F_0,D} + k_{fret}} = \left[1 + \left(\frac{r}{R_0} \right)^6 \right]^{-1} = 1 - \frac{\tau_{F_1,D}}{\tau_{F_0,D}}, \tag{2.11}$$

where $\tau_{F_0,D}$ represents the fluorescence lifetime in absence of the donor or by comparing the measured donor and acceptor intensities I_D and I_A as

$$E = \frac{I_A}{I_A + \gamma I_D}. \tag{2.12}$$

The drawback of the second method is the incorporation of the donor and acceptor quantum yields Φ_D and Φ_A and the detection efficiencies of both channels η_D and η_A for determining

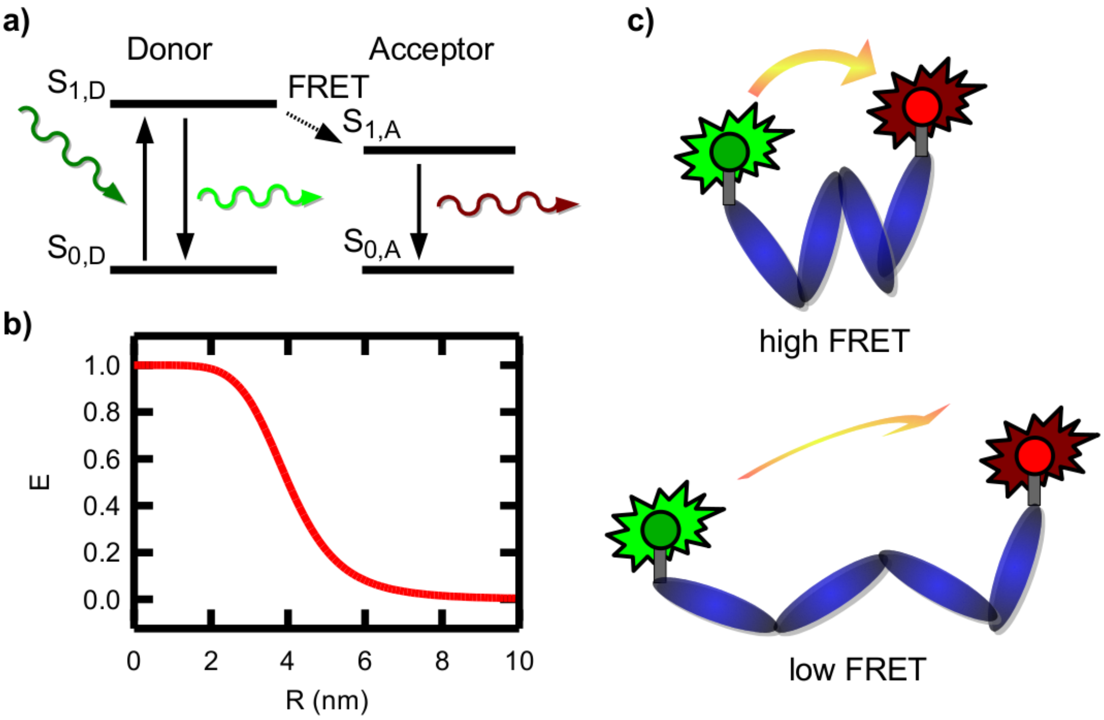

Figure 2.4: **a)** Simplified Jablonski diagram for FRET. After absorbing a photon, the energy in the excited state $S_{1,D}$ can be released directly by emitting a photon ($S_{1,D} \rightarrow S_{0,D}$) or indirectly after a resonant energy transfer ($S_{1,D} \rightarrow S_{1,A} \rightarrow S_{0,A}$). **b)** Energy transfer efficiency E plotted as a function of R for R_0 = 4 nm. The transfer efficiency equals 50% at R = 4 nm. **c)** Schematic diagram of a protein labeled with a donor and an acceptor. If the fluorophores are in close proximity (for example: folded protein), the probability of the energy transfer is higher than in the case of a larger donor to acceptor distance (unfolded protein).

the correction factor γ as

$$\gamma = \frac{\eta_A \Phi_A}{\eta_D \Phi_D}. \tag{2.13}$$

However, no pulsed laser set-up is necessary if only intensities are analyzed.

These considerations are summarized and visualized in figure 2.4, where **a)** shows a simplified Jablonski diagram for FRET, **b)** the distance dependency of the energy transfer using equation 2.11 with R_0 = 4 nm and **c)** a doubly labeled protein, whose potential conformational changes (folded$\rightleftharpoons$ unfolded protein) will change the observable energy transfer.

Schuler and coworkers demonstrated in 2002 that spFRET in solution can probe the energy surface of protein folding [87, 86]. In 2003 Rhoades and coworkers showed spFRET of immobilized proteins [79]. Newly developed single molecule techniques allow a time resolution on the nanosecond scale [71]. For a recent review in the field of SMS protein folding/unfolding see for example reference [66].

Alternating-Laser Excitation

However, spFRET using one laser for excitation as it has been described in the last section suffers from a number of drawbacks [51]: First, if a doubly labeled molecule (donor and acceptor) has an energy transfer efficiency close to unity (high FRET), this molecule can hardly be distinguished from a second molecule, which is only labeled with an acceptor. The first one will show high intensities in the red detection channel and low intensities in the green one, whereas for the second molecule there is a certain probability to excite the acceptor with the green laser (this effect is known as crosstalk). Therefore, the second molecule will show a similar intensity behavior like the first one. Second, if a doubly labeled molecule has an energy transfer efficiency close to zero, there might be no sufficient difference in the intensity traces to a molecule only labeled with a donor. Third, there is no possibility to quantitatively analyze the molecular interactions. If there is an interaction in the form of $M_A + L_D \rightleftharpoons M_A L_D$, where M_A represents an acceptor-labeled macromolecule and L_D a donor-labeled ligand, the different species can not be resolved.

To overcome these drawbacks, Kapanidis, Lee and coworkers suggested in 2004 a new excitation scheme called ALEX (alternating-laser excitation) based on the use of two lasers instead of one [51]. Each of the two lasers operating in the continuous wave mode was modulated by an electro-optical modulator in association with a polarizer in such a way that an alternated excitation by either red or green laser light was achieved in order to excite the acceptor and the donor directly. The alternation period τ_{alt} was in the µs to ms range and during each excitation cycle the number of photons in both detection channels was recorded. Integrating over a certain amount of alternation cycles led to four binned intensity traces: **a)** $I_{D_{exc}}^{D_{em}}$, intensity in the donor detection channel after excitation of the donor, **b)** $I_{D_{exc}}^{A_{em}}$, intensity in the acceptor detection channel after excitation of the donor, **c)** $I_{A_{exc}}^{A_{em}}$, intensity in the acceptor detection channel after excitation of the acceptor and **d)** $I_{A_{exc}}^{D_{em}}$, intensity in the donor detection channel after excitation of the acceptor.

The calculation of the energy transfer efficiency E remains similar to equation 2.12

$$E = \frac{I_{D_{exc}}^{A_{em}}}{I_{D_{exc}}^{A_{em}} + \gamma I_{D_{exc}}^{D_{em}}}, \tag{2.14}$$

with γ as the correction factor mentioned previously. However, a new parameter S can be formulated, which represents a donor-acceptor (D- A) stoichiometry according to

$$S = \frac{I_{D_{exc}}^{A_{em}} + \gamma I_{D_{exc}}^{D_{em}}}{I_{D_{exc}}^{A_{em}} + \gamma I_{D_{exc}}^{D_{em}} + I_{A_{exc}}^{D_{em}} + I_{A_{exc}}^{A_{em}}}. \tag{2.15}$$

It can be shown that S is independent of E (supporting material in reference [51]).

If a molecule is only donor-labeled, then $S \approx 1$ because of $I_{A_{exc}}^{D_{em}} + I_{A_{exc}}^{A_{em}} \approx 0$, and if a molecule is acceptor labeled only, then $S \approx 0$ because of $I_{D_{exc}}^{A_{em}} + \gamma I_{D_{exc}}^{D_{em}} \approx 0$. Additionally, as long as $I_{A_{exc}}^{D_{em}} + I_{A_{exc}}^{A_{em}} \approx I_{D_{exc}}^{A_{em}} + \gamma I_{D_{exc}}^{D_{em}}$, the stoichiometry of doubly labeled molecules is close to $S \approx 0.5$ whereas E remains dependent on the donor-to-acceptor distance. Figure 2.5 shows a schematic diagram of an E vs. S plot separating four different species using the stoichiometry parameter S and the energy transfer efficiency parameter E.

This excitation scheme can be further improved by using pulsed interleaved lasers instead of a modulated continuous wave laser [69]. Pulsed lasers with high repetition rates in the MHz range and pulse widths of around 0.5 ns allow to relate every detected photon to the last excitation pulse as long as two requirements are fulfilled: 1) the fluorescence lifetime is shorter than the time slice between two laser pulses and 2) the mean photon count rate is much smaller than

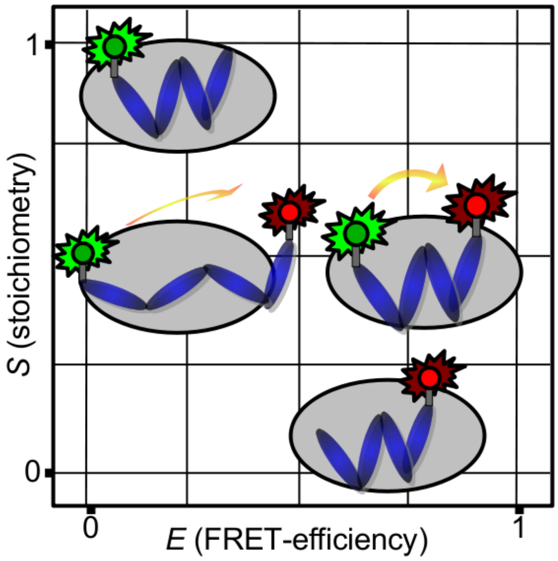

Figure 2.5: Schematic diagram of E-S plot for one donor-labeled, two doubly-labeled and one acceptor-labeled species. Without using the parameter S, a distinction of two species with almost the same (apparent) energy transfer efficiency E would not be possible.

the repetition rate of the lasers. The advantage of the last excitation scheme over that of ALEX is that one conserves the lifetime information of every detected photon.

2.5 Fluorescence correlation spectroscopy

In 1972 Magde and coworkers presented a new method to determine diffusion coefficients and particle concentrations from a detected fluctuating fluorescence signal [61]. Two landmark publications followed in 1974, which described the concept more in detail [19, 62].
Fluorescence correlation spectroscopy (FCS) is based on the fluctuation $\delta I_d(t)$ of the detectable, time-dependent fluorescence intensity $I_d(t)$ around a mean value $\langle I_d \rangle$ even under equilibrium conditions, reading

$$I_d(t) = \langle I_d \rangle + \delta I_d(t). \tag{2.16}$$

In the simplest case, the fluctuation of the fluorescence signal is caused by the Brownian motion of a few fluorescent molecules in a sufficiently small detection volume. It was shown by Rigler and coworkers, that the convolution of the collimated laser beam and the collection efficiency function can be approximated by a three-dimensional Gaussian with half axis w_0 and z_0 [80]

$$I(x,y,z) = I_0 \exp\left(-2\left(\frac{x^2+y^2}{w_0^2} + \frac{z^2}{z_0^2}\right)\right), \tag{2.17}$$

which acts as the excitation/detection focus. Let us further assume that at the time $t_0 = 0$ a single fluorescent molecule is placed in the center of the focus. Now, if the following time increment τ_1 is short enough, so that the mean free pathway of the molecule is much smaller than the size of the focus, there is a certain probability that the molecule remains within the focus at the measurement-time $t_1 = t_0 + \tau_1$. With this consideration it is obvious that the intensities detected in consecutive measurement intervals are related to each other. Generally, in FCS, the fluctuating intensity is analyzed in terms of the intensity auto-correlation function (ACF)

$$G(\tau) = 1 + \frac{\langle \delta I_d(t) \cdot \delta I_d(t+\tau) \rangle}{\langle I_d \rangle^2}. \tag{2.18}$$

A detailed derivation of the ACF can be found in the above-mentioned references or in references [46, 112].

The ACF for the one-dimensional case of pure diffusion along the z-axis reads

$$G_{1D}(\tau) = 1 + \frac{1}{N}\left(1 + \frac{4D\tau}{z_0^2}\right)^{-\frac{1}{2}}, \tag{2.19}$$

for the two dimensional case of pure diffusion in the x-,y-plane

$$G_{2D}(\tau) = 1 + \frac{1}{N}\left(1 + \frac{4D\tau}{w_0^2}\right)^{-1}, \tag{2.20}$$

and for the three-dimensional case of pure diffusion

$$G_{3D}(\tau) = 1 + \frac{1}{N}\left(1 + \frac{4D\tau}{w_0^2}\right)^{-1}\left(1 + \frac{4D\tau}{z_0^2}\right)^{-\frac{1}{2}}, \tag{2.21}$$

where N represents the mean particle number in the detection volume and D the diffusion coefficient. Defining the diffusion time for the one-dimensional diffusion as

$$\tau_{\mathrm{D}}^{\mathrm{1D}} = \frac{z_0^2}{4D} \tag{2.22}$$

and for two- and the three-dimensional case as

$$\tau_{\mathrm{D}}^{\mathrm{2D,3D}} = \frac{\omega_0^2}{4D} \tag{2.23}$$

the ratio between the diffusion time in the one-dimensional case along z and in the three-dimensional case is just the square of the structural parameter s, which is defined as $s = z_0/w_0$ and amounts to $s \approx 4$ in a standard confocal microscope. Therefore, one can expect a 16 times longer τ_{D} inside a small channel for one-dimensional diffusion as compared to free bulk diffusion according to

$$\tau_{\mathrm{D}}^{\mathrm{1D}} = \frac{z_0^2}{4D} = \frac{s^2 w_0^2}{4D} = 16\tau_{\mathrm{D}}^{\mathrm{3D}}. \tag{2.24}$$

The ratio between the visually easier to access ACF decay half times $\tau_{1/2}$, however, is even larger due to the different exponents of the diffusion terms.

Equations 2.19 and 2.21 can be expanded in order to determine the triplet parameters of the molecules [106], reading

$$G_{1D,T}(\tau) = 1 + \frac{1}{N}\left(1 + \frac{4D\tau}{z_0^2}\right)^{-\frac{1}{2}} \frac{1 - F + e^{-\frac{\tau}{\tau_T}}}{1 - F} \tag{2.25}$$

or rather

$$G_{3D,T}(\tau) = 1 + \frac{1}{N}\left(1+\frac{4D\tau}{w_0^2}\right)^{-1}\left(1+\frac{4D\tau}{z_0^2}\right)^{-\frac{1}{2}} \frac{1-F+e^{-\frac{\tau}{\tau_T}}}{1-F}, \tag{2.26}$$

with F as the fraction of molecules in the triplet state, and τ_T as the mean duration of stay of the triplet state. Additionally, suggestions have been made to determine even rate constants as described in section 2.2 and photo-induced (back-)isomerization of dyes [106, 107], facing the problem that with a large set of fitting parameters the accuracy of each parameter determination suffers. Gennerich and Schild derived fitting functions for confined diffusion within neuronal dendrites, which feature a diameter of less than 1 µm and a length of tens of micrometers [31, 30]. For a more comprehensive review about the present use of FCS see reference [33].

In contrast to the ACF, which is calculated out of one intensity time trace, it is often useful to determine the so called cross-correlation function (CCF), which is calculated out of two intensity time traces. Therefore, the emitted beam of the fluorescent light is separated using a 50/50 beamsplitter and then focused on two detectors. The definition for the CCF

$$G_{\mathrm{CC}}(\tau) = 1 + \frac{\langle \delta I_{d,1}(t)\cdot\delta I_{d,2}(t+\tau)\rangle}{\langle I_{d,1}\rangle\langle I_{d,2}\rangle} \tag{2.27}$$

yields the same fitting functions as described previously. The advantage of using the CCF lies in the fact that one can get rid of the effect of afterpulsing. Afterpulsing is an intrinsic property of the detectors, where the detection of a real photon can be followed by a detection of a virtual photon [21, 113] and is further described in the next subsection.

Time-resolved fluorescence correlation spectroscopy

In 2002 Böhmer and coworkers introduced a new method for performing fluorescence correlation spectroscopy by using the fluorescence lifetime to separate mixtures of different fluorescent species [8]. The method is called time-resolved fluorescence correlation spectroscopy (TRFCS). In TCSPC (see section 2.3), every photon is sorted into a channel according to its arrival time after the laser pulse (TCSPC-time). Let us assume a mixture of two species; species **A** with a short fluorescence lifetime and species **B** with a sufficiently longer lifetime. It is obvious that photons which arrive shortly after the laser pulse are mainly emitted by species **A**, whereas photons which arrive almost before the next pulse are mainly emitted by species **B**. In fact, every photon can be related to one of the species with a certain probability. Generally, the intensity I_j of each channel j can be written as

$$I_j = w^{(A)}p_j^{(A)} + w^{(B)}p_j^{(B)}, \tag{2.28}$$

where $w^{(A,B)}$ represents the overall number of photons and $p^{(A,B)}$ the normalized probability of detecting photons within channel j of the respective species **A** and **B**. If a mixture of two species in terms of Fluorescence Correlation Spectroscopy needs to be separated, two filter sets $f_j^{(i)}$ ($i =$**A**, **B**) have to be created in such a way that they fulfill

$$\left\langle \sum_{j=1}^{L} f_j^{(i)} I_j \right\rangle = w^{(i)}, \tag{2.29}$$

where L is the total number of TCSPC channels. The brackets indicate an averaging over an infinite number of measurements. Moreover, it can be shown, assuming that photon detection follows Poissonian statistics, that with $\hat{M}_{ij} = p_j^{(i)}$ the filter sets $f_j^{(i)}$ can be calculated according to

$$f_j^{(i)} = \left(\left[\hat{M} \cdot \mathrm{diag} \left\langle I_j \right\rangle^{-1} \cdot \hat{M}^{\mathrm{T}} \right]^{-1} \cdot \hat{M} \cdot \mathrm{diag} \left\langle I_j \right\rangle^{-1} \right). \tag{2.30}$$

The $L \times L$-dimensional matrix consists of the diagonal elements $\left\langle I_j \right\rangle^{-1}$ with $j = 1, ..., L$. The approximation $\left\langle I_j \right\rangle \approx I_j$ is used for direct calculation. The patterns $p_j^{(i)}$ have to be measured independently from each other by measuring the two species in separate solutions. The filter sets $f_j^{(i)}$ and the corresponding patterns $p_j^{(i)}$ form an orthonormal system, which can be used for verification of the filter sets according to

$$\sum_{j=1}^{L} f_j^{(i)} p_j^{(k)} = \delta_{i,k}. \tag{2.31}$$

In contrast to the normal procedure of calculating the auto-correlation function, where every photon is previously weighted with a factor of 1, the weighting factor in TRFCS is $f_j^{(i)}$.
Another useful application of TRFCS is the possibility of discriminating afterpulsing from the raw data [21]. In avalanche photodiodes every absorbed photon can generate a photoelectron which then leads to further ionizations until the breakdown pulse occurs at the end. This breakdown leads to the pulse which indicates the detection of a photon. However, if some of the charge carriers remain electronically trapped for a certain time, they can be later on released by thermal excitation thereby starting a new chain of ionizations. This will cause a new pulse at the detector output now generated by a virtual photon. Due to the fact that FCS is sensitive for temporally related events, afterpulsing causes decays in the auto-correlation curve which often coincide with the decay of triplet states. In contrast to the prior use of TRFCS, where the fluorescence decay behavior of the two single species has to be known, this problem is easier to solve: Let us assume, analogous to equation 2.28, that the measured intensity per channel is a superposition of two fractions, namely the ”real” data fraction **A** and the afterpulsing fraction **B**. The probability for afterpulsing follows an exponential decay with a time constant large compared to the time between two laser pulses. For this reason, the probability pattern for **B** reads $\hat{M}_{Bj} = p_j^{(B)} = L^{-1}$, where L represents the total number of TCSPC channels. For the calculation of $p_j^{(A)}$, the minimum value of I_j is substracted from every measured I_j. After the normalization it follows that $\hat{M}_{Aj} = p_j^{(A)} = \sum I_j / \left(I_j - \mathrm{Min}(I_j)\right)$. The calculation of the filter sets is straightforward using equation 2.30 and taking $\left\langle I_j \right\rangle \approx I_j$.

Influence of uncorrelated background

If the diffusion of single molecules is confined to host materials, this may cause additional uncorrelated background luminescence. Either caused by the material itself or by adsorption of probe molecules onto the host material, the background influences the behavior of the auto-correlation function. Even if the mean diffusion time τ_D remains unchanged, the amplitude of the auto-correlation function is getting smaller with increasing background luminescence. As mentioned above, the amplitude is inversely proportional to the number of apparent molecules within the focus. Based on the work of Koppel in 1974 [54], the following equation was derived by Milon and coworkers [67] in order to relate the calculated apparent number of molecules N to the real number of molecules N' and the (apparent) number of molecules N_{noise} given by the (uncorrelated) background according to

$$N = \frac{(N' + N_{noise})^2}{N'} \tag{2.32}$$

with

$$N_{noise} = \frac{\text{background count rate per second}}{\text{count rate per molecule per second}} = \frac{\langle I_{Bg} \rangle}{\langle I \rangle - \langle I_{Bg} \rangle} N', \tag{2.33}$$

where $\langle I_{Bg} \rangle$ is the (estimated) mean background intensity and $\langle I \rangle$ the measured mean intensity. If the presence of (uncorrelated) background cannot be completely neglected, the real number of molecules N' in the focus is always smaller than the calculated one without background correction.

2.6 Orientation determination: from 2-D to 3-D

Beside using single molecules for spFRET as described in section 2.4, another unique feature of single molecules is their absorption and emission anisotropy due to the well-defined transition dipole(s) for both processes allowing the determination of the molecule's orientation. As shown in figure 2.6 **a)**, the orientation of a vector in spherical coordinates is fully determined by the polar angle θ and the azimuthal angle ϕ. Whereas the determination of θ is quite sophisticated, the determination of ϕ is more straightforward. Figure 2.6 **b)** shows that by using a polarizing beamsplitter in front of two detectors the detectable light can be divided into its horizontal and vertical components. However, it has to be emphasized that the simple relation $\tan\phi = I_{c,0}/I_{c,90}$ does not hold for using microscope objectives with high numerical aperture. Historically, the first polarization-resolved techniques performed at single molecules were based on a different concept (for orientation determination in steady-state fluorescence polarization microscopy see reference [1]). Instead of detecting polarization-resolved intensities, the polarization of the laser light was modulated before exciting the single molecules. Note that ϕ corresponds to the azimuthal angle of the emission transition dipole, which does not coincide with the azimuthal angle α of the absorption transition dipole in any case [36]. In 1993 Güttler and coworkers published a method, where the polarization of the laser light was changed with a $\lambda/2$ retardation plate [34]. The polarized light was used to excite single pentacene molecules in a p-terphenyl matrix. The measured intensity is a function of the azimuthal angle ϕ and was used to show the existence of two structural domains. In 1994 Xie and coworkers used two polarization directions (0° and 90°) to show that dipole rotation is the origin of emission jumps in sulforhodamine 101 adsorbed on glass [110]. A very accurate determination of the in-plane dipole angle α was demonstrated by Ha and coworkers in 1996 [35]. Single molecules were excited in the far field with linearly polarized light. The polarization angle ψ was continuously modulated in the millisecond range using an electro-optical modulator. Thus, the detected emission signal can be plotted as a function of ψ. Assuming that the emission signal I_{em} is a function of the absorption transition dipole $\overrightarrow{\mu}$ and the electrical

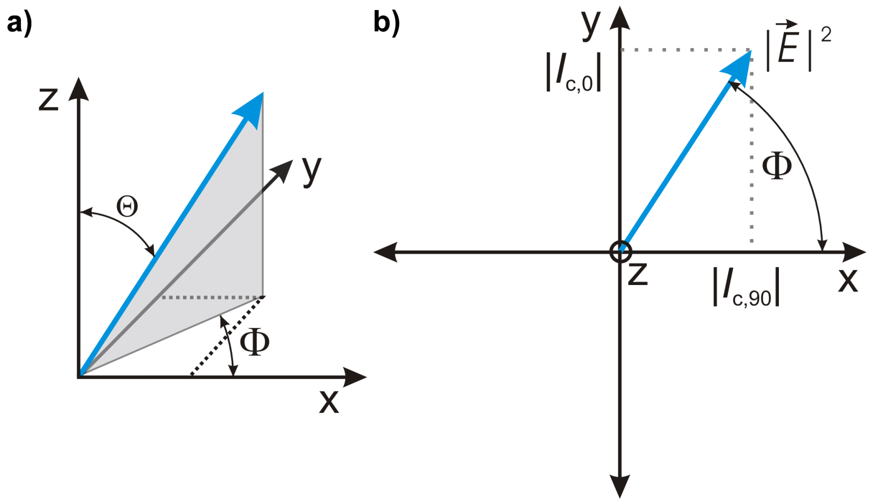

Figure 2.6: a) The orientation of a vector in spherical coordinates is fully determined by the polar angle θ and the azimuthal angle ϕ. **b)** Polarization-resolved techniques are using a projection of the transition dipole to determine the azimuthal angle ϕ. Here, a polarizing beamsplitter is used to divide the detectable light into its horizontal ($I_{c,0}$) and vertical ($I_{c,90}$) components.

field vector $\vec{E}$ according to

$$I_{em} \propto \left| \vec{\mu} \cdot \vec{E} \right|^2, \tag{2.34}$$

the detected modulated intensity can be fitted using

$$I_{em} = I_0 \cos^2(\psi - \phi) + I_{back}, \tag{2.35}$$

where I_0 is the signal intensity and I_{back} the background intensity. Moreover, this technique can resolve desorption and re-adsorption of single molecules from and onto the coverslip but suffers from the high number of photons which have to be detected in order to achieve sufficient accuracy. A more detailed description of the method can be found in reference [36]. In 1997 Sase and coworkers resolved the axial rotation of sliding actin filaments by exciting the fluorophores with circularly light and separating the emitted fluorescence with a polarizing beamsplitter [83].

Three-dimensional orientation determination

As mentioned above, the determination of the full three-dimensional orientation of single molecules is much more sophisticated. In the following, several methods will be discussed, which have been proposed in the literature.
Betzig and Chichester showed in 1993 that a near-field scanning optical microscope can be used to determine the accurate position and the three dimensional orientation of single fluorophores [5]. Unexpectedly, the imaged molecules did not appear as identical peaks with comparable width but rather as a distribution of ellipsoidal and symmetric peaks or rings and arcs. These patterns can be calculated for various orientations taking into account the interaction of the electric dipole of the molecule with the incident electromagnetic field from the aperture. In 1999 Bartko and coworkers published a detection sheme using a confocal microscope operating in a total internal reflection mode between the sample/air interface with CCD wide-field

detection [2]. After slightly defocussing the molecules in the z-direction, the imaged intensity patterns were used to determine the orientation of the molecules by applying an appropriate fitting-model. A similar pattern approach is described in reference [7]. Instead of using slight defocussing, different directions of incidence with linearly polarized light can be used for orientation determination, resulting in a shot noise-limited angular resolution of 2° [78]. For the case of using highly symmetric single chromophores (e.g. CdSe quantum dots) Empedocles and coworkers demonstrated in 1999 that comparing the fluorescence intensity as a function of the polarization angle is sufficient for a three-dimensional orientation determination [20].

Several other publications deal with more complex excitation schemes. Sick and coworkers used an annular illumination geometry approach, where the inner part of the laser beam is cut off [91]. Again, the imaged intensity patterns can be attributed to different orientations without loosing the spatial information as it occurs with the defocussing techniques. Hübner and coworkers used this scheme to determine the donor and acceptor transition dipoles in individual molecules, which is crucial to reliable distance determination based on FRET [50]. Forkey and coworkers used four different excitation polarizations in a total internal reflection scheme to measure the structural dynamics of the light chain domain of brain myosin V with a time resolution of up to 20 ms and without the need of any fitting procedure [25]. Nearly at the same time Vacha and Kontani presented a set-up combining a TIRF-illumination scheme with epi-fluorescence detection [101]. They also achieved an orientation determination without additional fitting procedures. In 2004 Debarre and coworkers reported that so called out-of-plane molecules, where the absorbing dipole coincides with the z-axis, can be detected more easily if amplitude and phase masking is applied to the input beam [12]. In a theoretical work, Fourkas predicted that comparing the fluorescent light intensities of three polarization directions would be sufficient to determine ϕ and θ [26].

Even though a number of methods was proposed for a full three-dimensional orientation determination of the absorption/emission dipole of single molecules, yet no fast easy-to-use approach is available. This problem will be addressed in chapter 5.

2.7 Geometrical confinement of diffusion

Single molecule detection of freely diffusing molecules suffers from two limitations. First, the transit time of the freely diffusing molecules through the confocal volume restricts the timescale of internal dynamics that can be explored. It is obvious that the longer a single molecules stays within the confocal focus the more photons can be detected from that specific molecule. Second, in a typical single molecule experiment in solution, the concentration of sample molecules is limited to less than one nanomol per liter to keep the probability of double occupancy low. However, systems that involve ligand binding or chemical change do often require micromolar or higher reagent concentrations [58]. Unfortunately, both limitations mostly interact with each other: Reducing the effective excitation/detection volume will lead to shortened transit times of the diffusing molecules.

The excitation/detection volume can be reduced in two different ways. One way is to reduce the excitation volume, where different methods have been proposed:

STED: The stimulated emission depletion was theoretically described by Hell and Wichmann in 1994 [41] and gained a lot of attention after its experimental realization [40, 53]. This technique consists of a conventional confocal excitation spot which is overlapped with a STED spot featuring a central naught. The STED spot is created by a pulsed laser with higher wavelength than the excitation wavelength and a $\lambda/2$ wave plate in the center of the beam and efficiently depletes the first excited state of a fluorophore at high intensities in its accessible volume. Therefore, the effective excitation spot is drastically minimized to 0.67 attoliter (10^{-18} l) and an optical resolution of around 30 nm can be obtained, which is far beyond the diffraction limit.

TIRF: In a total-internal-reflection-fluorescence scheme a large angle of the incident laser light excludes light propagation trough the glass/water interface. However, evanescent fields can enter the sample volume [42, 93]. The excitation volume is reduced by the fact that the penetration depth of the evanescent field in an aqueous solution is less than 200 nm.

SNOM: Similar to TIRF the direct light propagation in a scanning near-field optical microscope is prevented and only evanescent fields can enter the volume of interest [5]. In SNOM a tapered fiber tip with a diameter of less than 100 nm is covered with a metal at the side to fulfill this requirement.

Zero-mode waveguides: Zero-mode waveguides consist of sub-wavelength holes in a thin metal film deposited on a glass substrate. Again, the propagation of light through the metal film is forbidden and only evanescent fields occur within the holes [59]. With this method observation volumes of zeptoliters (10^{-21} l) can be achieved. Moreover, Samiee and coworkers derived an empirical FCS model accounting for one-dimensional diffusion within the tubes and used this technique to measure oligomerization of the bacteriophage λ repressor protein at micromolar concentrations [82].

Besides reducing the excitation volume with the methods described above, restricting the accessible space of the detectable diffusing fluorophores is another possible strategy for efficient single-molecule detection. An example from a biological system are dendrites of cultured neurons [31, 30]. These dendrites are cellular extensions of the neurons, where the majority of input to the neuron occurs. They feature a thickness (diameter) of less than 1 µm and a length of several tens of micrometers. Other examples of reducing the effective detection volume are presented in the following: **1)** Cone-shaped micro-capillaries with an inner diameter of less than 1 µm were used to confine the diffusion of single molecules [111]. The flow of the conjugates was established using electrokinetic forces. Due to the fact that the path of motion of the molecules is confined and thereby known, the obtainable signal-to-noise ratio is increased compared with measurements in free solution [15]. Sauer and coworker proposed the use of micro-capillaries for DNA sequencing [84]. **2)** Mesostructured molecular sieves were used to observe the translational diffusion of single terrylenediimide molecules [88]. **3)** In recent years, nanofluidic devices for single molecule detection fabricated by lithographic methods have gained more and more attention [64]. This is mainly attributed to the availability of advanced lithographic techniques such as electron beam lithography, reactive ion etching et cetera. Han and coworkers reported on the separation of long DNA molecules using entropic trap arrays [38] and Foquet and coworkers showed the focal volume confinement by single fluidic channels featuring a channel width down to 350 nm [24].

Even tough a reduction of the effective detection volume can be achieved with several methods, it remains a challenge to combine reduced detection volumes with increased observation time.

Chapter 3

Materials and methods

Overview

Whereas the last chapter covered different concepts of SMS relevant to this thesis, this chapter is aimed at giving a more detailed description of the applied methods. Section 3.1 describes the preparation of self-ordered porous alumina, which will be used as a host material to confine the diffusion of single molecules. Section 3.2 deals, on the one hand, with the detailed description of the SCOM set-up and, on the other hand, with configurations for confining the diffusion. The fluorescent probes, which will be used in the experiments, are introduced in section 3.3. The characterization of the Monte-Carlo simulations is presented in section 3.4. These simulations will be used for comparison with experimental findings, and therefore a strong relationship to the experimental conditions is required.

3.1 Self-ordered porous alumina

Self-ordered porous alumina was prepared by a two-step procedure following the procedures described elsewhere [65, 60]. Using 0.3 M sulfuric acid solution for the second anodization yields pores with a diameter of 25 nm and a depth that can be adjusted by the anodization time. The pore growth rate is about 5 µm/min. After anodization, the pores were widened to 35-40 nm, as determined by scanning electron microscopy (figure 3.1), by isotropic etching with 0.3 M oxalic acid for 1 h at 30 °C. Thus, the porosity of the membrane increased from 10% to around 20-25%. The underlying aluminum substrate was removed by a selective wet-chemical etching step with a mixture of 1.7 g $CuCl_2 \cdot H_2O$, 50 ml of a 37 wt-% aqueous HCl solution and 50 ml deionized water. The surface of the alumina membranes was protected either by a polymeric coating or by preventing direct exposure of the alumina membrane to the etching solution. Additionally, the barrier oxide at the pore bottoms was removed by treating the membrane with 10% phosphoric acid at 30 °C for a few minutes.

It was shown that porous alumina shows intrinsic photoluminescence whose origin is still a matter of debate [48]. Nevertheless, it was shown that the fluorescence of solubilized dye molecules inside porous alumina membranes can be detected and that the Fabry-Perot effect can be used to calculate the membrane thickness assuming an effective medium with a refractive index of $n = 1.63$ for the case of a 10% porosity and water-filled pores [48].

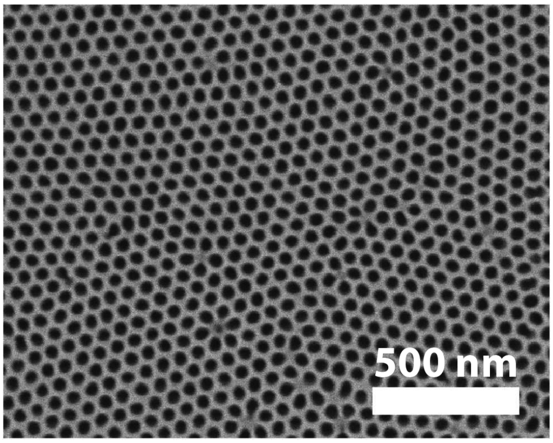

Figure 3.1: Top view of ordered porous alumina as imaged by a scanning electron microscope. The mean pore diameter is 35-40 nm.

3.2 The scanning confocal optical microscopy set-up

Measurements were performed using different confocal microscopes. The setup in Prague, which was used for diffusion studies of Alexa Fluor 488 and eGFP was described in detail elsewhere [4]. The experimental set-up in Halle is based on a home-build scanning confocal optical microscope. Here, I will give a general overview of the capabilities with the latter set-up. Different lasers were used for excitation, solid-state lasers operating at 488 nm (Protera, Novalux) or pulsed lasers operating at 470 nm and 635 nm (LDH-P-470 and LDH-P-635, Picoquant). The pulsed lasers are controlled by a driving circuity (PDL-808 driver, Picoquant) and the repetition rate can be changed up to 40 MHz with a pulse width lower then 100 ps. In the case of dual laser excitation, dichroic mirrors allow the superposition of the laser light, which is then passing a $\lambda/2$ and a $\lambda/4$ filter in order to control the polarization of the laser light. The light is coupled into an optical fiber, which provides a point source at their end. The light from the fiber output was collimated by a 4x microscope objective and reflected off either a multichroic beam-splitter (z405/488/633, Chroma) or a 488 nm beam-splitter. Excitation light was focused by a microscope objective (Nikon CFI Plan Apochromat 60x1.25 water or CFI Plan Apochromat 100x1.4 oil). A piezo-driven stage (P-734, Physik-Instrumente) operated in closed-loop allowed positioning of the focal spot with nanometer precision. Here, the x- and y-direction can be adjusted by moving the cover glass in respect to the objective, whereas the focus in the z-direction is adjusted by moving the objective.

Fluorescent light collected by the microscope objective passed several filters before being focused onto the detectors. Depending on the experimental conditions, different filters were used: a long-pass filter suppressing the 488 nm laser (HQ500LP, Chroma), bandpass filters (HQ532/70 and HQ650/100, Chroma) and a longpass filter (HQ650LP, Chroma). For FRET experiments, the emission was split by a dichroic mirror (595DCXR or 570DCXR, Chroma) into donor and acceptor components. For anisotropy or cross-correlation experiments, the emission was split by a polarizing- or a 50/50 beamsplitter. Apochromatic lenses with a focal distance of 500 mm were used to focus the light onto the active area of the single-photon counting modules (SPCM AQ14, Perkin-Elmer). Thereby, the active areas served as the confocal pinholes. Pulses from the detectors were fed into a TCSPC board (TimeHarp200, Picoquant) operating in the time-tagged time-resolved (TTTR) mode with a timing resolution of 35 ps for recording the fluorescence decay and 100 ns resolution for recording photon arrival times. The whole microscope was controlled by a programmable digital signal processing unit (ADWin Gold, Jäger) and home-written software (LabView, National Instruments).

Set-up for probing diffusion in porous alumina

Figure 3.2 shows the schematic cross-sectional diagrams of three different configurations used for probing the diffusion of molecules inside self-ordered porous alumina membranes. In all cases, the membrane was glued onto a glass tube with a diameter of around 4 mm and a height of 5 mm to 12 mm using epoxy resin. Beside the easier handling of the brittle membrane, the tube can be used as a chamber for the sample solution as long as membranes with closed bottom are used. Figure 3.2 **a+b)** shows membranes with a closed bottom, where the membranes are optically coupled to the cover glass either by immersion oil or by water to match the requirements for the objective in use. In figure 3.2 **c)**, the glass tube with the opened membrane is attached to a linear actuator (M-230.10, PI). The linear actuator has a travel distance of 2 cm and allows driving the glass tube out of the (larger) sample chamber.
Fixing the membrane with respect to the cover glass as shown in 3.2 **a+b)** enables adjusting the focus by the piezo-driven stage freely in all three dimensions, whereas the focus as shown in figure 3.2 **c)** can only be moved in z-direction, with respect to the membrane. Even if the positioning of the membrane in the third case is more difficult, the advantage is that the measurements in free solution are not disturbed by the long optical path as it occurs in the first cases. In addition, diffusion through the membrane can be investigated. The glass tubes in figure 3.2 **a+b)** are pushed to the coverslide using a clamp (not shown in the diagrams) in order to minimize the distance between the cover slide and the membrane. In conclusion, all three possibilities to mount the membrane have their advantages and disadvantages and it has to be

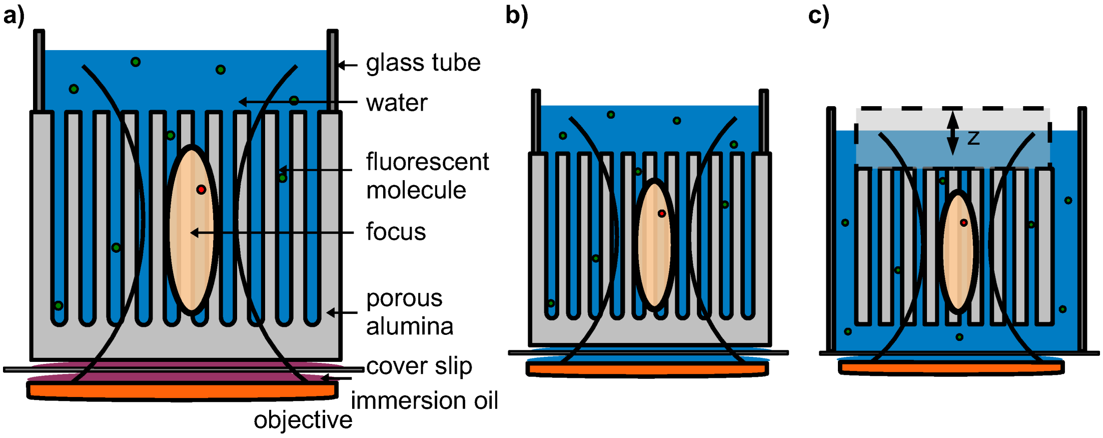

Figure 3.2: Schematic cross-sectional diagrams of the three different configurations used for diffusion measurements. In all cases, the membrane was glued to a glass tube. **a+b)** The glass tube is acting as sample chamber in the case of a closed pore bottom. **a)** The membrane is coupled to the cover slip using immersion oil (oil-immersion objective), **b)** the membrane is coupled to the cover slip using water (water-immersion objective). **c)** the glass tube was attached to a linear actuator to adjust the spacing between the membrane and the cover slip. For measurements inside the membrane, the focus of the objective was moved inside the membrane (view from the cover slip), for measurements in solution the focus was below the water/membrane interface.

decided from experiment to experiment which configuration should be used.

3.3 Fluorescent probes

In this section, the different fluorophores used in this thesis are introduced.

The Alexa Fluor dye series are fluorescent dyes which are covering the whole absorption/emission spectrum from the ultraviolet until the near infrared range [74]. The dyes are known for water solubility, *pH* insensitivity between *pH* 4-10, high quantum yield, high photostability, and a low intersystem-crossing rate [49]. In comparison to other chemically similar dyes as Fluorescine and Rhodamine, the Alexa dyes contain sulfonate (RSO_2O^-) groups so that they are negatively charged and hydrophilic. The diffusion coefficient for Alexa Fluor 488 in aqueous solution is $D = 2.8 \cdot 10^{-6}\text{cm}^2/\text{s}$ (measured against the chemically similar dye Rhodamine 6G as a reference [62]).

Perylene monoimide (PMI) is a dye which is solvable in toluene. A co-solution of poly(methylmethacrylate) and PMI in toluene was spin casted as a thin polymer film onto a microscope cover slip for three-dimensional orientation determination.

The wildtype green fluorescent protein (GFP) is a natural protein from the jellyfish *Aequoria victoria* and consists of 238 amino acids [6, 73]. GFP (molecular weight $M = 27\,\text{kDa}$) forms a barrel-like structure about 2 nm in diameter and 4 nm in height surrounding the p-hydroxybenzylidene imidazolinone fluorophore, which consists of three aminoacids, namely serine at position 65, tyrosine at position 66, and glysine at position 67. In order to increase the fluorescence intensity of the chromophore, two amino acids were substituted [11]: phenylanaline at position 64 was replaced by leucine (F64L) and serine at position 65 was replaced by threonine. This mutant is called the enhanced green fluorescent protein (eGFP) and has a main absorption maximum around 489 nm. EGFP was expressed as a $(\text{His})_{10}$ fusion using the pET19b-EGFP expression plasmid in E.coli BL21 (DE3) cells at 25°C and purified as described in reference [63]. In recent years (e)GFP was widely studied in the field of single molecule spectroscopy [100]; the diffusion coefficient was determined as $D = 8.7 \cdot 10^{-7}\text{cm}^2/\text{s}$ with a corresponding Stokes radius of $\alpha = 2.82\,\text{nm}$ [97]. Haupts and coworkers studied the fluctuations in fluorescence of eGFP as a function of the pH-value [39], and the fluorescence quantum yield was determined to $\Phi_f = 0.6$ [75]. Suhling and coworkers showed that the fluorescence lifetime of eGFP can be used to monitor its environmental refractive index [96].

Barstar is a small protein (molecular weight $M = 10.2\,\text{kDa}$) consisting of 90 amino acids and acting as the biological inhibitor of the enzyme barnase, which is a ribonuclease from the bacteria *Bacillis amyloliquefaciens*. Even if the folding pathway is rather complex, Barstar behaved as a two state folder in equilibrium studies [32, 85]. Here, the Barstar variant pWT was used, which was labeled with Alexa Fluor 488 as the donor and Alexa Fluor 594 as the acceptor. The doubly labeled protein was prepared according to procedures reported in reference [45].

3.4 Monte-Carlo simulations

A tight interplay between simulations and experiments can be very advantageous. Whereas in a single molecule experiment one often has to deal with a mostly inseparable superposition of

different effects, simulations can address them individually. Moreover, simulations offer the possibility both to test simplified assumptions and to change parameters, which are sometimes not directly accessible under experimental conditions.
The basic concept of Monte-Carlo simulations will be explained using the differential equation for one-dimensional diffusion, which describes the movement of single particles along a straight line:

$$\frac{\partial}{\partial t}\rho(x,t) = D\frac{\partial^2}{\partial x^2}\rho(x,t), \tag{3.1}$$

where $\rho(x,t)$ is the probability density of finding a particle at a certain place at a certain time and D the diffusion coefficient. Assuming further that at time $t = 0$ the particle is located at a defined place $x = 0$

$$\rho(x,t=0) = \delta(x), \tag{3.2}$$

the solution of the diffusion equation can be given as

$$\rho(x,t) \propto \frac{1}{(4\pi Dt)^{1/2}}e^{-x^2/4Dt}. \tag{3.3}$$

Whereas the mean position of the particle $< x >$ remains constant, the variance, which describes the mean square displacement of the particle, is a function of time

$$\mathrm{Var}(x) = 2Dt. \tag{3.4}$$

To calculate the movement of a particle within a certain time t, the Monte-Carlo algorithm draws a random number out of Gaussian probability distribution with the variance introduced above. In this work either C/C++ or the internal Igor programming language (similar to C/C++) was used for programming purposes. The random number generators are described in reference [76].

Simulations for diffusion and FRET experiments

As mentioned above, Monte-Carlo simulations offer the possibility to model experiments ab initio and are commonly used in the field of single molecule spectroscopy [72, 109]. We start with the random walk model for a single molecule in absence of any flow, drawing for each time step Δt a Gaussian distributed mean free path $\Delta x_i = \sqrt{2D\Delta t}$ for each of the possible directions x, y, z in a Cartesian coordinate system. The movement of the molecule is restricted to a cylinder with adjustable size. This has the advantage that the modeling of the apparent dimensionality of diffusion is quite simple:

apparent 1D diffusion the radius of the cylinder is small and the height large compared to Δx_i

apparent 2D diffusion the radius of the cylinder is large and the height is small compared to Δx_i

apparent 3D diffusion the height and the radius of the cylinder are large against Δx_i

Whereas in the case of apparent 3D diffusion the influence of the boundary conditions can be neglected as long as the cylinder is much larger than the detection focus, the boundary conditions become crucial for the case of apparent 1D diffusion. The simulations are mainly focused on the 1D case, with long pores aligned along the z-axis. For this reason, the boundary conditions in the x- and y-plane are fixed: each movement, which would cause the molecule to leave the cylinder, is discarded. For the z-direction (the cylinder axis), three boundary conditions can be applied: **1)** if the molecule would leave the cylinder, the movement is discarded (periodic boundary condition); **2)** if the molecule diffuses out of the top side of the cylinder, it vanishes and a new molecule enters the cylinder with a certain probability; **3)** if the molecule diffuses out of the cylinder at one end, it re-enters the cylinder at the opposite end. The second boundary condition is used to simulate the experimental conditions as described in section 3.2 for a membrane with a closed pore bottom.

If the fluorescent molecules diffuse through a laser focus they are absorbing photons from the laser light and emitting light with a higher wavelength. The number of detectable photons N_{D} during time Δt from one molecule is a complex function [109]

$$N_{\mathrm{d}} = \kappa \cdot \sigma_{\mathrm{abs}} \cdot q_{\mathrm{D}} \cdot q_{\mathrm{f}} \cdot \Delta t \cdot \frac{I_{\mathrm{exc}}(r,z)}{e_{\mathrm{phot}}} \cdot \mathrm{CEF}(r,z), \tag{3.5}$$

where κ is the instrument detection efficiency, σ_{abs} is the absorption cross section, q_{D} is the quantum efficiency of the detector, q_{f} is the quantum efficiency of the fluorophore , $I_{\mathrm{exc}}(r,z)$ is the Gaussian-Gaussian-Lorentzian excitation profile (including the laser intensity), $e_{\mathrm{phot}} = hc/\lambda$ is the energy of one photon (h is Planck's constant, c is the speed of light, and λ the wavelength of the photon), and, finally, CEF is the collection efficiency function. Two simplifications will be made: first, as it has been mentioned in chapter 2.5, the convolution of $I_{\mathrm{exc}}(r,z)$ and $\mathrm{CEF}(r,z)$ can be approximated by three-dimensional Gaussian distribution ($r^2 = x^2 + y^2$) [80]

$$I(r,z) = \frac{1}{e_{\mathrm{phot}}} \cdot I_{\mathrm{exc}}(r,z) \times \mathrm{CEF}(r,z) = I_0 \exp\left(-2\left(\frac{r^2}{w_0^2} + \frac{z^2}{z_0^2}\right)\right), \tag{3.6}$$

with w_0 as the width of the short half axis and z_0 as the width of the long half axis, second, some parameters will be combined to a parameter called simulated brightness B_{Sim}

$$B_{\mathrm{Sim}} = \kappa \cdot \sigma_{\mathrm{abs}} \cdot q_{\mathrm{D}} \cdot \Delta t \cdot I_0. \tag{3.7}$$

The parameter B_{Sim} will be adjusted in such a way that the molecular brightness B from the FCS analysis (B equals the overall number of detected photons per second divided by the apparent particle number N as obtained from the auto-correlation function, see chapter 2.5) matches the experimental conditions. The emission of photons after excitation of the fluorophore is following a Poisson distribution $\mathrm{P}(m)$, with an average value m. This shot-noise nature of photon emission is included by calculating the number of detectable (emitted) photons according to

$$N_{\mathrm{d}} = \mathrm{P}\left(B_{\mathrm{Sim}} \cdot q_{\mathrm{f}} \cdot \exp\left(-2\left(\frac{r^2}{w_0^2} + \frac{z^2}{z_0^2}\right)\right)\right). \tag{3.8}$$

Only if the quantum efficiency of the fluorophore q_f is set to unity, N_{d} can be interpreted as the number of absorbed photons, even if possible losses of photons after emission are already taken into account. For comparison, N_{abs} is defined as the number of absorbed photons. According to chapter 2.1, the molecule in the first excited state can decay on different pathways to the ground state. Here, each excited molecule adopts the triplet state with a certain probability. The lifetime of the triplet state is given by a time constant. During this time the molecule does not emit any photon. The bleaching of fluorophores is not included in the simulation, but can be implemented easily. Other non-fluorescent decays are included by using q_{f}. If excited molecules do not emit fluorescence, the photon is discarded, so that $N_{\text{d}} \leq N_{\text{abs}}$.

Doubly labeled molecules/proteins bear two excitable dyes serving as a donor and an acceptor for FRET. This is described in chapter 2.4. Both dyes can be handled as described above, but, additionally, the ability of the donor to transfer energy to the acceptor has to be taken into account. The rate of the energy transfer depends on the Förster radius of the dye pair and their distance to each other. Using equation 2.11, a probability for the occurrence of an energy transfer is calculated. To discriminate between the dyes, the intensities from the donor and the acceptor are stored in different detection channels, namely a green and a red channel. Moreover, the probability of crosstalk is implemented. Crosstalk occurs, if the donor emits light into the acceptor channel instead of the donor detection channel. FRET is called a spectroscopic ruler for conformational changes of proteins [105]. Proteins can undergo conformational changes such as folding and unfolding, which are experimentally triggered by temperature or urea [79, 86]. In any case, the conformational changes in a two state model are fully described by two rates, one from the folded to the unfolded state and vice versa. These changes result into two different donor to acceptor distances, which influence the probability of the energy transfer.

In order to simulate the time-resolved fluorescence correlation spectroscopy (see section 2.5), every fluorophore is additionally characterized by a time constant which represents the fluorescence decay rate.

Under the experimental conditions associated with the use of porous membranes as a matrix confining the probe molecules, more than one cylinder is in the detection focus. This is implemented by an hexagonal array of pores around the initial cylinder with a preliminary defined pore to pore distance. Every simulated molecule is randomly assigned to one of these pores and the distance $r_{0,i}$ from the original cylinder is stored as an offset value. In equation 3.8, r is replaced by $r + r_{0,i}$, which leads to a decreased excitation/detection probability of the molecule according to the instrument response function.

After explaining the implemented mechanisms, the "work-flow" of the simulation will be elaborated in more detail. At first, different particle sets are defined (e.g. free dye, proteins containing a donor dye or an acceptor dye only, doubly labeled proteins,...). Each particle set consists of a certain number of particles. Then, a set of specific data is assigned to each single particle, including, for example, position, number and nature of the attached chromophores, and the conformational state. After allocating the particles, the first outer loop count up the simulated time with a time increment of 1 µs. Within this loop, all particles are moved and the probability of photon absorption is calculated. If absorption takes place, the excited state can relax via emission of a photon, intersystem crossing (triplet), non-radiative decay or resonance energy transfer. The generated data files have the same file structure as those obtained from the experiments. All analyzing software tools can be used both for simulations and experiments in the very same way.

Chapter 4

Fluorescent molecules diffusing in confinement

Overview

In this chapter the nanoscale-confined diffusion of fluorescent probe molecules inside self-ordered alumina nanopores is studied for the case that the long axis of the pores coincides with the optical axis of a confocal microscope. Section 4.1 presents the experimental results. Autocorrelation and fluorescence lifetime analysis of the fluorescence signal are used as efficient tools to study macromolecules in a channel-type confinement. Section 4.2 deals with the question if water- or oil-immersion objectives are favorable for measurements in porous alumina. Monte-Carlo simulations of two-dimensional confinement (which leads to one-dimensional diffusion) and for comparison in unconfined systems (which leads to three-dimensional diffusion) are presented in section 4.4. Comparing these simulations with the experimental findings allows developing a more detailed picture of diffusion within confinement. In section 4.3 the adsorption behavior of eGFP at the pore walls is discussed as a function of the pH-value of the used buffer. First measurments of the fluorescence resonance energy transfer of doubly labeled proteins in porous alumina are presented in section 4.5.

4.1 One dimensional diffusion in porous alumina

The alignment of the long axis of the pores with the optical axis of the confocal microscope as it has been described in section 3.2 forces the probe molecules to diffuse parallel to the long axis of the laser focus, which possesses an ellipsoidal shape with short half axis $w_0 \simeq 250\,\mathrm{nm}$ and long half axis $z_0 \simeq 1000\,\mathrm{nm}$ (checked by scanning fluorescent latex-beads). The cover glass thickness correction capability of the microscope objective was used to compensate for the mismatch of refractive indices between water ($n_{\mathrm{H_2O}} = 1.33$) and the water-filled membrane treated as an effective medium with $n_{\mathrm{Alox}} = 1.57$ [48], which is possible due to the similarity of the refractive indices of glass ($n_{\mathrm{Glass}} = 1.52$) and water-filled porous alumina. This will be elaborated more in detail in section 4.2.

As long as the pore diameter is much smaller than the size of the laser focus, only movements of the molecules in the z-direction lead to intensity fluctuations. The measurements were per-

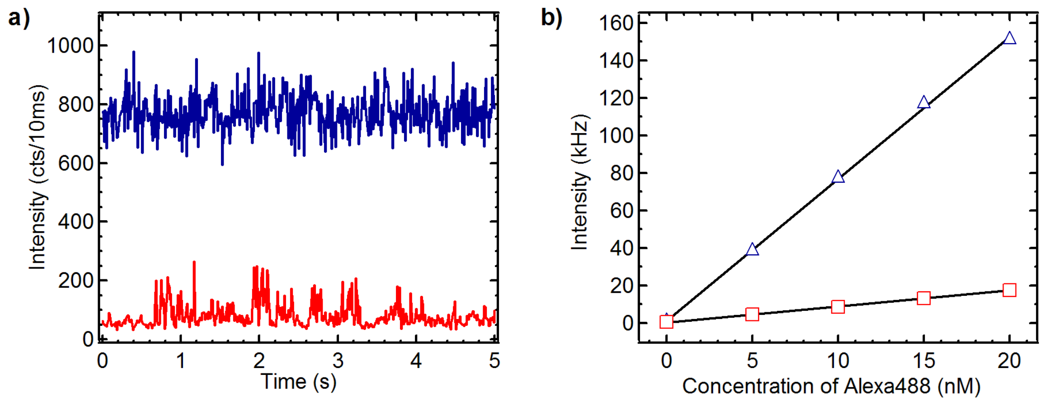

Figure 4.1: **a)** Transient fluorescence intensities for the dye Alexa Fluor 488 10 nM in bulk solution (top trace) and nanopore-confined solution (bottom trace) excited at 470 nm with a power of 8 μW. **b)** Average intensity for different dye concentrations in bulk solution (-△-) and inside the nanopores (-□-). The count rate increases linearly (solid line) with the concentration of the dye in the solution.

formed using the set-up described in reference [4] and using a linear actuator for positioning of the membrane with respect to the focus of the confocal microscope (see section 3.2 for details). For recording time traces at a stationary point, the focus was either placed 10 µm within the membrane or 10 µm below the membrane. This scheme allows recording of transients for one and the same stock inside the membrane and in free solution. Prior to any measurement, the membranes and the chamber were incubated over night with 107 µM bovine serum albumin in order to prevent the fluorescent molecules from unspecific adsorption. After incubation, the membranes were rinsed with deionized water.

For the first measurements, the 10 mM phosphate buffered saline (PBS) buffer (+137 mm NaCl, +2.7 mm KCl, *pH* 7.4, Sigma–Aldrich). PBS buffer was filled into the chamber and the background intensity of the buffer and the buffer-filled porous alumina membrane was recorded. Both background count rates were smaller than 1000 photons per second ($\hat{=}$1 kHz). Some microliter of a 100 nM stock solution of Alexa Fluor 488 were consecutively added to increase the concentration of the dye in the chamber. Figure 4.1 **a)** shows the transient fluorescence intensity for a 10 nM solution of Alexa Fluor 488 in buffer inside the membrane, and, for comparison, in bulk solution. The two transients clearly differ both in the average intensity, which is 77 kHz (770 photons/10 ms) in bulk solution and 9 kHz (90 photons/ 10ms) within the membrane, and their shape; the transient within the membrane shows a pronounced burst-like behavior. As shown in figure 4.1 **b)**, the detected intensity depends linearly on the dye concentration. The ratio between the slopes of the plots showing the fluorescence intensities inside the membrane and in the bulk as a function of the concentration is 1 to 9.

Similar behavior is found for eGFP, the second analyte that was investigated. Figure 4.2 **a)** shows a typical fluorescence transient for 10 nM eGFP in bulk solution and within the porous alumina membrane. In addition to the pronounced fluorescence bursts like those observed for Alexa Fluor 488 within the membrane, a slow decrease of the background signal was found. If the laser is switched off and on again, the background signal recovers and decays again. Again, as shown in figure 4.2 **b)**, the detected intensity depends linearly on the concentration of eGFP, but the ratio of the slopes in this case is only 1 to 4.

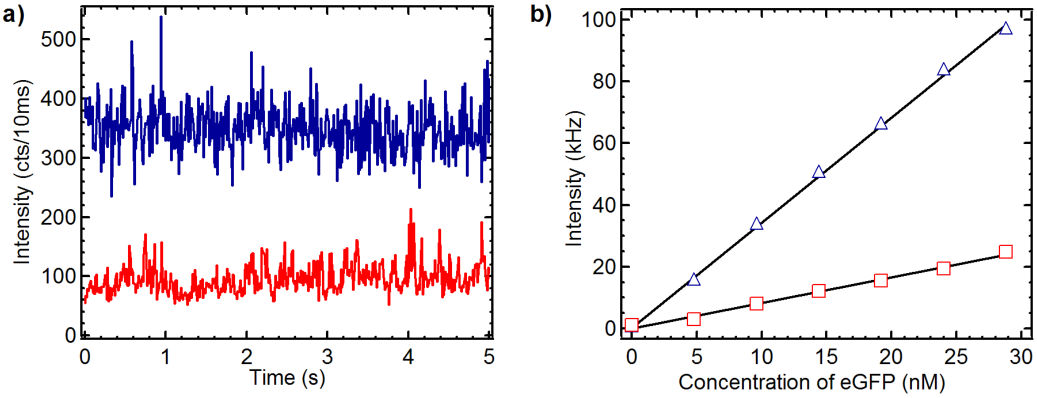

Figure 4.2: **a)** Transient fluorescence intensities for eGFP 10 nM in bulk solution (top trace) and nanopore-confined solution (bottom trace) excited at 470 nm with a power of 8 μW. **b)** Average intensity for different protein concentrations in bulk solution (-△-) and inside the nanopores (-□-). The count rate increases linearly (solid line) with the concentration of the dye in the solution.

The intensity drop inside the membrane could be caused by either one or a combination of the following effects: a lower average number of molecules in the detection volume, a reduced excitation intensity, a quenched emissive rate of the molecules or a reduced detection efficiency. The first effect concerns just the apparent concentration whereas the latter three would change the molecular brightness, i.e. the apparent fluorescence intensity per molecule. The actual reason will be elaborated in detail in the following.

The quantity related to the apparent concentration of molecules within the detection volume is the amplitude $G(\tau=0)=1+1/N$ of the auto-correlation functions (ACFs), which are shown in figure 4.3 **a)**. $G(0)$ is decreasing with increasing dye concentration, and is considerably lower in bulk solution than within the membrane. The obtained average number of dye molecules in the detection volume N is plotted versus the dye concentration in figure 4.3 **b)**. A linear dependence is obtained, where the slope for the bulk data is about 3 times the slope within the membrane. Therefore, the apparent particle number in the membrane is lowered by a factor of three, which is in reasonable agreement with the reduced detection volume inside the membrane assuming a porosity of 20-25%. Note that the intercept of the lines is essentially zero, which indicates the reliability of the method.

Figure 4.4 **a)** shows the ACF for 10 nM eGFP in bulk solution and within the membrane. Both functions have the same amplitude indicating an almost equal apparent number of molecules within the detection focus. As shown in figure 4.4 **b)**, this is the case for each concentration of eGFP.

It is known from literature that uncorrelated background, which is here assigned to immobilized eGFP molecules for the measurement inside the membrane, has a huge impact on the apparent mean number of molecules [54]. The assignment of the background signal to immobilized molecules is supported by the finding that the average count rate of eGFP is not reduced as much as for the Alexa dye. The integral intensity from membranes soaked with eGFP solution is thus the sum of diffusing molecules (as measured by FCS) and of immobilized molecules. Assuming the same reduction of the effective confocal volume within the membrane as for the Alexa dye, we can estimate the number of molecules causing the constant background.

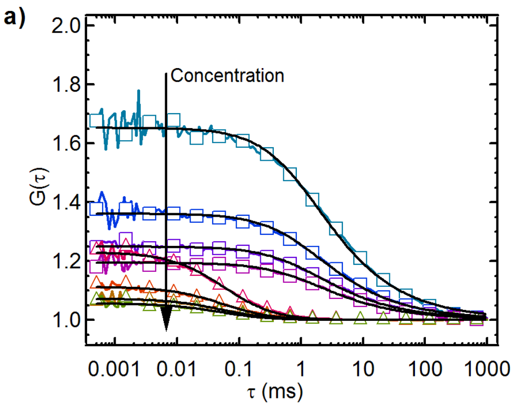

Figure 4.3: a) Intensity auto-correlation functions for transients of different concentrations of Alexa Flour 488 in bulk solution (△) and in the nanopores (□). The solid lines are fits according to equations 2.21 and 2.19 assuming three-dimensional and one-dimensional diffusion, respectively. **b)** Mean particle numbers N in the confocal volume as a function of dye concentration in bulk solution (-△-) and inside the nanopores (-□-). Straight lines represent linear fits.

The ratio between the fluorescence intensity reduction factors $r = I_{\text{bulk}}/I_{\text{Alox}}$ for the Alexa dye ($r_{\text{Alexa}} \approx 9$) and for eGFP ($r_{\text{eGFP}} \approx 4$) is $r_{\text{Alexa}}/r_{\text{eGFP}} \approx 2$. Therefore, it can be concluded that the total concentration of eGFP molecules in the confocal volume is two times the concentration expected from the effective concentration. In conclusion, the number of immobile molecules N_{immob} equals the number of mobile molecules N_{mob}. This conclusion can be further evidenced looking at the results from the correlation analysis. The apparent number of molecules N_{app} as measured by FCS in the presence molecules contributing uncorrelated background is given by [54]

$$N_{\text{app}} = \frac{(N_{\text{mob}} + N_{\text{immob}})^2}{N_{\text{mob}}}. \tag{4.1}$$

With $N_{\text{mob}} \approx N_{\text{immob}}$ one gets $N_{\text{app}} \approx 4N_{\text{mob}}$. This is in clear accordance with the experimental results: The apparent number of molecules in the focus for eGFP is by a factor of about 4 larger

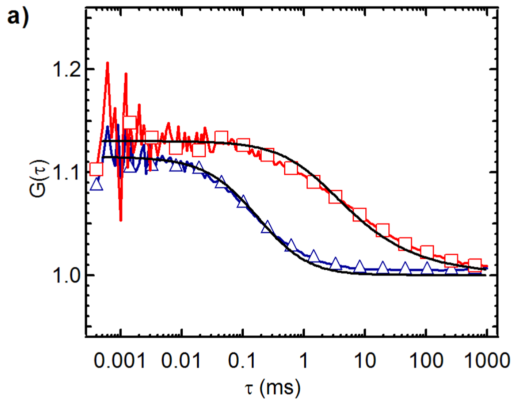

Figure 4.4: a) Intensity auto-correlation functions for transients of 10 nM eGFP in bulk solution (-△-) and in the nanopores (-□-). The solid lines are fits according to equations 2.21 and 2.19 assuming three-dimensional and one-dimensional diffusion, respectively. **b)** Apparent mean particle numbers N in the confocal volume as a function of eGFP concentration in bulk solution (-△-) and inside the nanopores (-□-). Straight lines represent linear fits.

than the value expected from the porosity of the membrane. On the other hand, assuming a tenth of a monolayer of BSA at the pore walls [57], one can estimate that some tens of thousands BSA molecules are located within the detection volume based on geometry considerations. The fraction of immobilized eGFP molecules related to the total amount of adsorbed protein is thus extremely small. Here, it is additionally assumed that the emitted fluorescence intensity is the same for diffusing and immobilized molecules, respectively, i.e., no fluorescence quenching is taken into account.

An important parameter in FCS is the molecular brightness, which is defined as the average intensity divided by the mean particle number N. The molecular brightness is influenced by changes in the excitation intensity and the detection efficiency, respectively, and by quenching of fluorescence. Figure 4.5 shows the average intensity as a function of the apparent particle number N for **a)** Alexa Fluor 488 and **b)** eGFP. Straight lines represent linear fits yielding the molecular brightness parameter; for Alexa Fluor 488 in bulk solution $B_{\text{bulk}}^{\text{Alexa}} = 8.3\,\text{kHz/molecule}$ and in the membrane $B_{\text{Alox}}^{\text{Alexa}} = 3.6\,\text{kHz/molecule}$. For eGFP, the corresponding numbers are $B_{\text{bulk}}^{\text{eGFP}} = 3.5\,\text{kHz/molecule}$ and $B_{\text{Alox}}^{\text{eGFP}} = 1.0\,\text{kHz/molecule}$. For Alexa Fluor 488, the molecular brightness is reduced by a factor of $R_{\text{Alexa}} = B_{\text{bulk}}^{\text{Alexa}}/B_{\text{Alox}}^{\text{Alexa}} = 2.3$. This is caused by the fact that the detection angle is lowered within the membrane. A water-immersion objective ($n_{\text{H}_2\text{O}} = 1.33$) featuring a numerical aperture of $N_A = 1.2$ has a half detection angle of $\alpha_{H_2O} = 64^\circ$ based on the equation

$$N_A = n \sin\alpha. \tag{4.2}$$

With the effective refractive index in the membrane of $n_{\text{Alox}} = 1.57$ the half angle amounts to $\alpha_{\text{Alox}} = 50^\circ$, which results in a decrease of the steradian of which photons can be detected. The ratio of these accessible solid angles for $\alpha_{\text{H}_2\text{O}}$ and α_{Alox} can be calculated according to the equation for the steradian

$$\Omega = 2\pi\left(1 - \cos\alpha\right). \tag{4.3}$$

The reduction of the detectable fluorescence within the alumina membrane can be calculated to be a factor of $R_\Omega = \Omega_{64^\circ}/\Omega_{50^\circ} = 1.7$, which is in reasonable agreement with the measured value for the Alexa dye ($R_{\text{Alexa}} = 2.3$). In the case of eGFP, the brightness was calculated with the apparent particle number $N_{\text{app}} = 2 * (N_{\text{mob}} + N_{\text{immob}})$. Taking only the real particle number ($N_{\text{real}} = N_{\text{mob}} + N_{\text{immob}}$) into account leads to $R_{eGFP} = 1.8$, which is in perfect agreement with the expectation of $R_\Omega = 1.7$.

In order to elucidate quenching effects due to pore-wall interactions, the fluorescence decay time of the dyes in the membrane was compared with the decay time in bulk solution. Contacts with the pore walls may lead to fluorescence quenching, which can be experimentally identified by a shortening of the fluorescence decay time. Besides quenching processes, the refractive index of the medium surrounding the emitter can modify the fluorescence lifetime τ_f via the radiative lifetime $\tau_0 = 1/k_{\text{rad}}$, which is inversely proportional to the square of the refractive index reading [94]

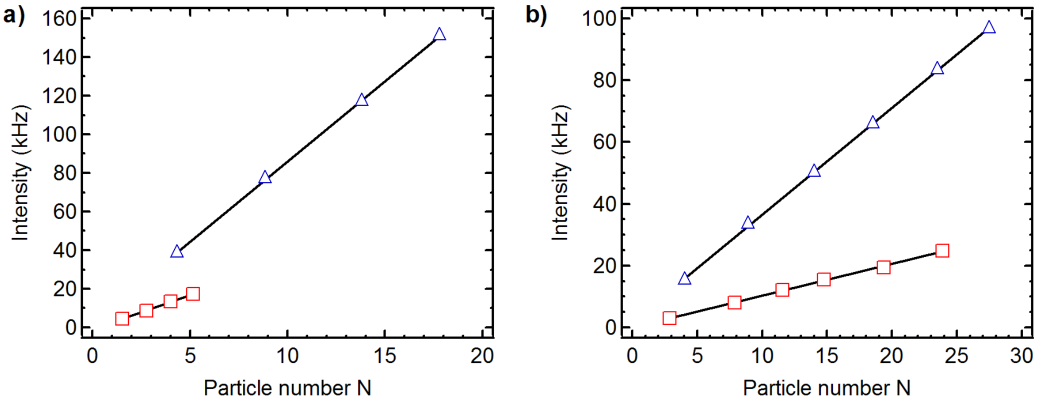

Figure 4.5: Average fluorescence intensity versus the particle number N in bulk solution (-△-) and in the nanoporous membrane (-□-) for different concentrations of **a)** Alexa Fluor 488 and **b)** eGFP. The solid lines represent linear fits, where the slope represents the moleculear brightness.

$$\frac{n_{\mathrm{M}}^2}{n_{\mathrm{H_2O}}^2} = \frac{\tau_{\mathrm{f,H_2O}}}{\tau_{\mathrm{f,M}}}. \tag{4.4}$$

For Alexa Fluor 488 the fluorescence decays follow a single-exponential law appearing as straight lines in the semilogarithmic plot in figure 4.6 **a)**. A decrease of the fluorescence lifetime from $\tau_{\mathrm{f,H_2O}} = 4.1\,\mathrm{ns}$ in bulk solution to $\tau_{\mathrm{f,M}} = 3.0\,\mathrm{ns}$ within the membrane was found for all dye concentrations. For Alexa Fluor 488 with its fluorescence quantum yield close to unity in solution, the fluoresence decay is nearly exclusively governed by the radiative rate k_{10} as discussed in section 2.1. With the refractive index of $n = 1.57$ for the water-filled membrane one can expect a fluorescence lifetime of $\tau_{\mathrm{f,M}} = 2.9\,\mathrm{ns}$ within the membrane, which matches the experimental result almost perfectly.

For eGFP, as it is shown in figure 4.6 **b)**, a mono-exponential fit model was applied, which reflects the shortening of the fluorescence decay due to refractive-index changes following Suhling's approach [96]. A fluorescence lifetime of $\tau_{\mathrm{f,H_2O}} = 2.6\,\mathrm{ns}$ in bulk solution and $\tau_{\mathrm{f,M}} = 2.2\,\mathrm{ns}$ in the membrane was obtained. The quantum yield of fluorescence $\Phi_{\mathrm{f}} = k_{\mathrm{rad}}/(k_{\mathrm{rad}} + k_{\mathrm{nrad}}) = k_{\mathrm{rad}} \cdot \tau_{\mathrm{f}}$ for eGFP is $\Phi_{\mathrm{f}} = 0.6$ [75]. Combining the Strickler-Berg formula with the definition of the fluorescence quantum yield,

$$\tau_{\mathrm{f,M}} = \left(\frac{\Phi_{\mathrm{f}}}{\tau_{\mathrm{f,H_2O}}} + \frac{1-\Phi_{\mathrm{f}}}{\tau_{\mathrm{f,H_2O}}} \frac{n_{\mathrm{M}}^2}{n_{\mathrm{H_2O}}^2} \right)^{-1}, \tag{4.5}$$

a fluorescence decay time in the membrane of $\tau_{\mathrm{f,M}} = 2.2\,\mathrm{ns}$ can be estimated, which is again in perfect agreement with the experimental result, indicative of the absence of quenching processes. At first, this finding is surprising because there are immobilized molecules in the membrane that might be prone to quenching. The chromophore of eGFP, however, is known to be shielded by the protein structure from the environment, thus preventing collisional quenching by pore-wall contacts. Let us now focus on the dwell time of the molecules in the focal volume, which is related to the decay of the ACFs in figure 4.3 **a)**. The solid lines represent fits to the experimental ACFs with the one-dimensional model using equation 2.19 for the signal measured inside the membrane and with the three-dimensional model using equation 2.21 in bulk

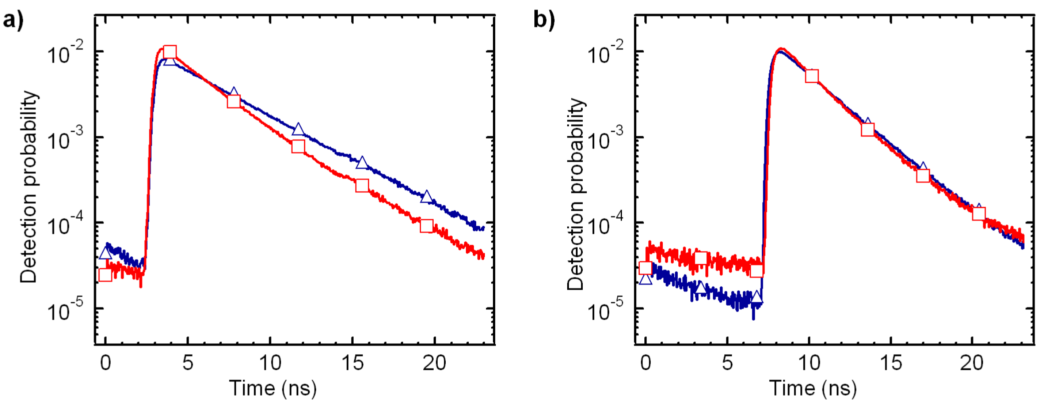

Figure 4.6: **a)** Fluorescence decay for 10 nM Alexa Fluor 488 in bulk solution (-△-) and in the nanoporous membrane (-□-). **b)** Fluorescence decay for 10 nM eGFP in bulk solution (-△-) and in the nanoporous membrane (-□-).

solution, respectively. All ACFs were corrected for afterpulsing by application of a temporal filter as described in section 2.5. The excellent agreement of the fitted curves and the experimental auto-correlation functions for the transients taken inside the nanopores is evidence of apparent one-dimensional diffusion. No long-time component is apparent in the ACFs, demonstrating the absence of sticking effects. Defining the diffusion time for the unconfined diffusion as $\tau_D^{3D} = \omega_0^2/4D$ and for one-dimensional diffusion as $\tau_D^{1D} = z_0^2/4D$, the ratio between the diffusion time in the one-dimensional case along z and in the three-dimensional case is just the square of the structural parameter s, which is defined as $s = z_0/w_0$ and amounts to $s \simeq 4$ in the microscope which was used. Therefore, one can expect a $s^2 = 16$ times longer diffusion time τ_D inside the membrane as compared to free bulk diffusion. The ratio between the visually easier to access ACF decay half times $\tau_{1/2}$, however, is even larger due to the different exponents of the diffusion terms. The fits of the model functions to the experimental ACFs yield diffusion times $\tau_D^{3D} = 54 \pm 3\,\mu s$ in bulk solution and $\tau_D^{1D} = 1003 \pm 30\,\mu s$ in the membrane with negligible variations between the different concentrations. The diffusion time τ_D^{1D} is thus 19 times longer than in free solution. This is in reasonable agreement with the applied model and indicates moreover that the diffusion time of Alexa Fluor 488 molecules is not affected by interactions between the analyte and the pore walls. The same holds for eGFP, where a 14 times increased diffusion time was found in the membrane as compared to bulk solution, which is indicating that the mobile fraction of the probe molecules is not slowed down by interactions with the pore wall. One can only speculate that the deviations of the experimental ACFs from the model functions in solution as well as under confinement for eGFP are related to the inherent photophysics of the eGFP chromophore [39].

4.2 Objectives: water-immersion versus oil-immersion

Water-immersion objective

All results in the previous section were obtained using a water-immersion objective with a correction ability for the cover glass thickness. Here, this correction ability is used to compensate

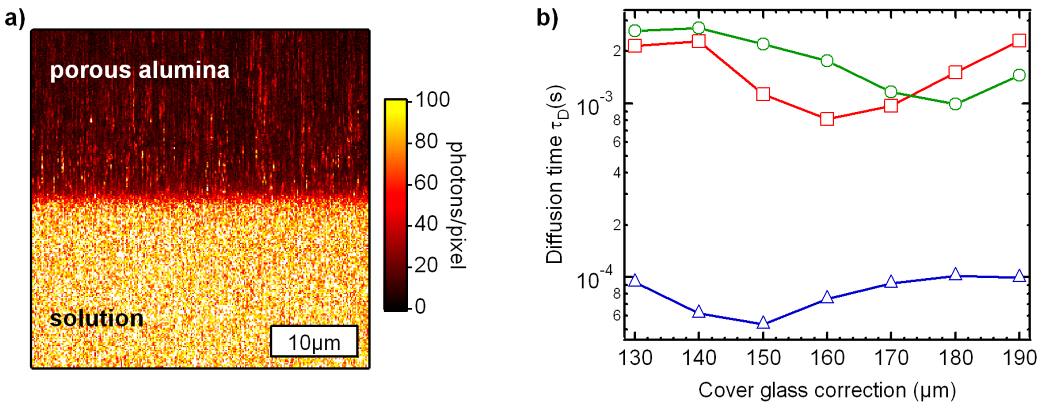

Figure 4.7: a) Fluorescence scanning image of Alexa Fluor 488 diffusing in solution and within the porous alumina membrane. The stripe-like features within the membrane correspond to the diffusion of the molecules along the pores (which coincides with the z- direction). **b)** Influence of the cover glass correction of the water-immersion objective on the diffusion time of 6.5 nM Alexa Fluor 488 diffusing in bulk solution 10 µm below the solution/membrane interface (-△-), 10 µm within the membrane (-□-), and 20 µm within the membrane (-◯-) . Note the logarithmic scale of the diffusion time.

the distortions of the focus in the alumina membrane, which are caused by a mismatch of the refractive indices of water $n_{\mathrm{H_2O}} = 1.33$ and the water filled membrane $n_{\mathrm{Alox}} = 1.57$. To elaborate this correction more in detail, an experiment was performed, where the diffusion time and the brightness was measured as a function of the specified objective cover glass correction. In contrast to the set-up used for the previous measurments as described in reference [4], the set-up described in section 3.2 has the ability to scan along the membrane. The excitation intensity was 10 µW at 470 nm. A polarizing beam splitter was used to split the fluorescent light into two detectors. This configuration allows for cross-correlating the signals without any need of applying an afterpulsing filter. Alexa Flour 488 was used as the fluorescent probe and the concentration of the dye was adjusted to 6.5 nM in PBS buffer. Due to the fact that the membrane was attached to a linear actuator whose position cannot be controlled via the x- and y-positioning stage, the image in figure 4.7 **a)** shows only a set of line scans along the z-direction, without any real change in the x- or y-direction. Nevertheless, several points should be noted: 1) as expected, the mean intensity per pixel in solution is larger than within the porous alumina, 2) there is no adsorption of Alexa Fluor 488 at the solution/membrane interface, which would result in a massively increased intensity per pixel at the interface and 3) within the porous alumina, strip-like intensity features are visible, which correspond to fluorescent molecules diffusing along the fast scanning axis of the focus.

Figure 4.7 **b)** shows the mean diffusion times calculated from the cross-correlation functions for three positions of the focus as a function of the cover glass correction. The focus was either placed 10 µm below the membrane, or 10 µm and 20 µm, respectively, within the membrane. The standard thickness of a cover glass slide is 150 µm, using this value for correction provides the smallest measurable diffusion time, which gives $\tau_D = 62$ µs in free solution. If the cover glass correction is changed, the diffusion time increases up to a factor of two. If the focus is placed 10 µm within the membrane, the diffusion time is minimized for a correction factor of 160 µm. Similar to the measurements in the previous chapters, the diffusion time within the membrane equals $\tau_D \simeq 1$ ms. Again, if the cover glass correction is changed, the measured

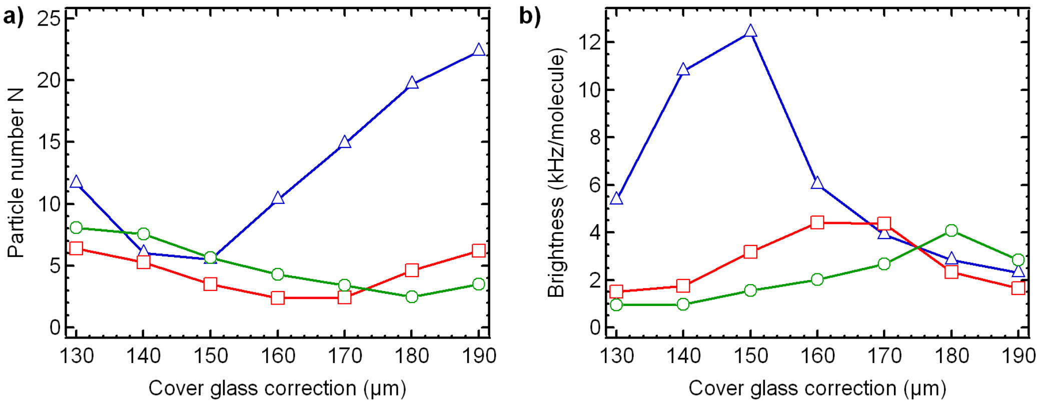

Figure 4.8: Influence of the cover glass correction of the water-immersion objective on **a)** the mean particle number N and **b)** the brightness B of 6.5 nM Alexa Fluor 488 diffusing in bulk solution 10 µm below the solution/membrane interface (-△-), 10 µm within the membrane (-□-), and 20 µm within the membrane (-○-). The minimized particle number and the maximized brightness for each line indicates the smallest obtainable focus as a function of the cover glass correction.

diffusion time increases. However, in contrast to the measurement in free solution, where the three-dimensional correlation fitting function is due to $D_{3\mathrm{D}} = w_0^2/4\tau_D$ mainly sensitive to the elongation of the focus in the x- and y-direction, the one-dimensional correlation fitting function is only sensitive to the elongation of the focus in the z-direction according to $D_{1\mathrm{D}} = z_0^2/4\tau_D$. If the focus is placed 20 µm within the membrane, the diffusion time is minimized using a cover glass correction value of 180 µm. This value is slightly higher than the value of 170 µm obtained by just adding the coverglass thickness and the depth within the membrane, which can be explained by the fact that the refractive index of water-filled porous alumina is slightly larger than that of the cover glass ($n_{\mathrm{glass}} = 1.52$).

As mentioned above, the diffusion time is not only sensitive to the dimensions of the excitation/detection focus. Additional useful parameters are the mean particle number N and the molecular brightness B, which is defined as $B = \mathrm{count\,rate}/N$. Figure 4.8 **a+b)** shows the mean particle number and the molecular brightness as a function of the cover glass correction factor for the three positions of the focus. Mainly, the lines are following the behavior of the diffusion time: if the diffusion time τ_D is minimized by the cover class correction, the particle number N is minimized, too, and thereby the brightness B is maximized. Let us take a closer look at the measurements in solution. If the value of the cover glass correction is between 170 µm and 190 µm, the diffusion time is more or less constant. In contrast, the particle number increases dramatically and therefore the brightness decreases. This finding can be explained by an expansion of the focus in z-direction and will be elaborated more in detail via Monte-Carlo simulations in section 4.4. Within the membrane, this effect (here on the expansion of the focus in the x- and y-plane) is too small to be clearly visible. In conclusion, the cover glass correction of the water-immersion objective provides a practicable tool to adjust the focus for measurements within porous alumina. Nevertheless, the mismatch of the refractive indices of water and water-filled porous alumina leads to an decreased molecular brightness within the membrane due to the reduction of the detection angle.

In contrast to the previous experiments in this section, the following experiment uses the experimental configuration shown in figure 3.2 **b)**, which allows for real scanning in the x- and

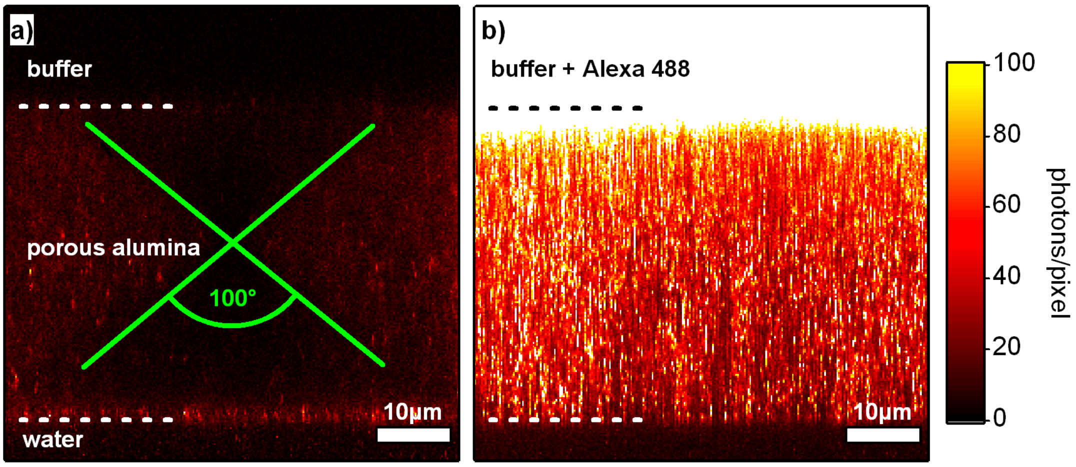

Figure 4.9: Color coded scanning images of a citrate buffer filled porous alumina membrane. The membrane was attached via pure water to the cover glass using an water-immersion objective for excitation and detection. The size of the image is 60 µm x 60 µm scanned with a resolution of 256 x 256 pixels and a time resolution of 1 ms/pixel. The dashed lines represent the buffer/membrane interface. **a)** Background intensity of the water filled membrane after bleaching for several minutes at the position of the crossed lines. The detection angle $2 \cdot \alpha$ is about 100°. **b)** After adding some micro liter of 130 nM Alexa Fluor 488 to reach a concentration of 6.5 nM in the solution, no adsorbing of the fluorescent protein at the water/membrane interface takes place. Moreover, this image was taken after recording a transient time trace within the membrane. No bleaching of molecules is visible.

z-plane. The excitation was performed at 40 µW using circulary polarizied laser light at a wavelength of 488 nm. A polarizing beamsplitter was used to split the fluorescent light into orthogonally polarized components. Figure 4.9 **a)** shows the background image of the buffer-filled membrane after taking a transient time trace at the crossing of the green lines. Laser irradiation leads to the bleaching of fluorescent contaminants in the alumina membrane. The bleached region can be used to estimate the detection angle according to $2 \cdot \alpha_{Alox} = 100°$ within the membrane, which is in perfect agreement with the theoretical calculated value in section 4.1. After addition of Alexa Fluor 488, the focus was placed at the center of the membrane to record a transient time trace. Subsequent recording of figure 4.9 **b)** shows the penentration of the membrane and the absence of a bleached region indicating a good mobility of the probe.

The main idea behind this measurement is shown in figure 4.10. Whereas in the previous part auto-correlation functions were calculated for different depths within the membrane using fixed correction settings of the water-immersion objective, here the correction was changed as a function of the depth within the membrane. Assuming a cover slide thickness of 150 µm, the collar ring of the objective was set to 150 µm. For each increase of the depth of the focus within the membrane (counted from the water/membrane interface), the collar ring was adjusted to the value of the cover slide plus the depth within the membrane. Indeed, as shown in figure 4.10 **a)**, the correction works sufficiently well. The diffusion time is around 1 ms in almost any depth. Only at higher depths and thereby close to the membrane/buffer interface deviations are clearly visible. These deviations can be attributed either to the non-ideal corrrection because of the higher refractive of the membrane compared to the cover slide or the beginning influence of the freely diffusing molecules above the membrane. Moreover, as shown in figure 4.10 **b)**,

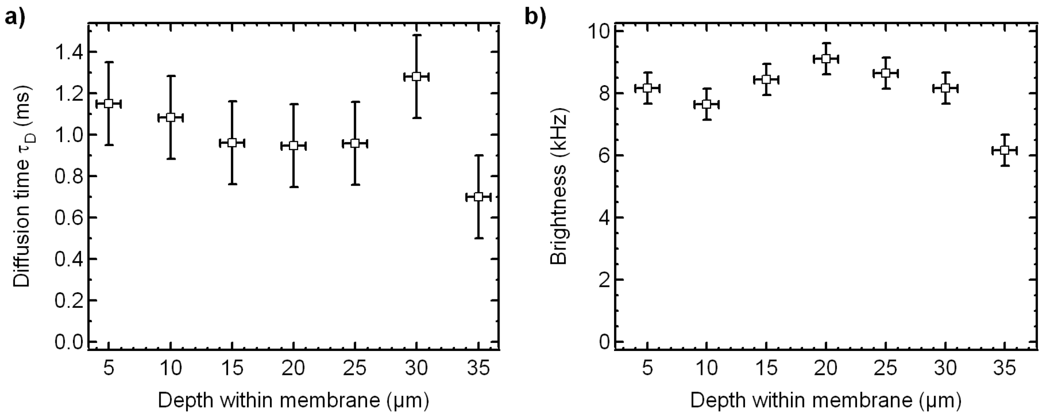

Figure 4.10: Alexa Fluor 488 diffusing within porous alumina using an water-immersion objective. **a)** diffusion time τ_D and **b)** molecular brightness as a function of the depth within the membrane (closed bottom), whereas the first water/membrane interface was set to zero. The correction ring of the water-immersion objective was set to 150 µm for the cover glass thickness plus the respective depth within the membrane.

the molecular brightness remains constant with increasing depth of detection in the membrane, demonstrating that the correction capability of the water-immersion objective can be used efficiently to compensate the spherical aberrations even in relatively large depths within a alumina membrane.

Oil-immersion objective

In order to overcome the problems caused by the decreased detection angle, I will now concentrate on the use of an oil-immersion objective instead of a water-immersion objective. The oil-immersion objective is corrected for measurements in objects with a refractive index of $n_{\text{Oil}} = 1.52$, which is close to the refractive index of the porous alumina membrane with $n_{\text{Alox}} = 1.57$. The oil-immersion objective has a numerical aperture of $NA = 1.4$, resulting in a detection angle of $2 \cdot \alpha = 2 \cdot 67^\circ = 134^\circ$.

In contrast to the experiments discussed above, where no adsorption of the fluorescent molecules at the solution/membrane interface occured, the following experiment shows a strong adsorption, thereby giving for example direct access to the detection angle. Figure 4.11 shows scanning images of a water-filled porous alumina membrane. This membrane was attached with immersion oil to the cover glass. The scanning area was 80 µm x 80 µm scanned with a resolution of 256 x 256 pixels and a time resolution of 1 ms per pixel. The laser power was adjusted to 60 µW at a wavelength of 488 nm. The background intensity of the system is shown in figure 4.11 **a)**. The intrinsic luminescence of the porous alumina membrane slightly exceeds the mean intensity in water. After adding some microliter of Barstar 488/594 solution in order to reach a concentration of 9 nM in the solution, figure 4.11 **b)** was recorded. The scanning along the pores took place from the right side to the left. If the scanning parameters are taken into account, the whole image is recorded in approximately one minute. This allows for imaging both the evolution of the adsorption of the molecules at the membrane/solution interface as indicated by the black arrow and the penetration of the membrane by the labeled protein as indicated by the green arrows. The count rate at the interface massively exceeds the range cov-

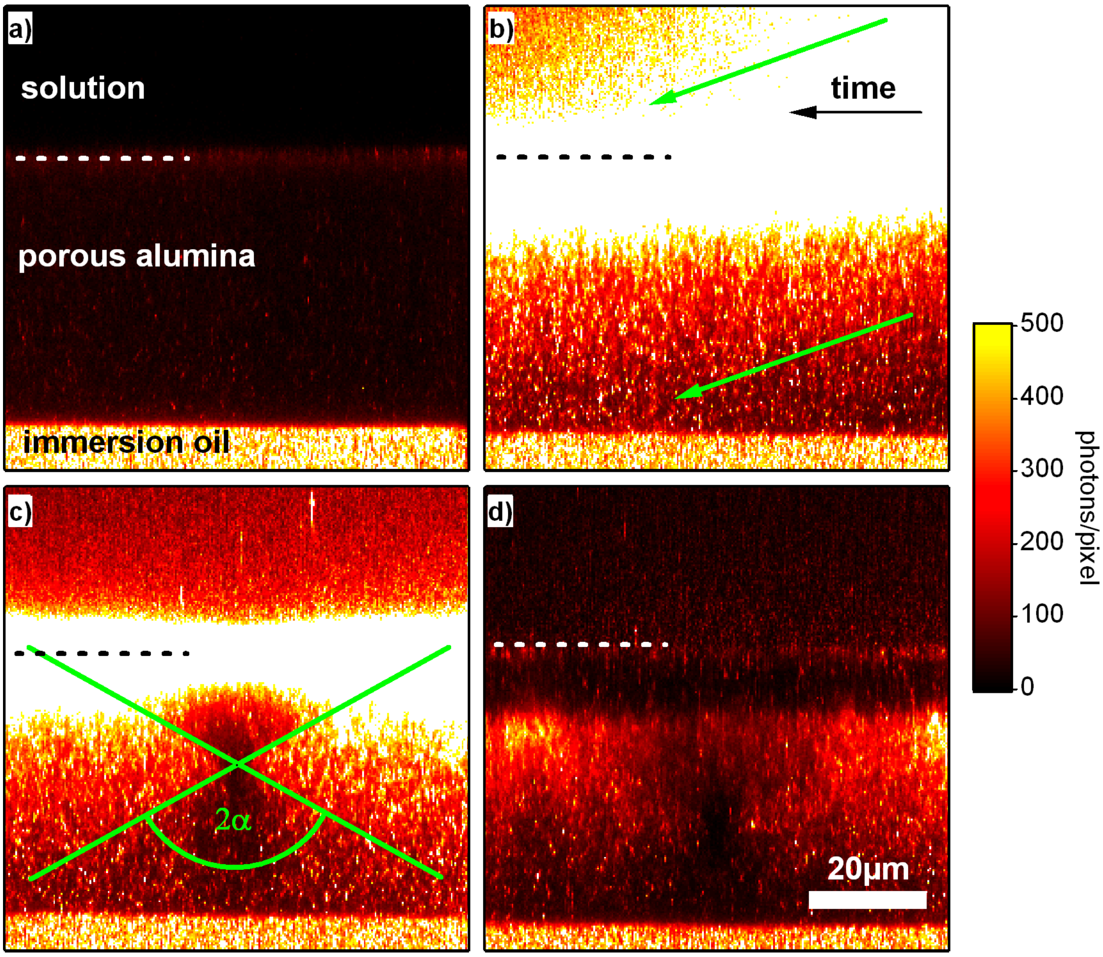

Figure 4.11: Color-coded scanning images of a water-filled porous alumina membrane. The membrane was attached via immersion oil to the cover glass using an oil-immersion objective for excitation and detection. The size of the image is 80 µm x 80 µm scanned with a resolution of 256 x 256 pixels. The dashed lines represent the water/membrane interface. **a)** Background intensity of the water filled membrane. **b)** After adding a few microliters of Barstar 488/594 solution to reach a concentration of 9 nM in the solution, strong adsorption of the fluorescent protein takes place at the water/membrane interface. Only a small fraction of molecules penetrate the membrane. The black arrow indicates the consecutive scanning time. **c)** Image taken after recording a longer time trace in the center of the crossed lines. The angle between the crossed lines is $2\cdot\alpha = 123°$. **d)** Image taking several minutes after adding 5 µl of 1M KOH to increase the pH-value from 7 to about 11.

ered by the color scale: a mean intensity of more than 5000 photons per pixel was measured directly at the interface. Figure 4.11 **c)** was recorded after taking a transient time trace for several minutes, where the focus was stationary placed at the center of the crossed lines. Strong bleaching occurs around the beforehand fixed focus position. The bleached region indicates a large fraction of immobilized molecules within the pores. Generally speaking, recording a transient time trace at a fixed position creates an image of the bleached region as a function of the excitation intensity distribution. This image can be used to estimate the detection angle of the oil-immersion objective inside the porous alumina membrane. The detection angle (between the crossing lines in figure 4.11 **c)**) was roughly estimated according to $2\cdot\alpha \simeq 123°$, which is in good agreement with the theoretical value of $2\cdot\alpha_t = 126°$ within a medium with a refractive index of $n = 1.57$. Note that the oil-immersion objective has a detection angle of $2\cdot\alpha = 134°$ in a medium with a refractive index of $n = 1.52$. Still, the detection angle of $2\cdot\alpha \simeq 123°$ is

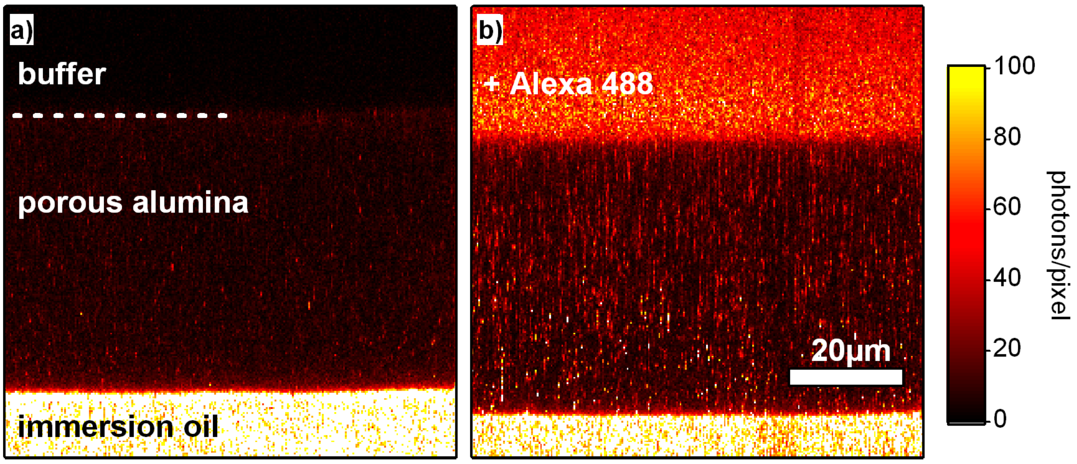

Figure 4.12: Color-coded scanning images of a citrate buffer filled porous alumina membrane. The membrane was attached via immersion oil to the cover glass using an oil-immersion objective for excitation and detection. The size of the image is 80 µm x 80 µm scanned with a resolution of 256 x 256 pixels. The dashed lines represent the buffer/membrane interface. **a)** Background intensity of the water filled membrane. **b)** After adding some micro liter of 130 nM Alexa Fluor 488 to reach a concentration of 6.5 nM in the solution, no adsorbtion of the fluorescent protein at the water/membrane interface takes place. Moreover, this image was taken after recording a transient time trace within the membrane. No bleaching of molecules is visible.

a significant improvement compared to the detection angle of $2 \cdot \alpha \simeq 100°$ within porous alumina using a water-immersion objective. The next image in figure 4.11 **d)** is recorded several minutes after adding 5 µl of 1 M KOH. Note that in this experiment deionized water was used instead of a buffer, therefore the *pH*-value increases instantaneously. This might lead to several (partly overlapping) effects, namely a degeneration of the alumina membrane (and thereby consequently the release of immobilized molecules), quenching of the fluorophores due to the release of oxygen and a change in the electrostatical behavior of the pore walls.

In conclusion, this example shows that the imaging of fluorescence along the porous membrane can provide useful information even if the recording of transient time traces within the membrane does not show any meaningful auto-correlation function.

The experiment discussed in the following deals again with the diffusion of Alexa Fluor 488 within porous alumina. Figure 4.12 shows a membrane attached with immersion oil to a cover glass. Note that the pores are closed at the bottom of the membrane. The immersion oil cannot penetrate the membrane. The laser power was adjusted to 25 µW at an excitation wavelength of 470 nm. The repetition rate of the laser was set to 40 MHz. The size of the image is 80 µm x 80 µm scanned with a resolution of 256 x 256 pixels at a scanning speed of 1 ms/pixel. A polarizing beamsplitter was used to separate the detected fluorescence into two detectors. Again, the background luminescence of the membrane as shown in figure 4.12 **a)** is almost negligible. After adding Alexa Fluor 488 to the citrate buffer solution (*pH* 8), the dye penetrates the membrane instantaneously without adsorbing at the solution/membrane interface. Figure 4.12 **b)** is taken after recording a transient time trace within the membrane showing no bleaching as expected due to the lack of immobilized molecules.

The transient time traces were recorded as a function of 1) the focus position at the *z*-axes within either the membrane or the solution and 2) as a function of the excitation polarization, which allows for accurate anisotropy measurements (not shown here). The oil/membrane interface corresponds to the focus position of 0 µm, whereas at a position of 45 µm the membrane/solution interface is located. Due to small shifts of the membrane in the z-direction during the measurements, the results from the different excitation polarizations at a position of 45 µm can not be compared with each other; for an excitation polarization of 0° the focus was predominantly located in solution, for an excitation polarization of 90° the focus was predominantly within the membrane.

The transient time traces were used to calculate the cross-correlation functions (not shown). Fitting these functions allows calculating the parameters shown in figure 4.13. Figure 4.13 **a)** shows the diffusion time τ_D as a function of the focus position. Interestingly, the expected diffusion time of around 1 ms (as determined by using a water-immersion objective in sections 4.1) within the membrane can only be found at a depth of about 35 µm. If the position of the focus is changed to smaller values, the diffusion time decreases to $\tau_D \simeq 0.35$ ms. As it is obvious from the MC-simulations in section 4.4, this finding can not be explained by a change in the auto-correlation function properties caused by the closed side of the pores. Moreover, a change in the diffusion coefficient would compromise previous results as discussed in section 4.1. Let us estimate the size of the focus, by taking the calculated diffusion time and the diffusion coefficient of Alexa Fluor 488 $D = 2.8 \cdot 10^{-6}\text{cm}^2/\text{s}$. According to $z_0 = \sqrt{4D\tau_D}$ the long half axis equals $z_0 \simeq 630$ nm. This shrinking of the excitation/detection focus is supported by figure 4.13 **b+c)**. Near the proximity of the side of the membrane with the closed pore bottoms, firstly, the mean particle number within the focus (which is in fact a function of the size of the focus) reaches a local minimum, whereas, secondly, the brightness reaches its maximum within the membrane. As shown in figure 4.13 **d)**, both findings occur with a constant count rate within the membrane. This indicates that in contrast to the mean number of fluorescent molecules within the focus, the overall concentration of molecules within the pore remains constant.

Moreover, the dimension of the focus was determined for an oil-immersion objective in reference [46]. The long axes equals $z_{0,oil} \simeq 610$ nm, which is in reasonable agreement with the calculated length of $z_0 \simeq 630$ nm by using $\tau_D \simeq 0.35$ ms. The increase of the diffusion time towards larger distances to the oil/alumina interface can again be attributed to the mismatch of the effective refractive index of water-filled porous alumina ($n_{alox} = 1.57$) to the refractive index to that the oil-immersion obejctive is corrected for ($n_{oil} = 1.52$). Due to this mismatch, spherical aberrations occur, which enlarge the dimensions of the focus in z-direction reaching approximately $z_0 = 1$ µm at a distance of 35 µm from the oil/alumina interface. Nevertheless, it has to be mentioned that according to equation 2.33 the particle number and the brightness within the membrane are strongly influenced by the background luminescence. In addition, measurements in solution ($n_{H_2O} = 1.33$) are neither corrected for the distortion of the focus which occurs after travelling through the whole membrane nor for measuring of solution with an oil-immersion objective. Therefore, the calculated values in the aqeous phase should be taken with care.

In conclusion, the oil-immersion objective has the great advantage that especially close to the oil/alumina interface, the focus is only slightly distorted and the detection angle is close to the

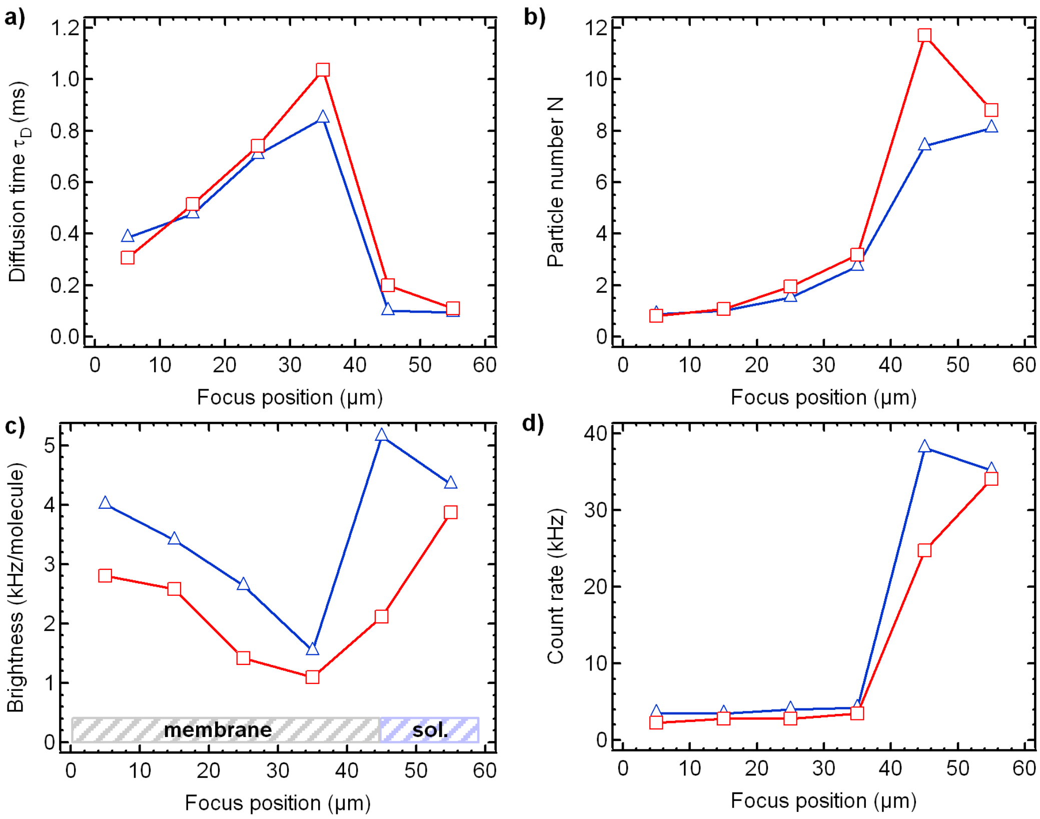

Figure 4.13: Alexa Fluor 488 diffusing within porous alumina (closed bottom) and in solution using an oil immersion objective. The measurements were performed using two excitation polarizations: 0° for the blue markers (-△-) and 90° for the red markers (-□-). All graphs are plotted as a function of the focus position, whereas the oil/membrane interface was set to zero: **a)** diffusion time τ_D, **b)** mean particle number N, **c)** molecular brightness B, and **d)** count rate.

maximum given by the numerical aperture of the objective. As shown in figure 4.13 **c)**, the molecular brightness is at this point almost as high as in free solution. From a more practical point of view, the usage of immersion oil to couple the membrane to the cover slide is very effective in terms of stability and reproducibiltiy.

Comparison of the objective configurations

As outlined in section 3.2, three different configurations were used for probing the diffusion in porous alumina. In each case, the membrane was glued onto a small glass tube. Whereas in the first two configurations the glass tube was pushed to the cover slide and the space between the membrane and the cover slide was either filled by water or immersion oil, the third configuration uses a linear actuator to position the glass tube in a larger, solution-filled chamber. The last configuration, which was mainly used in section 4.1, does not allow for scanning along the pores as the first two configurations do. However, using the third configuration enables the straightforward comparison of measurements in solution with measurements within the membrane because the measurement can be performed in the space between the coverglass and the membrane thus avoiding optical aberrations due to the membrane.

The drawback of this configuration is that, beside the impossibilty of accurate scanning, using a water-immersion objective for excitation and detection reduces the detection angle within the membrane significantly. As discussed in section 4.1, almost half of the emitted intensity is lost for detection. The same problem occurs for the configuration with the pushed glass tube using the water-immersion objective, even if scanning along the pores is now possible.

The oil-immersion objective matches the refractive index of the water-filled alumina membrane quite well, even if the focus size along the optical axis is reduced in comparison to the water-immersion objective. It should be mentioned that by further tuning the porosity of the membrane, the effective refractive index of the membrane can be adjusted to the refractive index of glass. This would be the best choice for experiments where the knowledge about the size of the focus is mandatory.

4.3 1D-diffusion of eGFP: Changing *pH*-value

As discussed in section 4.1, the porous alumina membranes were incubated in bovine serum albumine (BSA) in order to prevent unspecific adsorption of the probes at the pore walls. However, it was shown that there is still a significant fraction of immobilized eGFP present within the membrane. This section deals with the diffusive behavior of eGFP within the membranes as a function of different *pH*-values without incubating the membranes in BSA beforehand. Therefore, the following set-up settings were used: the laser power of the diode laser operating at 488 nm was adjusted to 60 µW. The excitation was performed using linear polarized laser light. Behind the dichroic mirror, the remaining laser light was filtered using a 532 ± 35 nm bandpass filter. A 50/50 beam splitter was used to seperate the emitted light into two detectors for cross-correlation analysis. The membrane was fixed using the scheme shown in figure 3.2 **b)**. Excitation and detection was performed using the water-immersion objective. The drastic effect of changing the *pH*-value of the buffer solution is demonstrated in figure 4.14. Figure 4.14 **a)** shows the background intensity of the membrane, of the citrate buffer solution (10 mM citric acid and 100 mM potassium phosphate) and pure water for optical coupling of the membrane to the microscope cover slide. Figure 4.14 **b)** was recorded directly after addition of eGFP in order to obtain a concentration of 9.2 nM in solution. The green arrow indicates the consecutive scanning times. The penetration of the protein into the membrane starts slowly and can be tracked by the scanning image. After recording of 4.14 **b)**, the focus of the microscope was placed within the membrane, indicated by the green ellipse in figure 4.14 **c)**, and a stationary intensity time trace was recorded. Figure 4.14 **c)** shows the image recorded after finishing the transient time trace. No adsorbtion at the membrane/buffer interface and no bleaching in the region of the recorded time trace is visible. This indicates that a large fraction of the proteins is mobile. A different behavior can be found, if instead of *pH* 8 for the initial buffer a *pH*-value of 6 was used. Figure 4.14 **d)** was recorded after the addition of eGFP to the buffer, and after recording an intensity time trace at the position marked by the green ellipse. The first distinctive feature is the strong adsorption at the membrane/solution interface. Whereas the legend of the figure has a color range from zero to 120 photons/pixel, the count rate exceeded 5000 photons per pixel at the interface. Moreover, strong bleaching occured, which is an additional hint for a large fraction of immobilized molecules. According to the literature, the isoelectric point (IEP) of alumina is around $pH\sim 8-9$ [27, 108] and for (e)GFP around $pH\sim 5.5$ *[70]*. It was reported by Lau and coworkers that BSA shows the strongest adsorption behavior within alumina membrane at its IEP of *pH*∼ 5 [57], regardless of the charge state of the adsorption surface [27]. Therefore, both the strong adsorption of eGFP at a *pH*-value of 6 and the lower adsorption behavior at higher *pH*-values can be explained, by assuming that both proteins with almost equal IEPs (eGFP and BSA) show a comparable adsorption behavior. Moreover, by testing different *pH*-values it was found that only at *pH*-values between *pH* 8 nad *pH* 11 bursts in the corresponding stationary intensity time traces were detectable within the membrane, whereas for lower *pH*-values the strong adsorption starting at the membrane/solution interface inhibited the detection of a diffusing fraction.

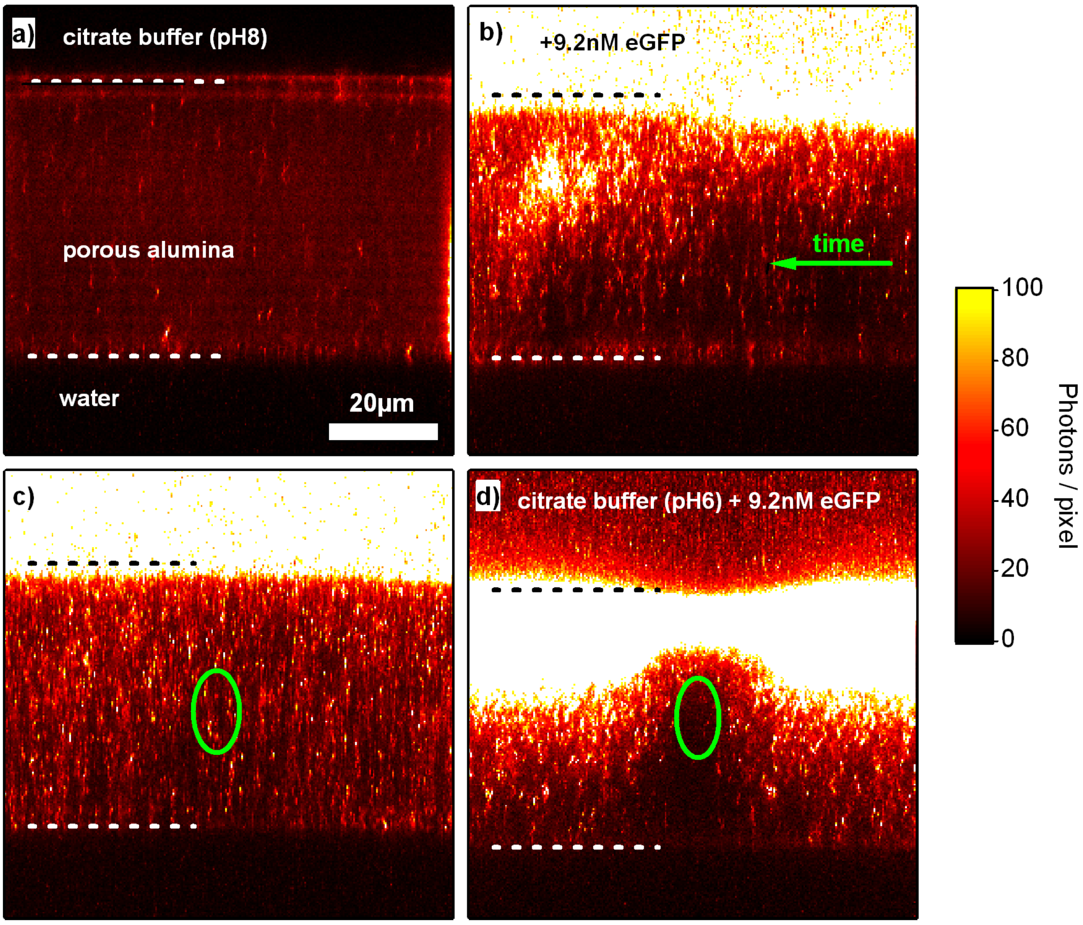

Figure 4.14: Color-coded scanning image of a buffer-filled porous alumina membrane. The membrane was attached via pure water to the cover glass using an water-immersion objective for excitation and detection. The size of the image is 60 µm x 60 µm scanned with a resolution of 256 x 256 pixels, recorded with a speed of 1 pixel/ms. The dashed lines represent the buffer/membrane and the pure water/membrane interface. **a)** Background intensity of a buffer-filled (*pH* 8) porous alumina membrane. **b)** Image recorded after adding several µl of eGFP in order to reach a concentration of 9.2 nM in solution. The green arrow indicates the direction, in which the focal volume was shifted during the series of consecutive measurements. The penetration of the dye into the membrane starts slowly. No adsorption is visible at the solution/membrane interface. **c)** Image recorded after taking a intensity time trace for several minutes at the position of the green ellipse: no bleaching visible. **d)** Instead of using a buffer with a *pH*-value of 8, a *pH*-value of 6 was used. The image was taken after recording an intensity time trace at the position of the green ellipse: strong bleaching is visible. In addition, a strong adsorption occurred at the solution/membrane interface where the count rate exceeded 5000 photons per pixel.

4.4 Monte-Carlo simulations of 1D and 3D diffusion

1D diffusion in single nanopores

As it has been shown in section 4.1, confined diffusion of single fluorescent molecules in nanoporous alumina can be explained with the model of quasi one-dimensional diffusion. Nevertheless, the complexity of the investigated system is still high. The auto-correlation curves, which fully represent the diffusional properties of the molecules in the system can be influenced by several effects: 1) the porous structure itself can contribute a background intensity signal, which leads to an increased apparent number of particles in the detection focus, 2) particles can interact with the porous structure. For example, particles can adsorb at the pore walls, which may lead to an uncorrelated background intensity, 3) the excitation/detection focus can be changed within the membranes due to the different refractive indices of the water filled porous structure and the used microscope objective, and 4) the auto-correlation fitting functions were derived for the case of infinite diffusional space. This is not fulfilled for the diffusion within a finite pore.

The simulations in the following section do not aim in covering the whole complexity of quasi one-dimensional diffusion in nanopores. In fact, the idea is to start with a simple model system. For the simplest case, the diffusion of single molecules was simulated in a single pore using a fully Gaussian excitation/detection focus. The diffusion coefficient was set to $D = 2.8 \cdot 10^{-6}\mathrm{cm}^2/\mathrm{s}$, which equals the diffusion coefficient of Alexa Fluor 488. The pore diameter was set to 30 nm and the size of the focus, which was placed in the center of mass of the pore, was defined by $w_0 = 250\,\mathrm{nm}$ and $z_0 = 1000\,\mathrm{nm}$ in agreement with the experiment. The excitation probability for a molecule in the center of the focus was set to $\rho = 0.2/\mu\mathrm{s}$. Figure 4.15 **a)** shows the normalized auto-correlation functions as a function of the pore length, which ranged from 5 µm to 60 µm (in steps of 5 µm), for the first boundary condition and **b)** for the second boundary condition. For the description of the boundary conditions see section 3.4. In the simulations using the first boundary condition, where movements which would cause the molecule to leave the pore are discarded, the shape of the auto-correlation changed dramatically for small pore lengths of less than 30 µm. Even for a pore length of 60 µm, the one-dimensional model (represented by the solid black line) according to equation 2.19 does not fit properly for times around 0.1 s. As it has been discussed above, the fitting functions were derived for the case that the molecules have an infinite space for diffusion. In conclusion, even if the pore length is much larger than the elongation of the focus in the z- direction, the calculated auto-correlation function is sensitive to the first boundary condition. The simulations, which are using the second boundary condition, show a completely different behavior. Here, each molecule which would leave the pore at the top side is virtually destroyed. However, at each time step there is a certain probability that a new molecule enters the pore. Only the auto-correlation function of the smallest pore featuring a length of 5 µm differs clearly from the other auto-correlation functions. For the case of pore lengths larger than 30 µm the fitting function matches almost perfectly the one-dimensional model.

Figure 4.16 **a)** shows the diffusion time τ_D as a function of the pore length for all boundary conditions as introduced in section 3.4. The dashed line represents the expected diffusion time which is calculated according to $\tau_{0,D} = z_0^2/4D = 0.89\,\mathrm{ms}$. Whereas τ_D is almost constant for

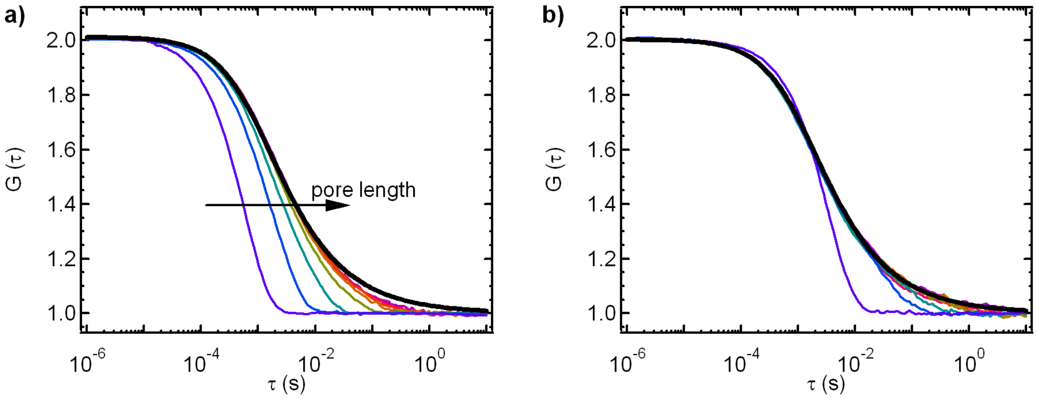

Figure 4.15: Simulated normalized auto-correlation functions of molecules diffusing in single pores with different pore lengths. The pore lengths range from 5 µm to 60 µm. The simulations in **a)** are using the first boundary condition: movements, which would cause the molecules to leave the pore are discarded, the simulations in **b)** are using the second boundary condition: molecules, which leave the pore at the top are destroyed. Nevertheless, new molecules can enter the pore with a certain probability. The black lines show the corresponding fits for pores with a length of 60 µm.

the second boundary condition above a pore length of 5 µm, the first and the third boundary condition leads to a different behavior. Here, τ_D increases without reaching the expected value even for a pore length of 60 µm. This finding can be explained by the fact that the boundary conditions that prevent the molecules from vanishing, impose some periodicity to the diffusional system. Each molecule will re-enter the focus within a certain timeframe if it is reflected by the lids of the cylinder (pore). This periodicity is broken if the molecules can diffuse away from the pore, as it is possible only in the case of the second boundary condition.

The question remains why the calculated τ_D value using the second boundary condition is larger than the expected value $\tau_{0,D} = 0.89\,\text{ms}$ in most cases. To answer this question, we have to consider the other graphs in figure 4.16. Figure 4.16 **b)** shows the mean particle number N as a function of the pore length. Except for a pore length of 2.5 µm, the initial concentration for each pore length was one particle per 5 µm pore length. The smallest pore initially contained one particle, and thereby twice as much particles per length. However, even under this assumption the calculated mean particle number is too high for the first and the third boundary condition which can be explained by the fact that the pore length is even smaller than the long axis of the detection focus. If the pore length is 10 µm or larger, N remains constant.

Simulations using the second boundary condition show a different behavior. Here, N is smaller as compared with the other boundary conditions and is increasing with increasing pore length. This effect is caused by the possibility of changing the concentration within the pore when molecules either can leave the pore or enter the pore. If the rate at which molecules leave the pore is initially larger than the rate at which particles enter the pore, the mean particle number decreases until a new equilibrium is reached. The auto-correlation function is averaging the mean particle number over the whole duration of the simulation. Thus, the decrease in the particle concentration in a small pore is faster than in a large pore and leads to smaller mean particle numbers as seen in the graph. This decrease in concentration does additionally affect the auto-correlation function, which normally decays to unity for infinite times, in such a way that an offset in $G(\tau)$ is induced. The (small) offset cannot be fitted using the normal one-

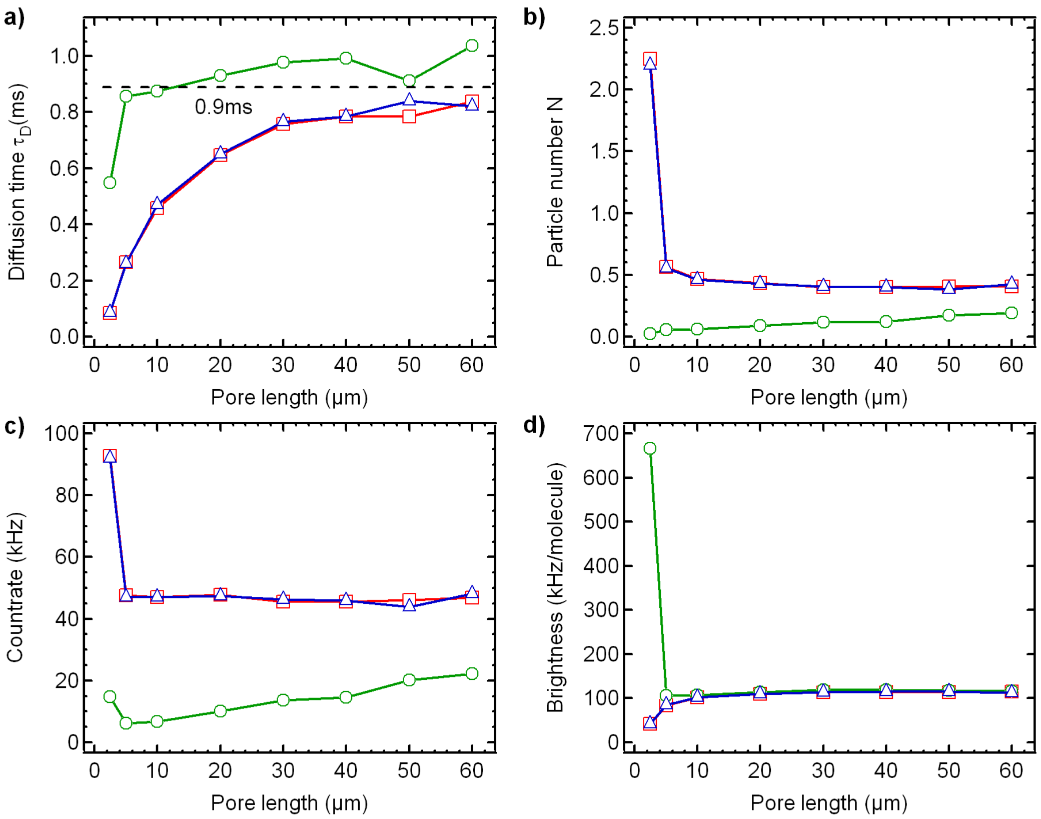

Figure 4.16: Various simulated parameters describing the diffusion properties as functions of the applied boundary condition and the length of the pore. Three different boundary conditions have been used: (-□-) as the first, (-◯-) as the second and (-△-) as the third boundary condition as discussed in section 3.4. The diffusion time τ_D as a function of the pore length is shown in **a)** Here, the expected diffusion time $\tau_D = 0.9$ ms is represented by the dashed line. The brightness B as shown in **b)** is calculated from the mean count rate shown in **d)** divided by the mean particle number N as shown in **c)**.

dimensional fitting function and will lead to a change in the determined diffusion time τ_D as it can be seen for the diffusion time calculated from the simulations with the second boundary condition. Figure 4.16 **c)** shows the mean count rate as a function of the pore length. For the first and third boundary condition, the count rate reproduces perfectly the molecule concentrations, which are constant with the exception of the doubled molecule concentration in the smallest pore. The second boundary condition shows an interesting feature for the smallest pore, where the count rate is higher than for the longer pores. Again, this can be explained by the given probability that a new molecule can enter the pore. In most cases, this molecule will disappear very soon. However, molecule is generated close to the focus, there will be a certain probability that the molecule is excited and emits photons without significantly contributing to the auto-correlation function. The evaluation of the brightness in figure 4.16 **d)** supports this finding: if the calculated mean number of molecules is small but the count rate is high, the molecule shows a very high apparent brightness. If the pores are larger than 5 µm, the brightness $B \simeq 100$ kHz is equal for each of the boundary conditions.

Another problem to be addressed is whether the position of the excitation/detection focus with respect to the pore does play a role for the obtained auto-correlation function. Figure 4.17 **a+b)** shows the diffusion time τ_D and the mean particle number N as a function of the position of

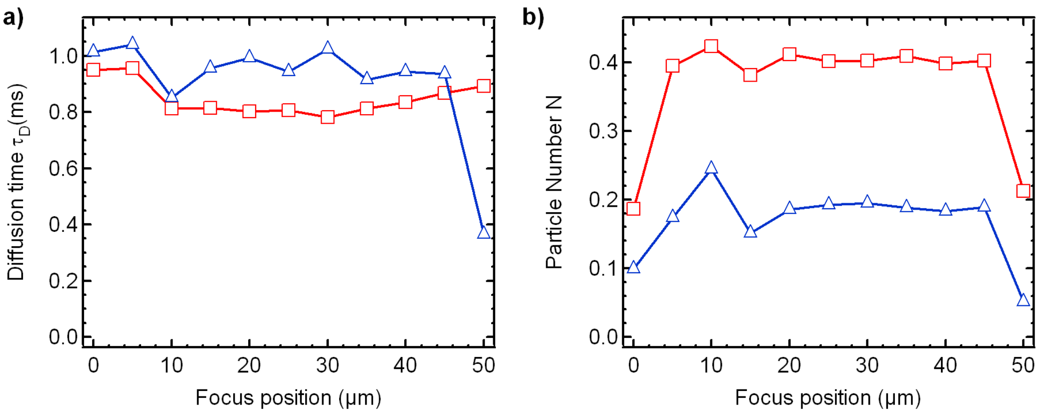

Figure 4.17: a+b) Simulated diffusion time τ_D and mean particle number N as a function of the position of the focus in a single pore with a length of 50 µm. Two boundary conditions were used: (-□-) as the first and (-△-) as the second boundary condition, as discussed in section 3.4.

the focus within a single pore with a length of 50 µm. The focus position of 0 µm corresponds in all cases to the closed side of the pore, where possible movements out of the pore are discarded according to the first boundary condition. Due to impedement of motion out of the pore, the mean diffusion time is slightly extended at this point. It has to be mentioned that half of the focus is out of the region of interest, which has almost no influence on the diffusion time, however, the mean particle number drops by a factor of two. The decay of the auto-correlation curve is only given by fluctuations in the intensity and not by the (mean) intensity itself. Nevertheless, the auto-correlation function is normalized by the squared (mean) intensity. For this reason, it is obvious that in the case of the diffusion time the pore bottom acts like a mirror of the fluctuations, whereas for a constant concentration of molecules within the pore the count rate is expected to decrease by a factor of two, thus perfectly matching the decrease of the mean particle number N.

At the focus position of 50 µm an additional effect occurs for the case of the second boundary condition. The diffusion time is drastically smaller because the molecule can disappear through the opening of the pore. Even if there is a certain probability that a new molecule enters the pore at the top, in most cases the new molecule will rapidly diffuse away.

In conclusion, the simulations confirm the quasi-one dimensional diffusion model quite well as long as the pore length is larger than 30 µm and the pore diameter is small in comparison with the dimensions of the focus in the x- and y-plane. Additionally, it was found that the boundary conditions play an important role in the interpretation of the obtained results.

1D diffusion in pore arrays and 3D diffusion

We will now extend the simulations by taking into account that in the experiment more than one pore is located within the focus. As discussed in section 4.4, this can be realized by creating a virtual hexagonally ordered pore array. Every molecule is randomly placed in one of the 60 pores. The generated hexagonal pore array consists of a central pore and the pores within an area with a radius corresponding to the eight-nearest neighbor distance. If the lattice constant is set to 65 nm, this distance is 260 nm, which corresponds to the small half axes $w_0 = 250$ nm of the excitation/detection focus. Larger pore arrays can be taken into account, nevertheless,

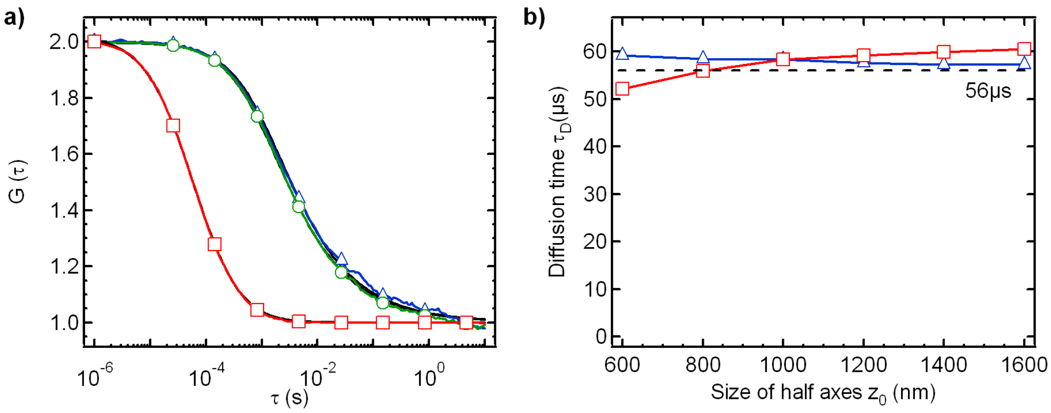

Figure 4.18: **a)** Comparison of the simulated normalized auto-correlation functions between three-dimensional diffusion (-□-), in this graph, the symbols represent every 20th data point), one dimensional diffusion in a single pore (-○-) and one dimensional diffusion in an array of pores (-△-). For the simulations of one-dimensional diffusion the second boundary condition was used. The solid black lines (almost invisible behind the calculated auto-correlation lines) show the corresponding fits. **b)** Influence of the focus size in the z- direction (represented by z_0) by using a fixed w_0 on the diffusion time for the case of three-dimensional diffusion. The ratio of z_0/w_0 represents the structure factor s of the focus. If the structure factor is set to $s = 4$ for all auto-correlation functions, the boxed values (-□-) are calculated. If the structure factor is set to z_0/w_0 according to the initial parameters for the simulations, the triangled values (-△-) are calculated. Here, the expected diffusion time of $\tau_D = 56\,\mu\text{s}$ is shown by the dashed line.

the computation time increases rapidly if the concentration of molecules within the pores is kept constant and thereby the number of simulated molecules has to be increased. Figure 4.18 **a)** shows the calculated auto-correlation function for the simulation of the three-dimensional diffusion, the quasi one-dimensional diffusion in a single pore and the quasi one-dimensional diffusion in an array of pores. The auto-correlation function of three-dimensional diffusion decays much faster than for the one-dimensional case, because a molecule can diffuse out of the focus volume in any direction. Moreover, the auto-correlation functions of the two cases of one-dimensional diffusion almost coincide. Only at timescales in the millisecond range slight deviations occur, which can be attributed to the different brightness of both variants. For the case of diffusion along the single pore, where the origin of the excitation/detection focus is in the center of mass of the pore, the expected photon count rate is higher than for a molecule diffusing in a pore, which is almost at the edge of the focus. Keeping in mind that the shape of focus is similar to a rotational ellipsoid, the brightness calculated for one-dimensional diffusion in a pore array is about 50% of the brightness in a single pore ($B_{1\text{D}}^{\text{Array}} = 65\,\text{kHz/molecule}$, $B_{1\text{D}}^{\text{sPore}} = 121\,\text{kHz/molecule}$). The brightness for the three-dimensional case $B_{3\text{D}} = 59\,\text{kHz/molecule}$ is even slightly lower, because the number of pores in the pore array is still too small to recover all contributions of the whole focus.

I will now concentrate on the diffusion time for the case of three-dimensional diffusion. As shown in figure 4.18 **a)**, the corresponding fitting function for the auto-correlation function matches perfectly the simulations. For simulating the three-dimensional diffusion inside a cylinder, the height of the cylinder was set to 5 µm and the diameter was set to 3 µm. Figure 4.18 **b)** shows the diffusion time as a function of z_0, which is the size where the maximum intensity of the Gaussian focus drops to $1/e^2$ along the z-axis. Changing z_0 by fixing $w_0 = 250\,\text{nm}$ will change the structure factor $s = z_0/w_0$. If the fitting functions for the two-dimensional case of diffusion (equation 2.20) are compared with the three-dimensional one, (equation 2.21), they only differ in a single term. If $z_0^2 \gg w_0^2$, this additional term contributes only slightly to the fitting procedure. For this reason, the diffusion time τ_D is almost insensitive to the size of the half axes z_0. Even if the fitting is performed with a fixed structural parameter of $s = 4$ for all cases, the deviation from the expected theoretical value of $\tau_D = w_0^2/4D = 56\,\mu\text{s}$ as represented by the dashed line is negligible. In conclusion, whereas for the case of three-dimensional diffusion the diffusion time is mainly sensitive to the size of the focus in the x-, y-plane, in the case of one-dimensional diffusion along the pores the diffusion time $\tau_D = z_0^2/4D$ is highly sensitive to z_0 .

Monte-Carlo simulations of spFRET in solution

This subsection deals with the simulation of doubly labeled proteins diffusing either in solution or in an array of pores. These doubly labeled proteins can untergo conformational changes. Thus, the distance between the attached dyes (labels) changes, which results in different energy transfer rates from the donor to the acceptor dye. Calculating this energy transfer efficiency has been a major challenge in recent years [104, 89, 72]. Two different approaches can be used to determine the transfer efficiency E by using the detected transient time traces. For the first one, each bin is used for calculating E according to equation 2.12, as long as the sum of both intensites per bin is above a certain threshold. Normally, a binwidth of $500\,\mu\text{s}$ is used for binning the transient time traces. This value has to ensure that, on the one hand, a molecule diffusing through the focus emits enough photons in this time to be statistically relevant and, on the other hand, that the counting of background intensity is minimized. Additionally, it has to be ensured that no averaging over different molecules takes place. The second approach of determing the transfer efficiency is slightly different. Here, a burst is defined and integrated intensities within each burst are used to calculate E [72, 17]. For the sake of simplicity, the proposed burst-search algorithm was modified in the following way, still making use of the binned transient time traces. Photons belong to a burst if at least $L = 50$ phontons are detected in a number of consecutive bins with at least $M = 30$ photons per bin. Figure 4.19 **a+b)** shows snapshots of the transient time traces of the donor and the acceptor channel for doubly labeled proteins diffusing in bulk solution (**a**) and within an array of pores (**b**), respectively. In addition, the burst-search algorithm was applied to the sum of both time traces of each graph. This algorithm gives ”1” if the bin corresponds to a burst otherwise ”0”. As seen in figure 4.19 **a+b)** the transients differ in their shape with respect to the dimensionality of diffusion. Whereas in 4.19 **a)** the width of the burst is given by one bin only, the width of the bursts in 4.19 **b)** is mostly larger. To give a more qualitative picture, the number of bursts as a function of the number of bins per burst is plotted in 4.19 **c)**. Comparing the three-dimensional case of diffusion with the one-dimensional case, two distinctive features should be noted. First, the overall number of bursts and second, the average number of bins per burst is much smaller in the case of the three-dimensional diffusion. This results in an increased number of photons per bin as compared to the one-dimensional diffusion as seen in figure 4.19 **d)**. The simulated time was equal for both cases of diffusion. In addition, a certain probability of $\rho_{T,D} = 0.1$ for

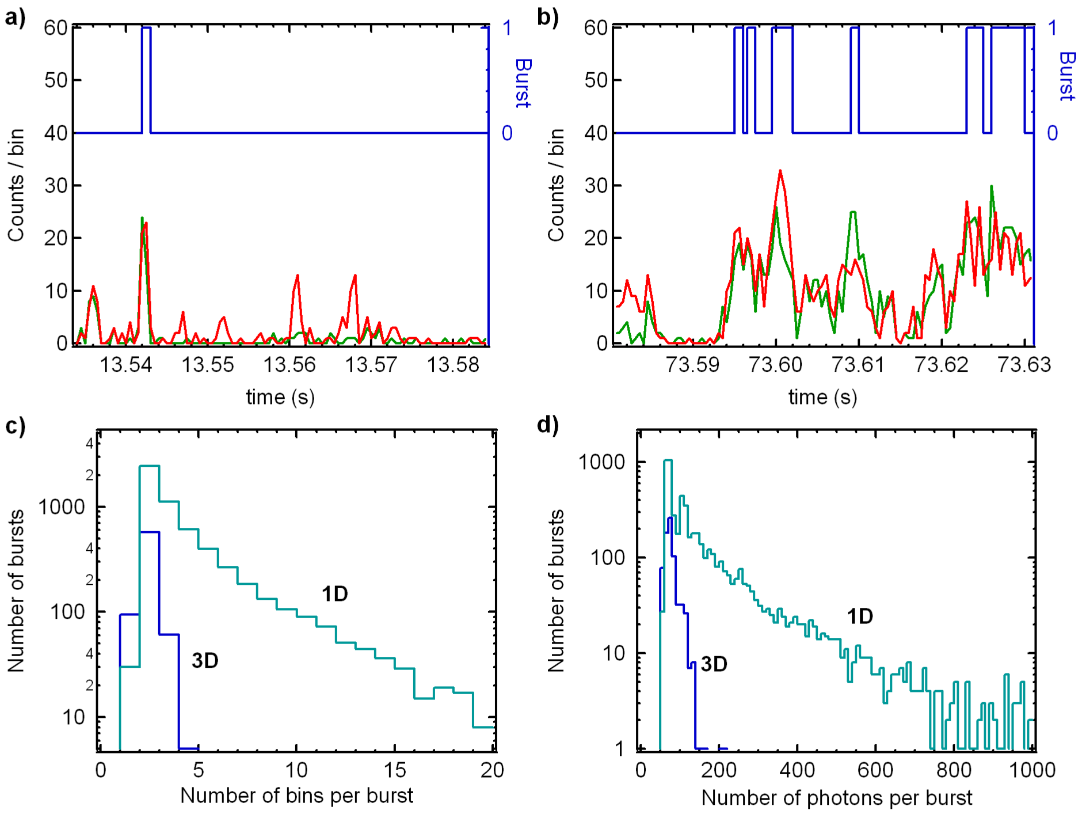

Figure 4.19: Simulation of doubly labeled proteins diffusing either in free solution or in an array of pores. **a+b)** Transient time traces of the protein: the green line represents the detected intensity in the donor channel and the red line in the acceptor channel, respectively. Both intensities are summed up for each bin, and a burst-criterion (see text for details) is applied. The burst trace (blue line) is either ”1” if a bin belongs to a burst otherwise ”0”. **a)** Simulations of diffusion in free solution and **b)** in an array of pores. **c)** Number of bursts as a function of the number of bins per burst. **d)** Number of bursts as a function of the number of photons per burst.

the donor and $\rho_{T,A} = 0.2$ for the acceptor was included for relaxation of excited states to non-fluorescent triplet states with a time constant of $\tau_T = 10\,\mu\text{s}$. In order to check the mean particle number N within the excitation/detection focus, the auto-correlation functions were calculated for both time traces detected in the donor channel. Figure 4.20 shows the auto-correlation function for the cases of quasi one-dimensional and three-dimensional diffusion. Again, the diffusion time is increased in the case of quasi one-dimensional diffusion. This increased diffusion time is highly advantageous for the separation of different compartments of the auto-correlation function. Whereas in the one-dimensional case the two contributions to intensity fluctuations, namely diffusion and triplet dynamic, can be clearly separated, the excistence of two components instead of one in the case of three-dimensional diffusion is easily overlooked. Here, the confined diffusion is a suitable tool to study dynamics of single molecules on time scales which are normally dominated by diffusion.

The mean particle numbers calculated by using appropriate fitting-functions are almost equal. As discussed above, the quasi one-dimensional diffusion shows a pronounced burst-like behaviour. The question arises whether this feature is useful for the determination of energy transfer efficiencies. In addition to the different cases of diffusion, the two possibilities of calculating the transfer efficiencies, namely the bin- and the burst-approach, are elaborated in

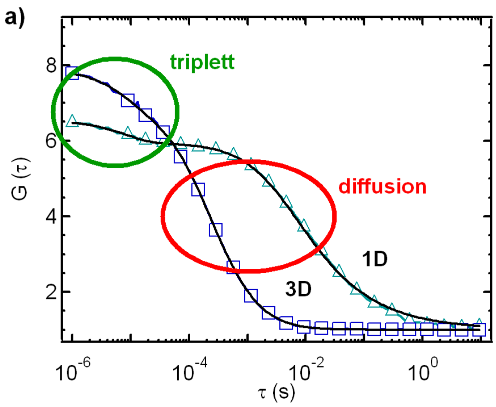

Figure 4.20: Simulated auto-correlation functions of the donor channel showing the differences in diffusion time for three-dimensional diffusion (-□-, symbols represent every 10th data point) and quasi one-dimensional diffusion (-△-), respectively. Here, a triplet-fraction was included in the simulations. This fraction is only clearly separable from the time-domain of diffusion in the case of 1D-diffusion. The solid black lines show the corresponding fits.

detail. The simulations were performed using equal time-constants for the folded $\rightleftharpoons$ unfolded

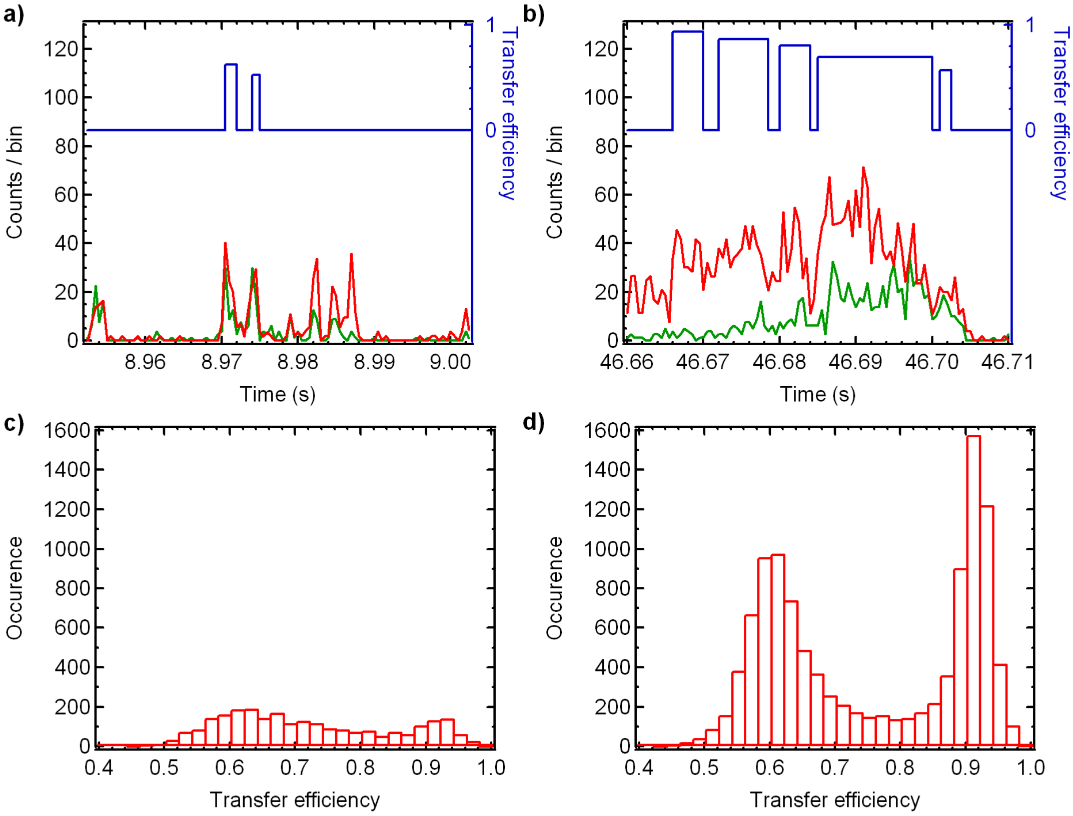

Figure 4.21: Simulation of doubly labeled proteins diffusing either in free solution or in an array of pores. **a+b)** Quantum yield-corrected transient time traces of the protein: the green line represents the detected intensity in the donor channel and the red line in the acceptor channel, respectively. Both intensities are summed up for each bin, and a burst-criterion (see text for details) is applied. The transfer efficiency was calculated according to equation 2.12 for each burst. **a)** Simulations of diffusion in free solution and **b)** in an array of pores. Histograms of the transfer efficiency **c)** in free solution and **d)** in an array of pores.

transitions. The quantum yield for the donor was set to $\Phi_{f,D} = 0.8$ and for the acceptor to $\Phi_{f,A} = 0.5$. These values are neccesary for calculating the transfer efficiency using equation 2.12. Ideally, both quantum yields are close to unity. Unfortunately, this condition is never fulfilled under experimental conditions. According to chapter 3.4, the detection efficiencies of both channels were set to one. Figure 4.21 **a+b)** shows the quantum yield corrected transient donor and acceptor time traces for 1D and 3D diffusion. In addition, the transfer efficiency is shown for each burst. Here, the burst-search criterion was slightly modified to match the conditions for the corrected time traces. The minimum number of photons per bin was reduced to $M = 20$, and the minimum number of photons per burst was increased to $L = 100$. The histograms of the transfer efficiencies per burst are plotted in figure 4.21 **c+d)**. Both figures show two distributions corresponding to the folded and the unfolded states of the diffusing proteins. Nevertheless, the histograms for 1D diffusion contain a larger number of bursts, and even more important, the relative width of the distributions is smaller than in the 3D case of diffusion.
In conclusion, calculating the transfer efficiencies by applying the burst-search algorithm benefits massivly from the prolonged diffusion time in the case of one-dimensional diffusion. The key point is the increased number of detectable photons per burst, which decreases the relative width of the distributions. This is of considerable importance if a larger number of sub-populations is studied (for example with two doubly-labeled species), where the ability to distinguish these populations in the transfer efficiency histogram is mandatory.

4.5 FRET in porous alumina

This section presents first results of the detection of FRET in nanoporous alumina membranes. Barstar 488/594 was introduced in section 3.3 as a small protein, which was additionally labeled with a donor dye (Alexa Fluor 488) and an acceptor dye (Alexa Fluor 594) [45]. The set-up was modified in order to fulfill the requirements for the detection of the energy transfer. The excitation laser power of the 488 nm continuous-wave diode laser was set to 80 µW. A 570 nm dichroic beamsplitter was used to separate the light emitted from the donor and the acceptor into the corresponding green and red detector channel. Furthermore, the light was filtered using a 532±35 nm bandpass filter for the green channel and a 650±50 nm bandpass filter for the red channel. An oil-immersion objective was used for detection. The membrane was attached to the cover slide using a thin (10 µm) layer of immersion oil and the membrane was fixed with respect to the scanning device. The scanning along the membrane was performed by using a 80 x 80 µm scanning area, rastered with a local resolution of 256 x 256 pixels and a time resolution of 1 ms/pixel. Figure 4.22 **a+b)** shows the background intensity in the green and the red detection channel, respectively. Comparing the intensities in the green and the red detection channel reveals that the background intensity of the buffer is slightly lower and the background from the membrane is slightly higher in the red detection channel. The detection efficiency of the photodiodes increases at higher wavelengths. Nevertheless, the background intensity is relatively low, and can be further decreased by bleaching with the laser at a fixed position within the membrane. Figure 4.22 **c+d)** was recorded after addition of several µl of Barstar 488/594 solution in order to reach a concentration of 6.2 nM in solution. Figure 4.22 **c)** shows a strongly increased intensity in the buffer and the stripelike behavior of proteins

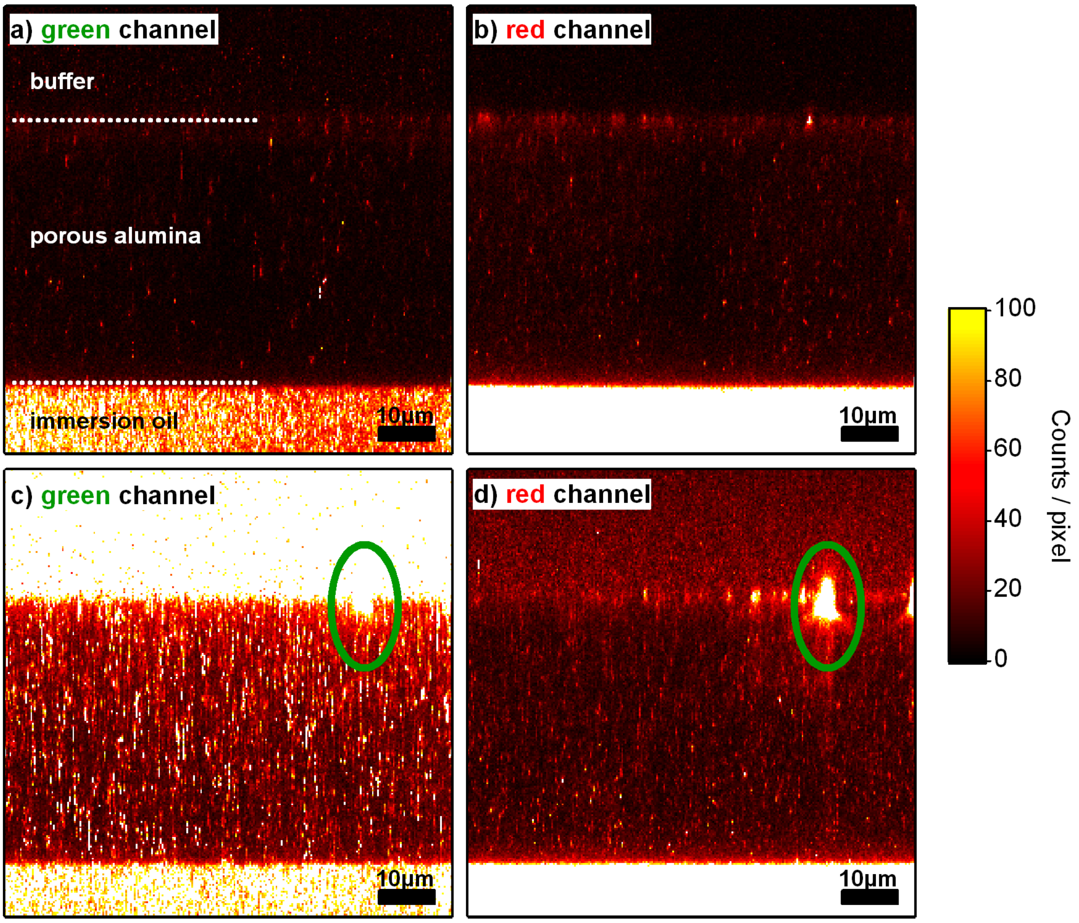

Figure 4.22: Color-coded scanning images of a citrate buffer-filled porous alumina membrane. The membrane was attached via immersion oil to the cover glass using an oil-immersion objective for excitation and detection. The size of the image is 80 µm x 80 µm scanned with a resolution of 256 x 256 pixels. The dashed lines represent the buffer/membrane and the membrane/oil interface. **a+b)** Background intensity of the buffer-filled membrane in the green channel and in the red channel. **c+d)** Scanned images of the green and the red channel after addition of 6.2 nM Barstar 488/594 solution. The green ellipse represents a defect in the membrane with strong adsorption of Barstar 488/594.

penetrating the membrane. However, the increase in the intensity in the red channel is only moderate. The reason for this is twofold: the quantum yield of the acceptor is significantly lower than the quantum yield of the donor ($\Phi_A = 0.22$ in contrast to $\Phi_D = 0.79$) and the labeling stoichiometry is disadvantageous. Two times more proteins are labelled only with a donor than being correctly labelled with a donor and an acceptor [45]. The area enclosed with the green ellipse can be either attributed to a defect in the membrane resulting in a stronger adsorption at this place or to an adsorbed aggregated protein complex. Nevertheless, raster-scanning of the membrane can be used to avoid taking measurements at these points. After directly placing the focus in the center of the images in figure 4.22, each time trace was recorded for 30 minutes in order to get sufficient statistics. Figure 4.23 **a)** shows a part of one recorded transient intensity time trace. Here, the intensities in the green and red channel were plotted as a function of time with a resolution of 500 µs per bin. It should be noted that the traces were directly corrected for the quantum yield of the fluorophores ($\Phi_A = 0.22$ and $\Phi_D = 0.79$) and the detection effciency in both channels ($\eta_A = 0.33$ and $\eta_D = 0.44$) [45]. A burst-like behavior

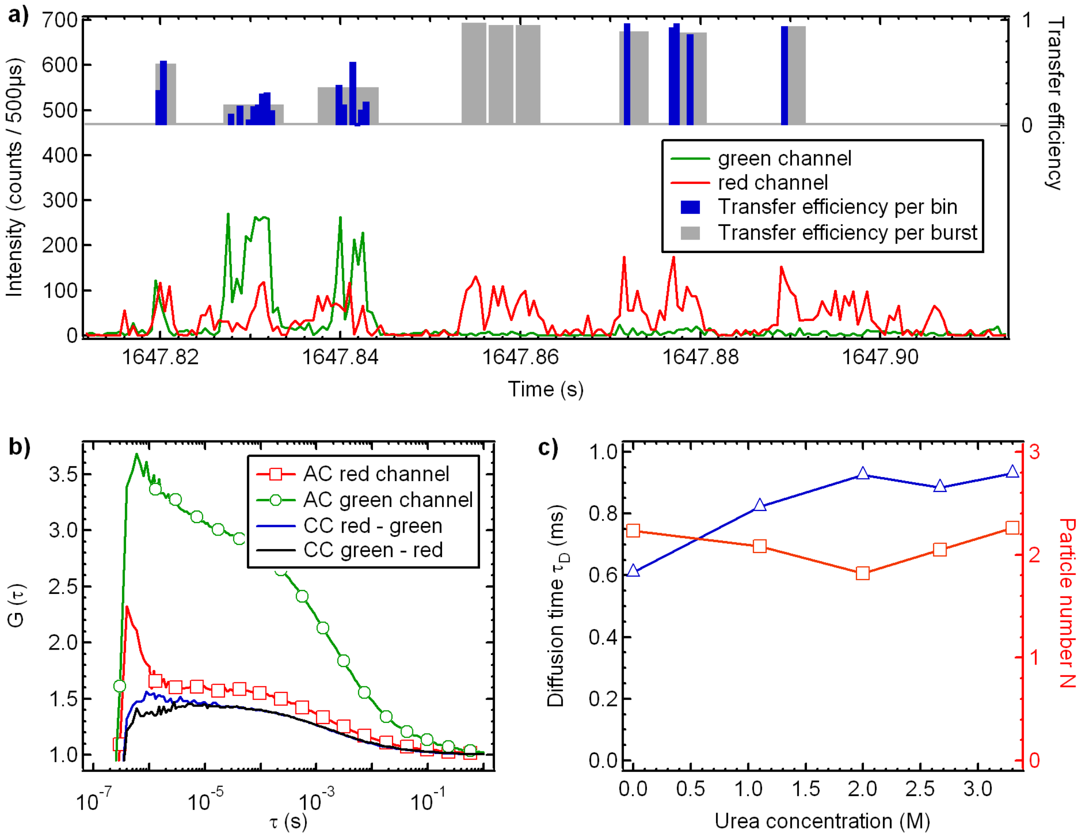

Figure 4.23: Analysis of measured time traces. **a)** (left axis) Cutout of the corrected timetraces in the green and the red detection channel as a function of time. (right axis) Calculated transfer efficiencies using a bin-based analysis (blue bars) and a burst-based analysis (gray bars). **b)** Auto- and cross-correlation functions for each possible constellation. **c)** Diffusion time τ_D and mean particle N as a function of the urea concentration.

was found, which can be analyzed in different ways. The simpliest method is to calculate the transfer efficiency for each single bin using equation 2.8 with $\gamma = 1$, because the correction was directly applied to the time traces. The blue bars in figure 4.23 **a)** correspond to the transfer efficiency per bin if the overall intensity of both channels exceeds 120 photons per bin. The gray bars in figure 4.23 **a)** correspond to bursts, which were found by the applied burst-search algorithm introduced in section 4.4. Due to the direct correction of the time traces, the criterion for the burst recognition was modified in the following way. Photons belong to a burst if at least $L = 300$ photons are detetcted in a number of bins with at least $M = 50$ photons per bin. The advantage of the burst-approach is that the history of an event can be used to obain a higher number of photons per burst than it is possible for a single bin. Thus, events can be used for calculating the transfer efficiency which would normally be discarded because they do not meet the threshold criterion of the single bin-approach. Moreover, detecting a higher photon number by averaging over several bins will give better statistics for the transfer efficiency histograms. Figure 4.23 **b)** shows the auto- and cross-correlation functions for each possible constellation. All correlations show the prolonged diffusion time of one-dimensional diffusion. Comparing the amplitudes of the auto-correlation functions in the green and the red channel, respectively, the amplitute is higher for the green channel, implying an apparent smaller particle number. However, as known from the stoichiometry of the protein labeling, more donor-only proteins are expected than molecules bearing both donor and acceptor. This finding can be explained by the strong influence of the background intensity especially for the red channel. Measuring the transfer efficiencies is performed with very low concentrations of the probes. Thus, the influence of the background either from the membrane or adsorbed molecules can be huge. Both auto-correlation functions show an increase in the correlation at time scales around 1 µs, which can be attributed to afterpulsing, and around 10 µs, which can be attributed to populated triplet states.

In addition, figure 4.23 **b)** shows the two cross-correlation functions of the red versus the green channel and the green versus the red channel. The slight discrepancy of both functions at short time scales is an experimental artifact caused by the detection electronics. Nevertheless, calculating the cross-correlation functions allows varifying the strong relation between the appearance of bursts in the red and the green channel. For example, after measuring the diffusion of a red and a green dye, which are not linked by a protein backbone, no cross-correlation function would be observable in contrast from being one for all times. Therefore, the excistence of a cross-correlation functions is a clear evidence for donor/acceptor labeled molecules diffusing through the detection focus.

Barstar 488/594 is a small protein and can be unfolded using urea. By unfolding the protein, the mean distance between the fluorophores increases and a drop in the transfer efficiency should be detectable. Here, a 8 M urea solution was added stepwise to force the unfolding of the protein. Between each step, transient intensity time traces were recorded within the membrane. As shown in figure 4.23 **b)**, the diffusion time, which was calculated using the red versus green cross-correlation function, increased from around $\tau_D = 0.6\,\mathrm{ms}$ to around $\tau_D = 0.9\,\mathrm{ms}$. The increase in the diffusion time can be attributed to several reasons: 1) the effective refractive index of the buffer- and urea-filled membrane changes due to the high concentrations of urea, which leads to a change in the size of the excitation/detection focus and 2) the (partial) unfolding of the protein leads to a different effective diffusion coefficient due to its increased hydrodynamic radius and its increased number of binding sites offered to the pore walls. However, the diffusion times are rather small for a protein. Similiar diffusion times were measured for freely diffusing dyes. Photobleaching due to the high excitation power is another effect, which might be responsible for the small diffusion times. If a fluorophore diffuses into the focus and bleaches, the auto-correlation function will interpret this result as an apparent shorter diffusion time.

The transfer efficiency histograms of Barstar 488/594 for different concentrations of urea are shown in figure 4.24. In general, three different regions can be defined for each histogram: 1) donor-only 2) donor + acceptor: unfolded conformational state, and 3) donor + aceptor: folded state. The first region (donor-only) shows low transfer efficiencies, as they are calculated for proteins, where only a donor is attached. Nevertheless, the correction for the low acceptor quantum yield introduces an artifical amplified background intensity in the red detection channel, which can not be prevented. Moreover, the uncorrelated background fluorescence of the membrane, which is in almost any case higher than in bulk solution, causes an additional broadening of the peak up to apparent transfer efficiencies of 0.5 - 0.6. Within the second region, the peak corresponds to the unfolded protein with a larger donor to acceptor distance than in the folded state, which belongs to the third region. It was shown by Hofmann and coworkers for

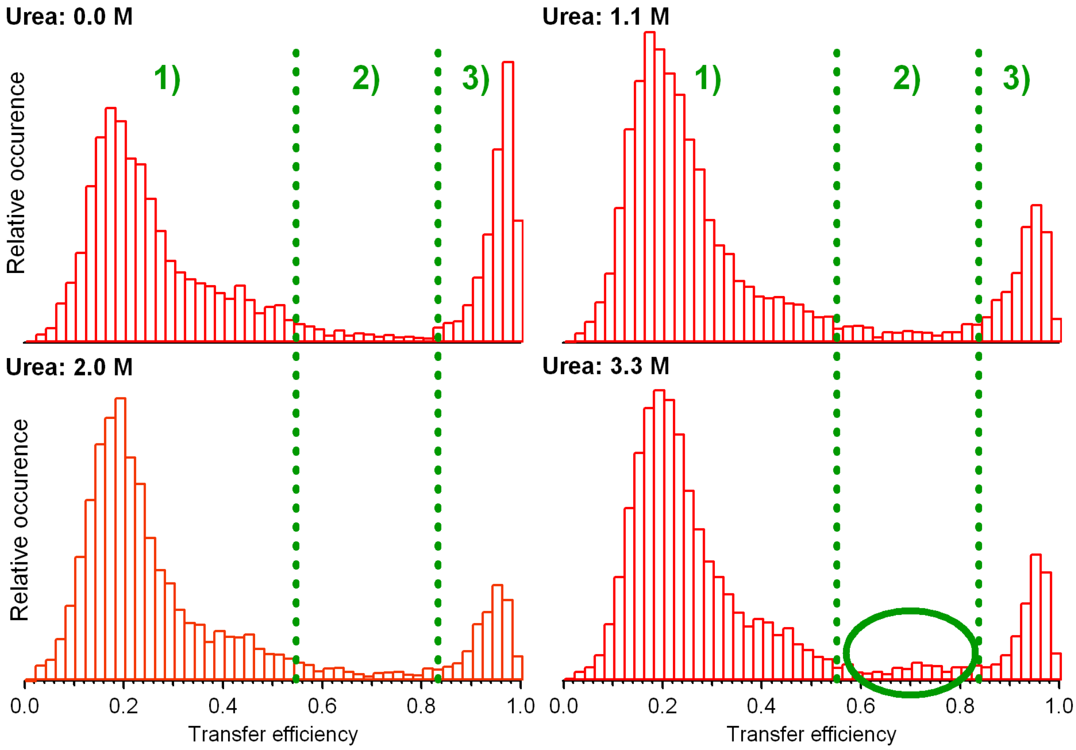

Figure 4.24: Histograms of the calculated transfer efficiencies for different concentrations of urea. For each concentration, the corrected transient timetraces were analyzed using a burst-search algorithm. The green ellipse indicates the area, where the peak of the unfolded protein was expected.

Barstar 488/594 diffusing in free solution that the peak position of the unfolded proteins shifts from around 0.7 for an urea concentration of 1.1 M to 0.55 for an urea concentration of 5.2 M [45]. The folding to unfolding transition is reversible for Barstar 488/594. The equilibrium of folded and unfolded proteins (equal rate constants for folding / unfolding) is attained for a urea concentration of around 2 M.

As shown in 4.24, the first and the third region are populated for each concentration of urea whitin the solution. However, no significant unfolded population occurs in the measurements. Only a very small peak can be seen for the highest urea concentration (marked by the green ellipse). These histograms differ from those obtained with free solution, where a significant fraction of unfolded proteins was found for urea concentrations higher than 1 M. There are a number of open questions which cannot be answered yet: 1) What is the actual concentration of urea within the pores? 2) Does the urea adsorb on the pore walls? 3) What is the influence of the single fluorophore on the diffusive behavior of the labeled protein within the membrane? 4) Are the rate constants of folding/unfolding within the membrane equal to those in free solution? As mentioned above, the experiment suffers from a number of drawbacks in particular the low acceptor quantum yield and the unsatisfying stoichiometry. Moreover, using an acceptor dye which can be directly excited by a pulsed laser would allow using more sophisticated energy transfer detection schemes as introduced in section 2.4. With such a scheme, the sorting of proteins in respect to their degree of labeling is possible and allows, for example, to discriminate between low-FRET proteins and proteins which are only labeled with a donor dye.

Chapter 5

3D-orientation determination of single molecules

Overview

One of the unique features of single molecule absorption and emission is their anisotropy due to the well-defined transition dipole for both processes, which allows the determination of the molecule's orientation. While polarization-resolved techniques can commonly detect only a projection of the transition dipole, several methods have been proposed to determine the full three-dimensional orientation. Here, a newly developed detection scheme is presented in section 5.1, which allows for a shot-noise limited determination of the emission dipole orientation utilizing an annular mirror and a polarizing beam splitter combined with three detectors in a scanning confocal optical microscope. Monte-Carlo simulations are presented in section 5.2, evaluating the accuracy and the theoretical limits of the presented scheme for orientation determination. Moreover, the application of this methodology for the determination of the relative orientation of transition dipoles in crystalline poly(diacetylene) nanofibers in porous alumina is presented in section 5.3. A general discussion in section 5.4 will close this chapter.

5.1 Models and methods

The dipole emission I_{Em} in a homogeneous medium can be described in spherical coordinates according to

$$I_{Em} = (\sin\theta\cos\phi\,\hat{e_x} + \sin\theta\sin\phi\,\hat{e_y} + \cos\theta\,\hat{e_z})^2 \tag{5.1}$$

with the polar angle θ and the azimuthal angle ϕ. Figure 5.1 shows the corresponding plot, where the orientation of the emission dipole coincides with the z-axis. Interpreting the dipole emission as a probability distribution of the directions of emitted photons, it is obvious that most of the photons will be emitted close to the x, y-plane. Moreover, the probability of detecting a photon along the z-axis is essentially zero.

The main idea is to make use of the anisotropic nature of dipole emission. Therefore, the ratio of the integrated detection probabilities of two, sufficiently large areas is determined. These areas are defined by the detection scheme depicted in figure 5.2. The fluorescence light collected

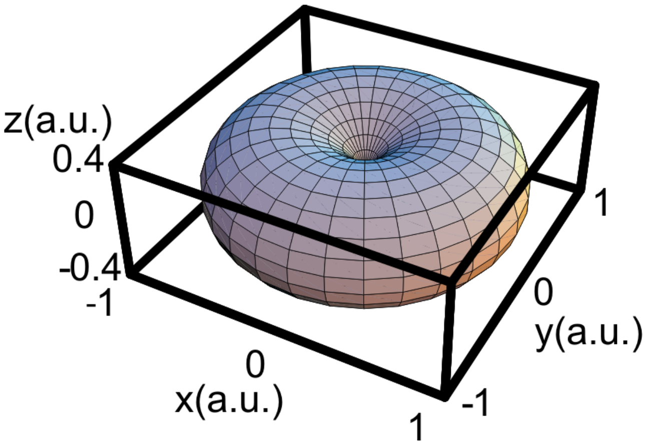

Figure 5.1: Normalized dipole emission plotted as a function of the polar angle θ and the azimuthal angle ϕ as defined in section 2.6. Here, the orientation of the dipole coincides with the z-axes. Whereas almost no emission occurs in the z-direction, the main contribution is emitted into the x- and y-plane.

by the microscope objective is split by an annular mirror and a polarizing beam splitter into three components. The annular beam splitter is a mirror with an elliptical aperture: light emitted in a hollow cone close to the rim of the microscope objective lens is reflected off the mirror while emission close to the optical axis is transmitted. The emission in the central cone is further divided into two orthogonally polarized contributions. All light components are focused onto avalanche photon diodes.

Figure 5.3 shows a more detailed view of the relation between dipole orientation and the fractions of light directed to the detectors. The area of the central cone is defined by $0 < \theta < \alpha_c$, where α_c is given by the annular beam splitter. The hollow cone is defined by $\alpha_c < \theta < \alpha_r$, where the cutoff angle α_r is given by the opening angle of the microscope objective. Here, by using an oil-immersion objective with $N.A. = 1.4$, α_r results in $\alpha_r = 67°$. For the determination of θ, two limiting cases can be discussed according to figure 5.3 **b+c)**. For $\theta = 0°$ only a small amount of light can be picked up by the central cone. In contrast, $\theta = 90°$ will give a high contribution to the central cone, whereas the fraction of light emitted into the rim of

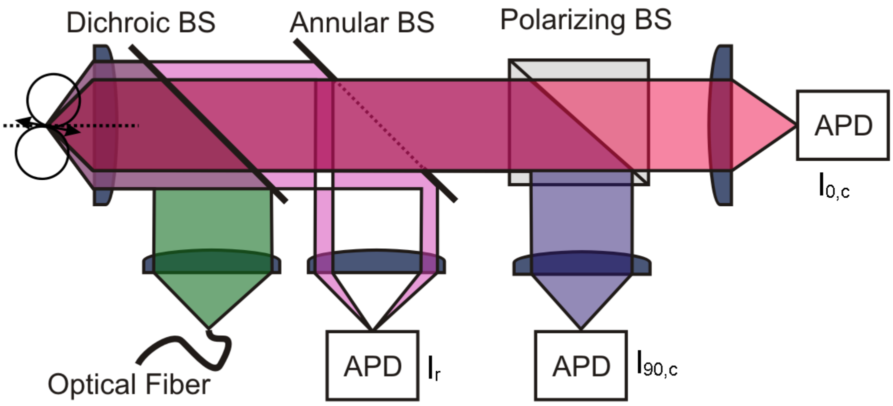

Figure 5.2: Diagram of the detection scheme for three-dimensional orientation determination of single molecules based on a confocal microscope. After excitation of the molecule, the emitted light is separated by an annular and a polarizing beam splitter into three fractions.

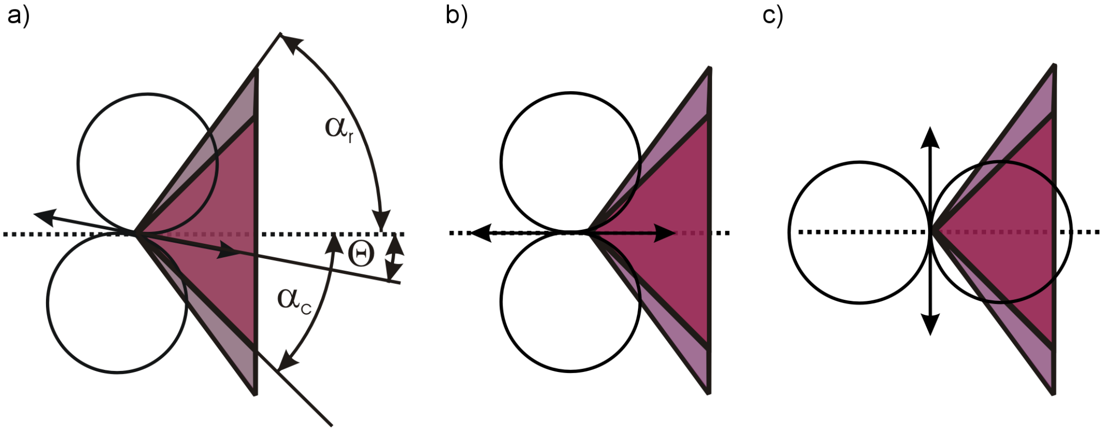

Figure 5.3: a) The orientation of the emission dipole according to the optical axis z is given by the polar angle θ. The angle α_c determines the inner cone of light, which can pass the annular beam splitter. The area between the angles α_c and α_r determine the fraction of light which is reflected by the annular beam splitter. **b)** First limiting case ($\theta = 0°$): Almost no light is emitted into the inner cone. **c)** Second limiting case ($\theta = 90°$): Most light is emitted into the inner cone.

the objective lens remains almost constant for both cases. The limiting cases will be of great importance during discussion of the accuracy of the proposed method.

Generally, the emission intensities in the central cone I_c and in the outer cone I_r can be expressed according to [26, 47],

$$I_r(\theta,\phi) = 2I_{tot}(t,t+\tau)\left[(A_r - A_c) + (B_r - B_c)\sin^2\theta\right] \tag{5.2}$$

$$I_{0,c/90,c}(\theta,\phi) = I_{tot}(t,t+\tau)\left[A_c + B_c\sin^2\theta \underset{90,c}{\overset{0,c}{\pm}} C_c\sin^2\theta\cos 2\phi\right] \tag{5.3}$$

$$I_c(\theta,\phi) = I_{0,c}(\theta,\phi) + I_{90,c}(\theta,\phi) = 2I_{tot}(t,t+\tau)\left[A_c + B_c\sin^2\theta\right] \tag{5.4}$$

with I_{tot} as the total emitted intensity integrated over all directions in space for a given time period and the following variables

$$A_{c,r} = \frac{1}{6} - \frac{1}{4}\cos\alpha_{c,r} + \frac{1}{12}\cos^3\alpha_{c,r} \tag{5.5}$$

$$B_{c,r} = \frac{1}{8}\cos\alpha_{c,r} - \frac{1}{8}\cos^3\alpha_{c,r} \tag{5.6}$$

$$C_{c,r} = \frac{7}{48} - \frac{1}{16}\cos\alpha_{c,r} - \frac{1}{16}\cos^2\alpha_{c,r} - \frac{1}{48}\cos^3\alpha_{c,r}, \tag{5.7}$$

which are fully defined by the detection angles α_c and α_r.

With the common definition of the polarization P as $P := (I_{90,c} - I_{0,c})/(I_{90,c} + I_{0,c})$ and defining correspondingly an inclination N as $N := (I_r - I_c)/(I_r + I_c)$, the polar angle θ and the azimuthal angle ϕ can be calculated according to

$$\theta = \arcsin\sqrt{-\frac{2A_c - A_r + A_r N}{2B_c - B_r + B_r N}} \tag{5.8}$$

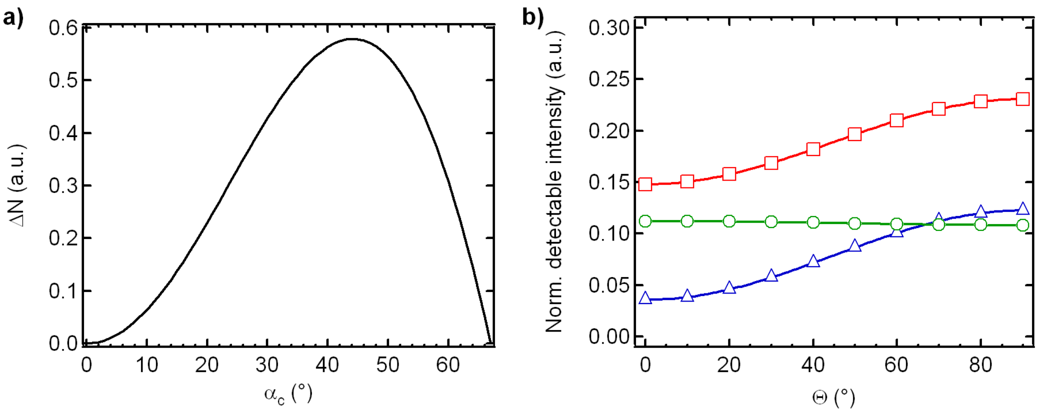

Figure 5.4: **a)** ΔN (see equation 5.10) as a function of α_c using a fixed detection angle of $\alpha_r = 67°$, which is defined by the numerical aperture of the microscope objective. ΔN defines the achievable contrast for determination of θ and reaches a maximum value for $\alpha_c = 44°$. **b)** The center intensity I_c (-△-), the intensity in the rim I_r (-○-) and the total detectable intensity I_D (-□-) as a function of θ and using $I_{tot} = 1$. Detection angles of $\alpha_c = 44°$ and $\alpha_r = 67°$ where used for calculations according to equations 5.2-5.4.

and

$$\phi = \frac{1}{2} \arccos \left(-P \frac{A_c + B_c \sin^2 \theta}{C_c \sin^2 \theta} \right). \tag{5.9}$$

N and P are invariant against the sign of θ and ϕ. This leads together with the symmetry of dipole emission to an eightfold orientation degeneracy for a given $\{P, N\}$ pair and to a range of θ and ϕ from 0° to 90°.

In order to find the optimal value for α_c, we consider the range of possible values $N(\alpha_c, \alpha_r, \theta) = (I_r - I_c)/(I_r + I_c)$. The angle α_c where the range $\triangle N$

$$\triangle N = \sqrt{(N_{\theta=0°} - N_{\theta=90°})^2} \tag{5.10}$$

has a maximum value can be found by calculating $d\Delta N / d\alpha_c = 0$. Figure 5.4 **a)** shows ΔN as a function of the cuttoff angle α_c with a fixed rim angle α_r. Using a rim angle of $\alpha_r = 67°$ results in an optimal cutoff angle of $\alpha_c = 44°$. For this cutoff angle, N is defined between $N_{\min} = -0.08$ and $N_{\max} = 0.5$ and the contrast for determination of θ is maximized. Now, the detectable intensities $I_c (= I_{90,c} + I_{0,c})$, I_r and $I_D (= I_c + I_r)$ can be plotted as a function of θ as shown in figure 5.4 **b)**. In contrast to the rim intensity I_r, which is almost constant for each θ-value, the center intensity I_c increases with higher values of θ. Note that the total detectable intensity I_D is only a function of θ and varies between 15% and 25% of the light emitted by a single fluorophore.

Monte-Carlo simulations of orientation determination

The convolution of the collimated laser beam and the collection efficiency function can be approximated by a two-dimensional Gaussian in the x- and y-plane. The spatial intensity distribution $I(x, y)$ of a confocal microscope can be written as

$$I(x, y) = I_0 \exp \left(-2 \frac{(x - x_0)^2 + (y - y_0)^2}{w_0^2} \right), \tag{5.11}$$

where I_0 represents the maximum excitation intensity, x_0 and y_0 the center of the focus and w_0 the effective beam waist in the radial direction. Defining $I_{tot} := I_0/Q$ as the total detectable intensity of the emitted light in the whole space, where $Q = \sigma_{\text{exc}}\phi_f\kappa$ represents the product of the excitation cross section of the fluorescent molecules σ_{exc}, their fluorescence quantum yield ϕ_f, and the setup-specific efficiency of detection of fluorescence κ [112], the detectable intensity I_D through the objective can be written according to

$$I_D = I_r + I_c = 2 \cdot Q\left(A_r + B_r \sin^2\theta\right) I_{tot} \exp\left(-2\frac{(x-x_0)^2 + (y-y_0)^2}{w_0^2}\right). \tag{5.12}$$

In the following, Q is set to unity without loss of generality.

The shot-noise nature of dipole emission is taken into account using a Poisson distribution, where the probability P of detecting k photons with an expectation value of λ is given by

$$P(X = k) = \frac{\lambda^k e^{-\lambda}}{k!}, \tag{5.13}$$

with k = 0,1,2,... and $\lambda > 0$. Furthermore, the Poisson distribution is characterized by $\lambda = \sigma^2$, where σ represents the standard deviation. The orientation, position (if applicable), and number of detected photons subject to a Poisson distribution are stochastically generated by Monte-Carlo methods implemented in Igor (Wavemetrics). Three types of simulations were carried out, namely simulations of orientation-resolved images (**type A**) and simulations of orientation-resolved transients (**type B** and **type C**).

For simulations of **type A** 8 molecules were placed at randomly distributed positions defined by $x_{0,i}$ and $y_{0,i}$ within an area of 5×5 µm (128×128 pixels). Coordinate z was set to zero. The azimuthal angles $\phi_{0,i}$ and the polar angles $\theta_{0,i}$, which determine the individual orientation of the emission dipole, were randomly distributed following a uniform distribution for azimuthal angles and a sinusoidal distribution for polar angles corresponding to the surface area element in polar coordinates. The intensities $I_{0,c}$, $I_{90,c}$ and I_r were calculated for each pixel by using equations 5.2 and 5.3 with $I_{tot} = 2000$ photons, $w_0 = 0.25$ µm, $\alpha_r = 67^\circ$ and $\alpha_c = 44^\circ$. Every calculated intensity value was used as a mean λ in equation 5.13 to stochastically generate a new intensity following Poisson distribution. The obtained image is just the sum of the intensities of the eight molecules. Finally, Poisson-distributed background luminescence of 5 photons per pixel was added pixel-by-pixel to $I_{0,c}$, $I_{90,c}$ and I_r.

For simulations of **type B** and **type C** one single molecule at a time was placed in the center of the intensity distribution, i.e. $x = y = x_0 = y_0 = 0$, with a fixed orientation defined by the azimuthal angle ϕ_0 and the polar angle θ_0. To mimic a time-dependent experiment, the procedure of adding noise to the beforehand calculated intensity ratios was carried out several thousand times. For simulations of **type B**, the total number of emitted photons per second was set to half a million. Assuming a time resolution of 2ms, the corresponding total intensity I_{tot} was set to $I_{tot} = 1000$ photons for each bin. The duration of the simulated transient time trace was 100 s.

As it was shown in equation 5.12, the detectable intensity I_D is a function of the polar angle θ. Instead of using $I_{tot} = const.$ as for simulations of **type B**, simulations of **type C** follow a different approach. Here, the probability of detecting a single photon in one of the three detectors is calculated as a function of the orientation using $I_{tot} = 1$. Poissonian-distributed noise is added to each probability. This addition of noise is iterated and the cumulative number of detected photons is stored, until a beforehand defined number of photons I_{No} is reached for this bin. The advantage of this approach is twofold: the θ-dependence of the detection probability is circumvented, and the number of detected photons per bin can be attributed to different binwidths. For simulations of **type C**, different numbers of photons per bin [either $I_{No} = 500$ or $I_{No,m} = 100 \cdot 2^{m/2}$, with $m = 0, 1, 2...$ was used] and different initial orientations $[\phi_{0,i}(\theta_{0,i}) = 0°, 5°, ..., 90°]$ were used. The overall number of simulated bins was set to 200.

Additionally, for simulations of **type B** the addition of background photons was slightly modified. In contrast to the anisotropic nature of dipole emission, the nature of background emission is considered being isotropic. In this case the ratio between the detected background intensity in the center and the overall detected intensity is given by the ratio of the solid angles

$$\Delta\Omega = \frac{2\pi(1-\cos\alpha_c)}{2\pi(1-\cos\alpha_r)} = \frac{2\pi(1-\cos 44°)}{2\pi(1-\cos 67°)} = 0.46. \tag{5.14}$$

In other words, 46% of the isotropic background intensity will be detected in the center (and therefore 23% in each of the two detectors) and 54% will be detected in the rim.

Note that this result is slightly different from the case of superposition of randomly oriented dipoles. This would lead to a determination of $\theta = 60°$ and $\phi = 45°$ (magic-angle condition) according to the uniform distribution for azimuthal angles and the sinusoidal distribution for polar angles corresponding to the surface area element in polar coordinates. In this case, using $\alpha_r = 67°$ and $\alpha_c = 44°$ leads to $I_{rim}(\theta = 60°) \simeq I_c(\theta = 60°)$. Therefore, half of the detectable background intensity I_{Bg} would be detected by the rim detector and the other half would be directed to the two detectors for the central beam. For sake of simplicity, if not stated otherwise, no background was added to simulations of **type C**.

Using these intensity patterns of simulations of **type B** and **type C** allows for re-calculating the orientations of the molecules bin by bin as a function of the beforehand defined azimuthal angles $\phi_{0,i}$, the polar angles $\theta_{0,i}$, the excitation intensities defined by $I_{No,m}$, and the detectable background intensity I_{Bg} in order to study the influence of the shot-noise nature to orientation determination. The distributions of re-calculated angles can be characterized by their mean and their standard-deviation.

5.2 Results of simulations

Figure 5.5 shows a simulation of **type A** after placing a set of molecules with randomly chosen orientation into a scanning area. The three detectable intensity images ($I_{0,c}$, $I_{90,c}$ and I_r) and their sum I_{sum} [$\equiv I_D$] show the typical Gaussian intensity distribution reflecting the point spread function. The intensity images of $I_{0,c}$ and $I_{90,c}$ show different maximum intensities for the molecules, whereas the images of I_r and I_{sum} look rather uniform. Nevertheless, it is obvious that different orientations of the molecules lead to different detectable intensities, which is a direct result of the anisotropy of dipole emission. After setting a appropriate intensity threshold value, the calculated intensity patterns were further used to re-calculate the azimuthal angles ϕ_i and the polar angles θ_i pixel by pixel according to the equations 5.9 and 5.8. Each molecule is labelled with the initially used angles $\phi_{0,i}$ and $\theta_{0,i}$ for comparison. The averaged reconstructed values for each molecule are well in line with those initially set. However, there are several distinctive features: 1) not every molecule shows an uniform angular pattern, 2) especially molecules with a high θ-value show a lot of missing pixels (→white pixels), and 3) the fringes of some molecules show mean values different from those of the inner part. In contrast, figure

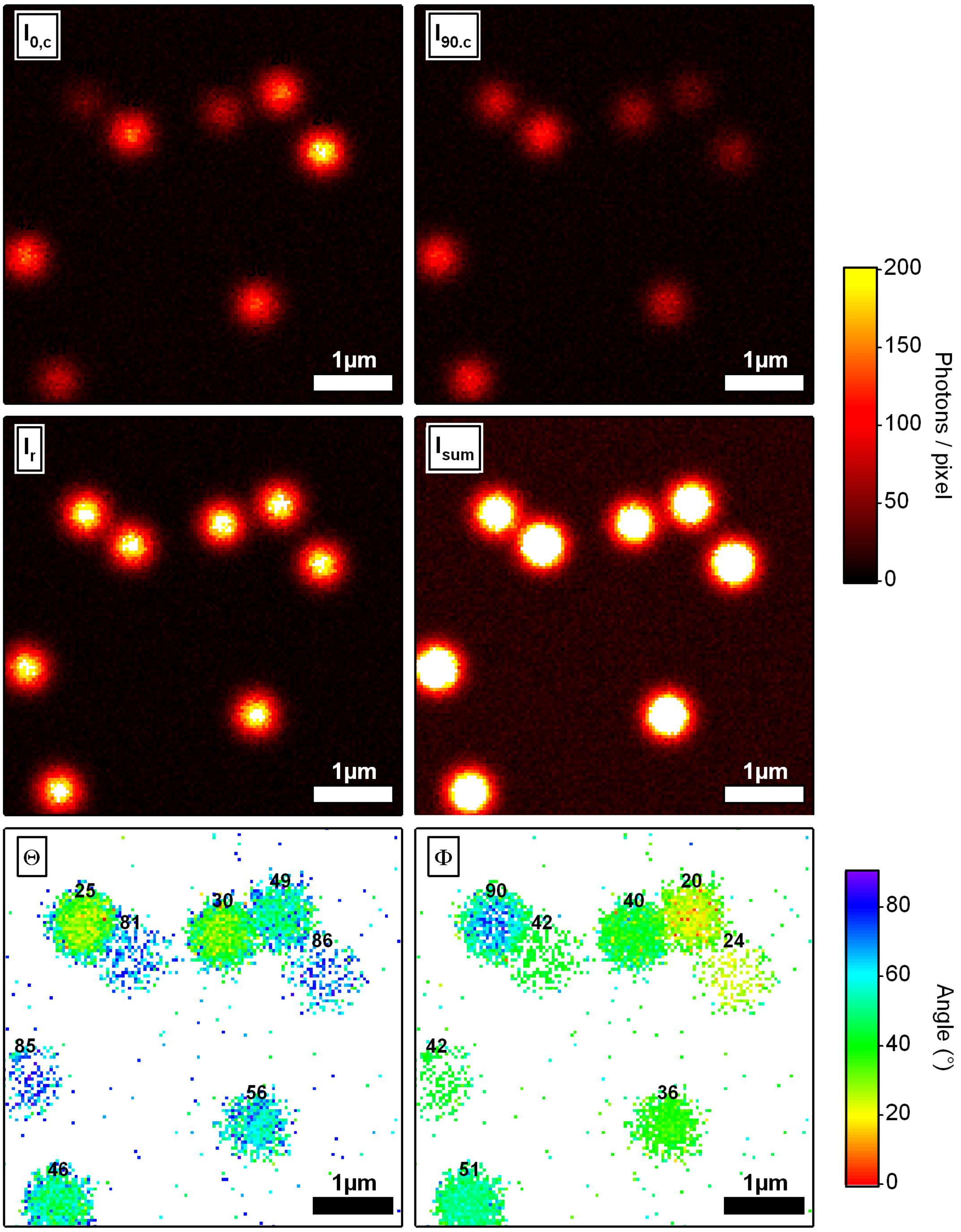

Figure 5.5: Simulations of **type A** of 8 randomly oriented and randomly distributed molecules on an area of 5 µm by 5 µm. $I_{0,c}$, $I_{90,c}$ and I_r show the pseudo color-coded, calculated fluorescence intensity as it would be detected after scanning the area with a confocal microscope. I_{sum} represents the sum of the previous intensities. After setting an appropriate threshold, the intensities were used to re-calculate the orientation patterns θ and ϕ pixel by pixel. Note that for all calculated intensities Poissonian noise was added.

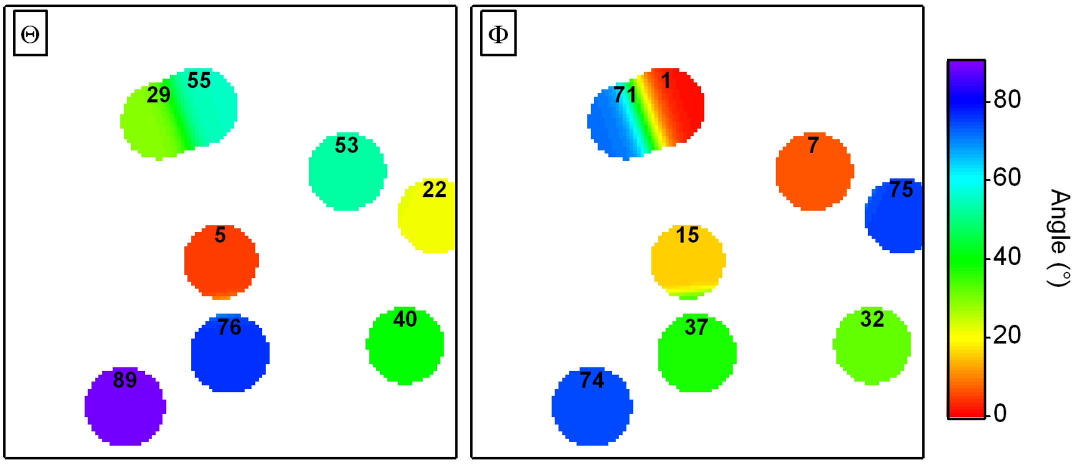

Figure 5.6: Simulations of **type A** of 8 randomly oriented and randomly distributed molecules on an area of 5 µm by 5 µm showing the re-calculated orientation patterns of θ and ϕ. Note that no background intensity and no Poissonian noise was added to the calculated intensity patterns (intensity patterns are not shown).

5.6 shows angular patterns of θ and ϕ, where the calculated intensity patterns (data not shown) were not Poissonian distributed pixel by pixel afterwards. Here, each molecule shows an uniform and perfect representation of the initial orientation, as long as no overlap of the molecules occurs. This possible overlap, as shown in figure 5.6, is a very interesting feature. As long as the orientations of those molecules are sufficiently different, the calculated angular patterns allow an easier spatial separation than the intensity pattern. Note that the overall emitted intensity of one single molecule is a function of θ. The molecules with the highest values of θ dominate the other ones according to figure 5.4 **b)**.

Comparing the angular patterns of figures 5.5 and 5.6 reveals that the shot-noise nature of photon emission is the main limiting factor for three-dimensional orientation determination. Generally speaking, every orientation of a fluorophore is defined by a particular relation between the intensities $I_{0,c}$, $I_{90,c}$ and I_r. However, due to the shot-noise nature of photon emission, only a probability distribution of detectable intensities can be given. After adding the Poisson-distributed noise to the detectable intensities, the initial particular relation between the intensities is changed. Re-calculation of the orientation will lead to apparently altered values of θ and ϕ, as long as there is still an orientation defined for the new relation of the intensities. Especially for values of $\theta,\phi \simeq 0°$ or $\theta,\phi \simeq 90°$ ($0° \leq \phi,\theta \leq 90°$), the set of valid intensity-relations is limited. This is the reason for the "missing" pixels in figure 5.5. The calculation of ϕ is based on the calculation of θ; missing pixels in the θ pattern will automatically lead to missing pixels in the ϕ pattern. To solve this problem, pixels from forbidden intensity-relations can be filled either with $\theta,\phi = 0°$ or $\theta,\phi = 90°$ according to the nearest valid relation. The overall number of valid relations is a function of the detected intensities: if the detected intensities (and therefore the overall number of emitted photons) is high, the Poissonian nature of photon emission becomes less relevant.

Simulations of **type B** were performed in order to elaborate the effect of the Poissonian photon statistics in transient time traces. After fixing the orientation of an emission dipole to $\theta_0 = 60°$ and $\phi_0 = 25°$ the three detectable intensities $I_{0,c}$, $I_{90,c}$ and I_r were calculated for each

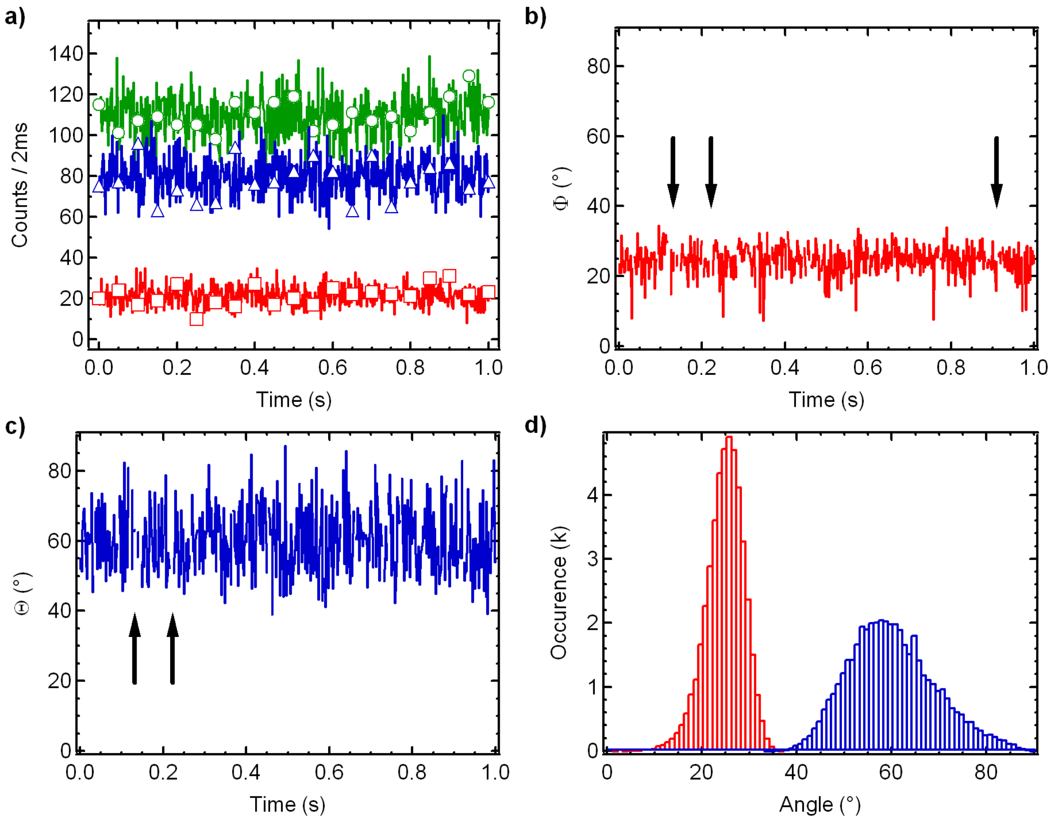

Figure 5.7: Simulation of transient time traces for orientation determination of the emission dipole of single molecules. The initial orientation was fixed to $\theta_0 = 60°$ and $\phi_0 = 25°$. **a)** Detectable time-traces using $I_{tot} = 1000$ photons per 2 ms: $I_{0,c}$ (-△-, spare symbols every 25th data point), $I_{90,c}$ (-□-), and I_r (-○-). **b+c)** Re-calculated orientations of ϕ and θ. Note that the lines are interupted (as indicated by the arrows). **d)** Histograms of the re-calculated angles ϕ (red, left) and θ (blue, right)

bin with a width of 2 ms using $I_{tot} = 1000$ photons per bin. Figure 5.7 **a)** shows sections of the transient time traces. The fluctuations in the intensities are only caused by the shot-noise nature of photon emission. Note that the time-resolution is 2 ms. During this time the total detected intensity of each bin is about 210 photons. In figure 5.7 **a+b)** this number of detected photons is sufficient to re-calculate ϕ and θ with high reliability. Nevertheless, it should be noted that the traces of the recalculated angles are interupted, were the relation of the three detected intensities exceeds the defined range due to shot noise. The histograms of ϕ and θ re-calculated from the full intensity traces are shown in figure 5.7 **d)**. Due to the non-linearity of the equations for calculating the angles, the finding of the non-symmetric angle distributions is not unexpected. The re-calculated mean values ($\theta_{avg} = 59.9° \pm 9.3°$ and $\phi_{avg} = 24.5° \pm 4.1°$) are in almost perfect agreement with the initially set values of $\theta_0 = 60°$ and $\phi_0 = 25°$. However, the initially chosen orientation is a "friendly" one; the angles are neither close to 0° nor to 90°. The problems arising from orientations close to 0 and 90°, the influence of the number of detected photons per bin on the reliability of three-dimensional orientation determination, and the most important question what conclusions can be drawn from the simulations for the experiments will be discussed in the following. Simulations of **type C** were performed for this purpose. As described in section 5.1, simulations of **type C** feature a constant number of detected photons per bin instead of defining a constant number of emitted photons by I_{tot}. The number of detected photons is composed by the probabilities of detecting photons in one of the three channels representing $I_{0,c}$, $I_{90,c}$ and I_r. Figure 5.8 shows such a simulation with 500 photons per bin and a duration of simulation of 200 bins. The initial orientation was varied from 0° to 90° in steps of 5° for all angles $\theta_{0,i}$ and $\phi_{0,i}$. Note that bins featuring non-valid ratios of the intensities are discarded and not assigned to a certain value. Figure 5.8 **a+b)** show the pseudo color-coded re-calculated mean orientation of all bins of one orientation trace as a function of the initially set values of $\theta_{0,i}$ and $\phi_{0,i}$. In the case of the re-calculated θ-values, they are well in line with the initially set values as long as $\theta \neq 0°$ and $\theta \neq 90°$. According to the arc sine and the square root in equation 5.8, θ is only defined between 0° and 90°. If the shot-noise nature of photon emission causes new relations of the three detected intensities which differ from the initial ones, only those contribute to the re-calculation which are still valid. This is the reason why the re-calculated average θ-value is slightly higher for $\theta_{0,0°}$ and slightly lower for $\theta_{0,90°}$ than expected. The re-calculated ϕ-values show a different behavior. If the initial θ_0-value is smaller than 10°, every initial $\phi_{0,i}$-value leads to a re-calculated value with a averaged value of around $\phi \simeq 45°$. To explain this finding let us take the limit of equation 5.9 according to

$$\phi = \frac{1}{2}\arccos\left(-P\frac{A_c + B_c \sin^2\theta}{C_c \sin^2\theta}\right) \quad \rightarrow \quad \phi = \lim_{\theta \to 0°}\left(\frac{1}{2}\arccos(0)\right) = 45°. \tag{5.15}$$

Small values of θ result in almost indeterminable ϕ-values, which is obvious taking into consideration that small θ means an orientation almost parallel to the optical z-axis.

The considerations for initial θ-values around 0° or 90°, as discussed above, do also hold for ϕ-values around 0° or 90°. Nevertheless, re-calculation of ϕ benefits from large values of θ: if $\theta_{0,i}$ is larger than 80°, the re-calculated ϕ-value maches almost perfectly the initial ϕ_0 -value. Figure 5.8 **c+d)** represent the standard deviation of the re-calculated angles as a function of their initial values. For the re-calculated θ-values, the standard deviation is in any case smaller than 10°, which is a reasonable value keeping in mind that the overall number of detected photons was restricted to only 500 photons per bin. With increasing initial values of $\theta_{0,i}$, the standard deviation increases from 2.5° to around 8°,due to the non-linearity of the equations for calculating the orientation. For small $\theta_{0,i}$ angles the determination of ϕ leads to apparent values, as can be seen in figure 5.8 **b)**. It is not surprising that the standard deviation is indeed large (around 15°). With increasing values of $\theta_{0,i}$, the standard deviation drops below 5°, which does make the detection scheme very suitable for determination of the azimuthal angle. Moreover, one should keep in mind that, assuming a completely random distribution of dipole orientations, the distribution of the polar angle θ scales with its sine and orientations with small angles of θ are rare.

Figure 5.8 **e+f)** serves the purpose to estimate how many of the 200 calculated bins are valid for re-calculation of either θ or ϕ. Both images support the previous findings: values of $\theta_{0,i}$ close to 0° or 90° hamper the re-calculation of those initial values. In fact, by using these values almost 60% of the calculated bins contain non-valid intensity ratios. The re-calculation of ϕ-values is even more difficult due to the fact that the calculation of ϕ-values is based on the calculation of θ-values. For this reason, re-calculation of ϕ suffers from ϕ-values close to either 0° or 90° and, additionaly, from θ- values close to either 0° or 90°. Especially for large

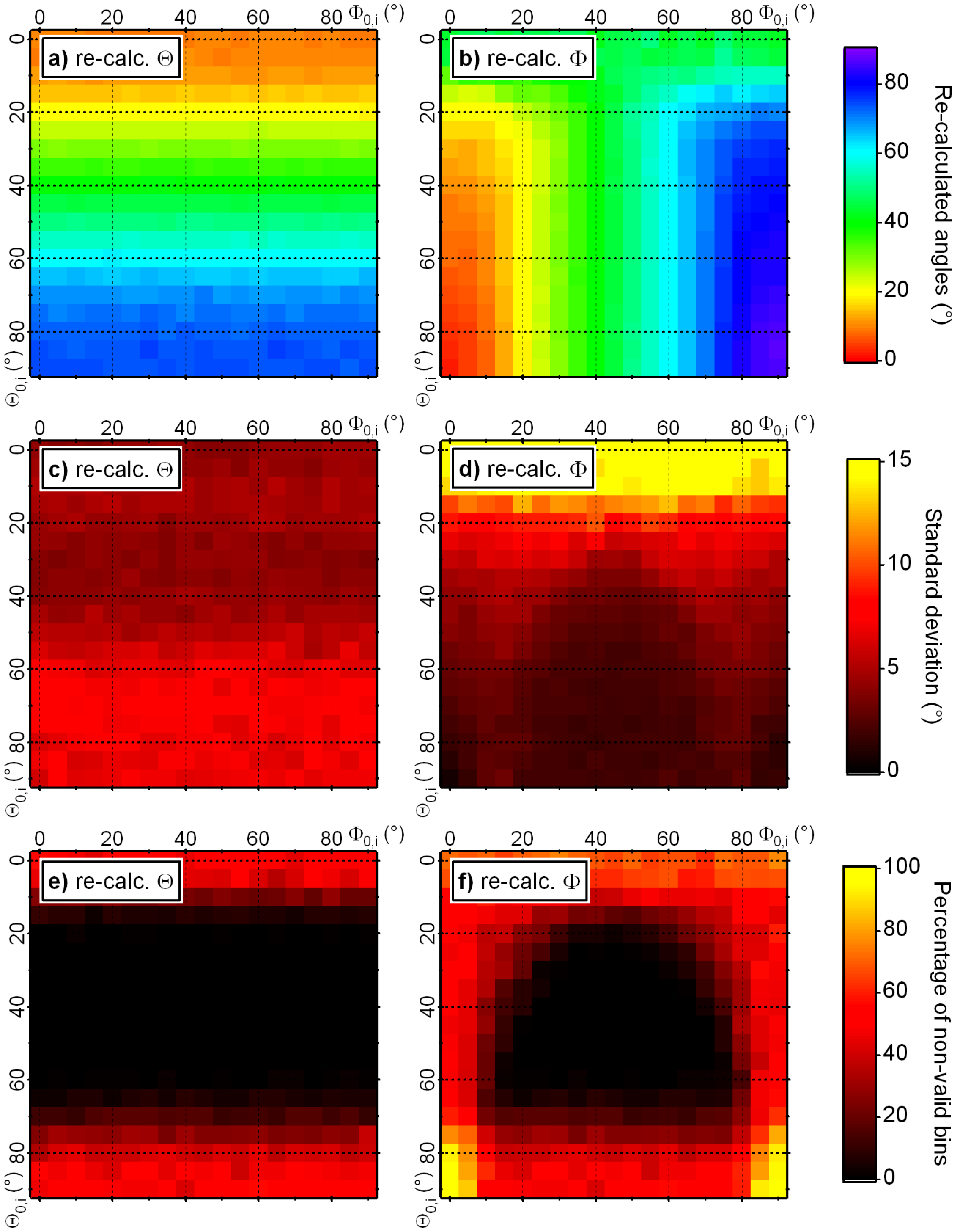

Figure 5.8: Simulations of **type C** for three-dimensional orientation determination. Different properties are plotted using pseudo-coloring as a function of the initial orientation defined by the values of $\theta_{0,i}$ and $\phi_{0,i}$. Undefined ratios of the calculated detectable intensities were not fixed. **a+b)** Re-calculation of θ and ϕ from the simulated detectable intensity traces. **c+d)** Standard deviation of the re-calculated angle-traces. **e+f)** Percentage of non-valid bins for re-calculation of the orientation out of the simulated intensity traces.

values of $\theta_{0,i}$ and $\phi_{0,i}$, there is almost no valid bin. This has to be taken into account if the apparent small standard deviations in figure 5.8 **d)** are considered.

As discussed previously, the non-valid ratios of detected (simulated) intensities can be set to

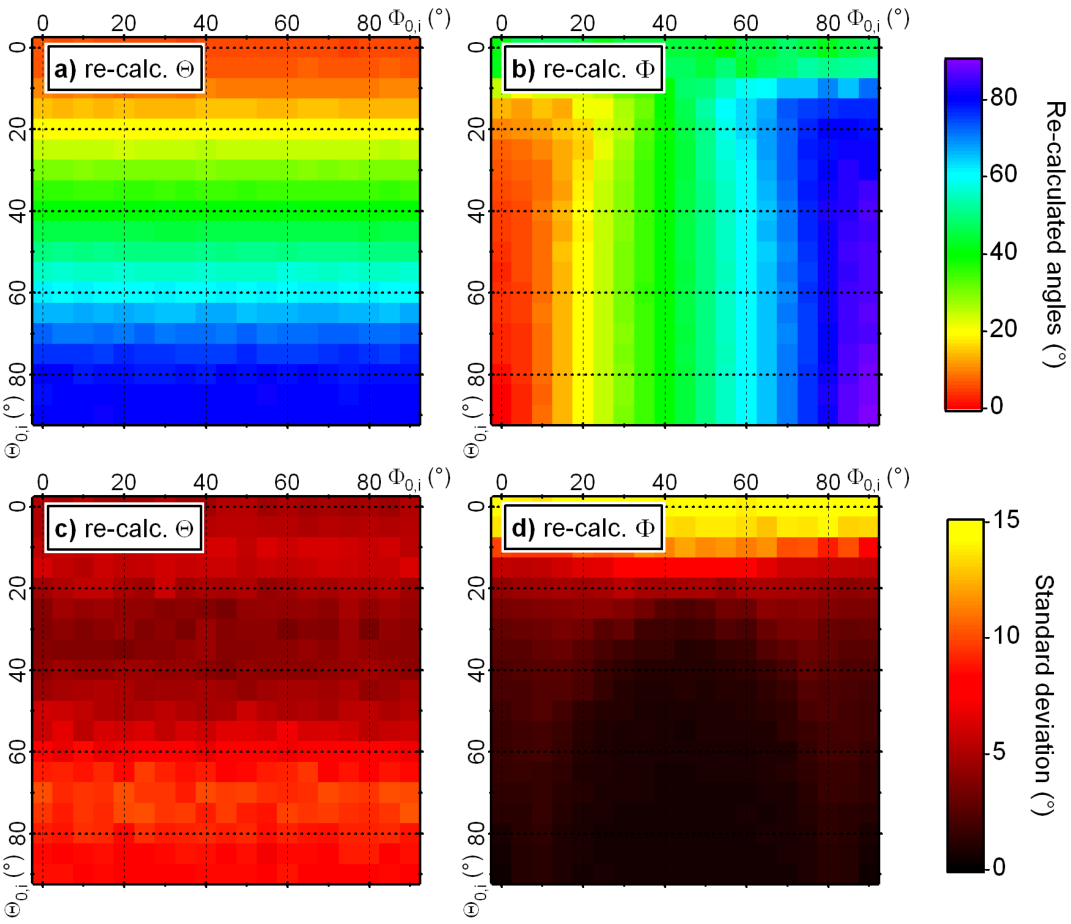

Figure 5.9: Simulations of **type C** for three-dimensional orientation determination. Different properties are plotted using pseudo-coloring as a function of the initial orientation defined by the values of $\theta_{0,i}$ and $\phi_{0,i}$. Non-valid ratios of the calculated detectable intensities were fixed to the nearest valid ratio. **a+b)** Re-calculation of θ and ϕ from the simulated detectable intensity traces. **c+d)** Standard deviation of the re-calculated angle-traces.

the next valid ones. As a result, the re-calculated angles θ or ϕ are either fixed to $\theta\,(\phi) = 0°$ or $\theta\,(\phi) = 90°$. Thus, the number of non-valid bins is zero. Figure 5.9 shows simulations using the same parameters as discussed before but with fixing non-valid ratios. As seen in figure 5.9 **a+b)**, the averaged re-calculated orientation at the edge is closer to the initial orientation than in figure 5.8. Especially re-calculation of ϕ benefits from this fixing of the angles at the edges as can be concluded from the reduced standard deviation in figure 5.9 **d)**, whereas the standard deviation for the re-calculated θ-values remains almost unchanged. In conclusion, 500 detected photons are sufficient for re-calculating the orientation, as long as the initial orientation is not close to values of either 0° or 90°. Therefore, in experiments attention should be paid to both angles. If, for example, a value of $\theta \simeq 5°$ was calculated, calculation of ϕ will lead to $\phi = 45°$ absolutely independend of the real ϕ-value.

In order to check the influence of the number of detected photons per bin on the accuracy of orientation determination, the following simulations are performed. Instead of going through all possible configurations of $\theta_{0,i}$ and $\phi_{0,i}$, the azimuthal angle ϕ_0 was fixed to $\phi_0 = 45°$ for each case. Only the initial values of $\theta_{0,i}$ were changed using stepwidths of 5°. As an additional parameter, the number of detected photons per bin was changed according to $I_{No,m} = 100 \cdot 2^{m/2}$,

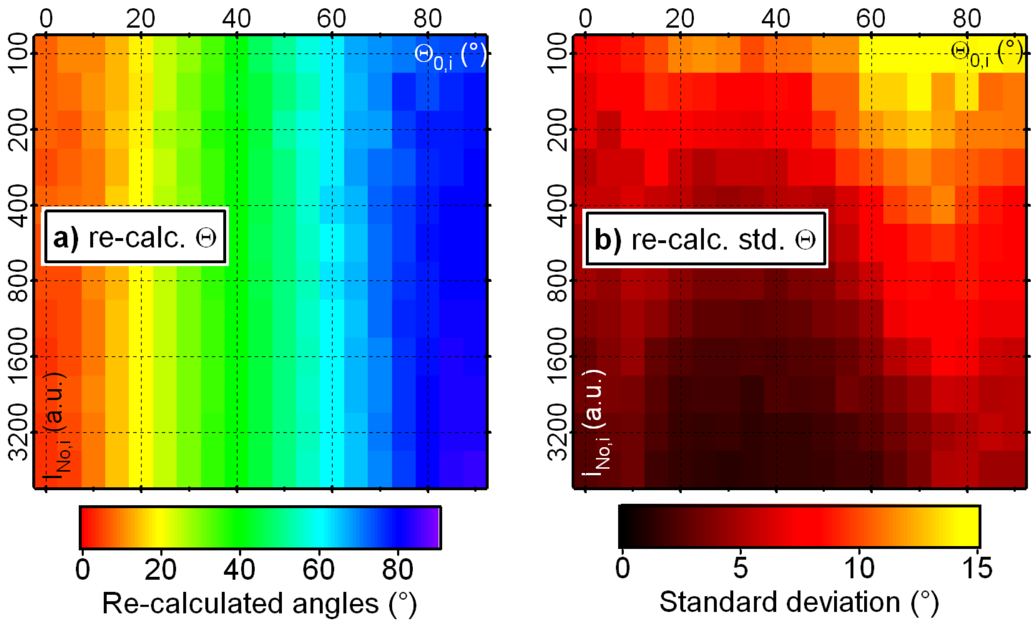

Figure 5.10: Simulations of **type C** for three-dimensional orientation determination. **a)** the re-calculated values of θ and **b)** the corresponding standard deviations are plotted as a function of the initial orientation $\theta_{0,i}$ and the number of detected photons per bin $I_{No,m}$ (logarithmic scale). No background noise was added to the simulations, ill-defined intensity ratios were fixed to valid ones.

with $m = 0, 1, 2, ..., 12$. The overall number of bins was set to 200. Figure 5.10 **a)** shows the averaged value of the re-calculated values of θ as a function of the initial $\theta_{0,i}$ and $I_{No,m}$. Again, all non valid-ratios were fixed to the next valid ones. Whereas the re-calculated mean values in figure 5.10 **a)** show only slight differences with an increasing number of photons per bin, the standard deviation drops significantly from around $\Delta\theta_{0,i} = 7° ... 15°$ for $I_{No,0} = 100$ photons per bin to $\Delta\theta_{0,i} = 0° ... 6°$ for $I_{No,12} = 4525$ photons per bin . This finding may indicate the potential time-resolution of the determination of the orientation of single molecules. Let us assume a detectable count rate of 200 kHz for an immobilized molecule with an arbitrary orientation of the emission dipole. Even with 100 photons per bin, the re-calculated mean θ-value reproduces the initial orientation with sufficient accuracy. Dividing 200000 photons per second with 100 photons per bin equals 2000 bins per second corresponding to a time resolution of 500 µs. The more photons are aquired for re-calculating the orientations, the higher the accuracy that can be obtained.

It should be explicitly mentioned that the orientation determination from experimental data is a so-called inverse problem. Even if the model applied for the MC simulations is straightforward, the interpretation of the re-calculated orientation using experimental data is rather complicated. In fact, there is no fitting function which could be used to fit the probability distributions obtained by re-calculating the orientation for a number of bins of one emission dipole. Moreover, as discussed above, re-calculating of ϕ-values for orientations with small θ-values will result in $\phi_0 \simeq 45°$.

From an experimental point of view, it is of interest with which probability a measured intensity distribution (and therefore a calculated orientation) corresponds to the actual orientation of the emission dipole. This issue is explored by the Bayes theorem [3], which relates the probability of an event A conditional on another event B to the (in generally different) probability of B conditional on A. Bayes claimed that the *a posteriori* probability $P(A \mid B)$ of detecting event A under condition of event B is related to the likelihood function $P(B \mid A)$ for A given B by a factor containing the *a priori* probability of A namely $P(A)$ and the one of B namely $P(B)$according to

$$P(A \mid B) = \frac{P(B \mid A) \cdot P(A)}{P(B)}. \tag{5.16}$$

Let us now relate this description to the problem of orientation determination. The *a priori* probability $P(A)$ describes the probability of appearance of each orientation. As mentioned in section 5.1, these *a priori* probabilities follow a uniform distribution for azimuthal angles ϕ and a sinusoidal distribution for polar angles θ corresponding to the surface area element in polar coordinates for random orientations. For example, $P(A)$ reads $P(A(\phi = 40^\circ)) = 1/90$ for the distribution of the azimuthal angles using increments of one degree. The second *a priori* probabiltiy $P(B)$ acts as a normalizing constant and can be determined using the MC-simulations. Here, $P(B)$ is the sum of the probabilities (as for example shown in figure 5.7 **d)**) of detecting a fixed orientation χ for each possible initial orientation. The likelihood function $P(B \mid A)$ is determined by the probability of re-calculating χ_{re} by using χ as the initial orientation for the MC-simulation. Now, $P(B \mid A)$ can be calculated for each detected orientation. Superimposing the calculations of $P(B \mid A)$ for different detected orientations will lead to a propability distribution, giving the possibility to calculate the initial orientation out of some detected orientations. Note that in many systems of interest $P(A)$ is precisely not fully randomly distributed.

The last point in this section adresses the influence of the isotropic background on the re-calculation of a given orientation. Again, only the influence on the re-calculation of the θ-values was studied. Whereas the number of detected photons per bin was fixed to $I_{No} = 400$ photons, the composition of this number was changed during simulation. At the beginning, all photons per bin were attributed to the fluorescent molecule of interest. Then, using stepwidths of 10%, a given percentage of photons per bin was attributed to isotropic background fluorescence. For example, by using a noise level of 10%, 360 photons are attributed to the fluorophore and 40 photons to background noise. As shown in figure 5.11 **a)**, the noise level was varied between 0% and 100%. Under experimental conditions, a noise level of less than 10% can be achieved in many cases. With this level, the re-calculated values are close to the initial ones. If the noise level is further increased, the distribution of photons into the three detectors will be dominated by the background photons. Thereby, the initial orientation can not be re-calculated and leads in any case to $\theta \simeq 60^\circ$ as discussed in section 5.1.

The standard deviation of the re-calculated θ-values is shown in figure 5.11 **b)**. The standard deviation is almost constant with an increasing level of noise and can not be used as an additional criterion to distinguish between a low or a high level of noise. In conclusion, Monte-Carlo simulations of the orientation determination offer an important tool to explore the possibilities and the limits of the proposed detection scheme. It was shown that, depending on the desired accuracy, a high time resolution can be obtained. However, the method is limited by the shot-noise nature of dipole emisson. Especially dipole orientations close to $\theta(\phi) = 0^\circ$ or $\theta(\phi) = 90^\circ$ cannot be determined with high accuracy. Moreover, it should be mentioned

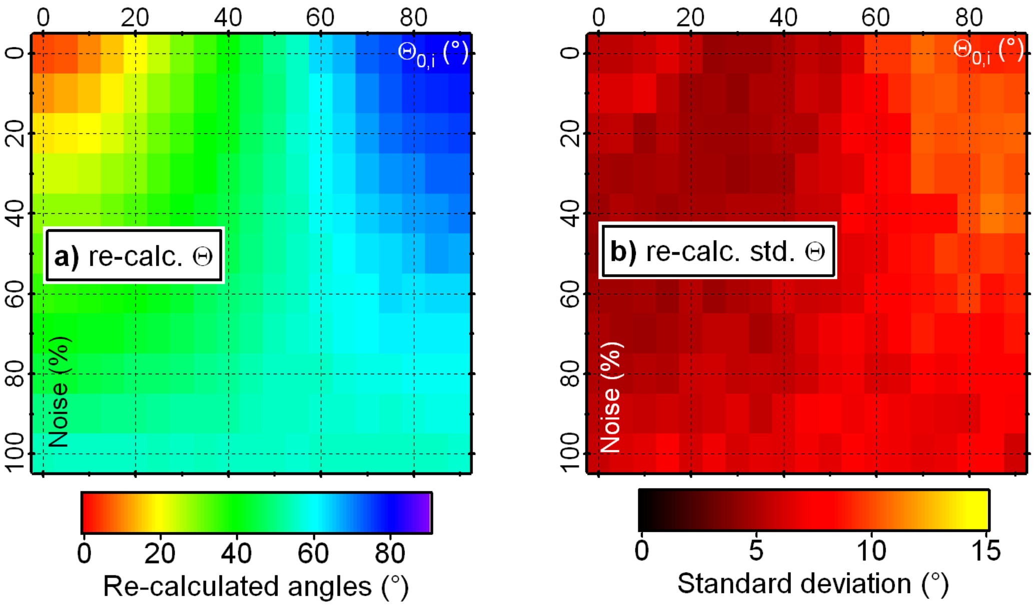

Figure 5.11: Simulations of **type C** for three-dimensional orientation determination. **a)** the re-calculated values of θ and **b)** the corresponding standard deviations are plotted as a function of the initial orientation $\theta_{0,i}$. The number of detected photons per bin was fixed to $I_{No} = 400$. The left axis shows the percentage of detected photons which are caused by isotropic background intensity. Ill-defined intensity ratios were converted to valid ones.

that the simulations neglect the non-ideal nature of the optical components. For example, the annular mirror may cause deflections of the center beam, the polarizing beam splitter is not perfect, and in general, the alignment of the setup is a bit challenging. These considerations have to be taken into account for the experimental section and require a proper correction.

5.3 Experimental results

Fluorescent latex beads

As discussed above, the alignment and correction procedures for three-dimensional orientation of the emission dipole are far from being trivial. In order to develop an appropriate correction, fluorescent latex beads (diameter 100 nm, Sigma-Aldrich) were used, which were immobilized on the cover glass surface by drying an aequos corresponding suspension of the beads. The concentration of the beads was chosen in such a way that after immobilization the mean inter-bead distance was large enough to clearly separate single beads with the confocal microscope. For these experiments, a water-immersion objective was used, featuring a beam diameter of 7 mm in the path of detection. A home-made mirror with an elliptical aperture was used to separate the inner detection beam from the outer beam. The diameter of the inner beam that could pass the mirror was about 3 mm. The overall detection angle of the water-immersion objective is given by its numerical aperture $NA = 1.2$, which results in a detection angle of $\alpha_r = 64°$ in water assuming an refractive index of $n = 1.33$. Geometrical considerations show that (taking the radii of the inner and the outer beam of 3.5 mm and 1.5 mm, respectively)

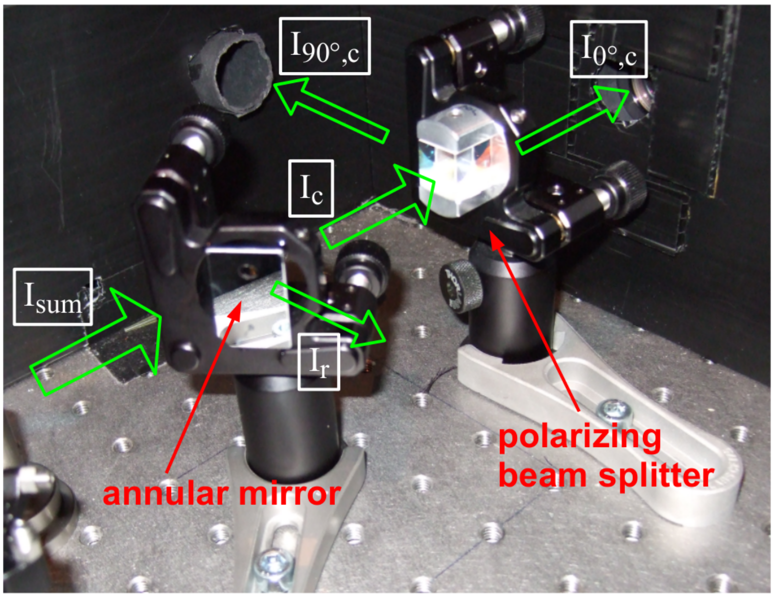

Figure 5.12: Experimental realization of the detection scheme for determining the three-dimensional orientation of emission dipoles. The incomming fluorescent light is at first separated by an annular mirror and at second by an polarizing beam splitter.

$$\frac{3.5\text{mm}}{\tan 64^\circ} = \frac{1.5\text{mm}}{\tan \alpha_{c,1}} \tag{5.17}$$

results in $\alpha_{c,1} = 41^\circ$, which is close to the ideal angle of $\alpha_{c,0} = 44^\circ$ theoretically derived in section 5.1. A polarization beam splitter was used for further separation of the inner detection beam. The experimental realization of the proposed detection scheme is shown in figure 5.12. To match the requirements of the water-immersion objective, the beads were covered with water. No desorption of latex beads was detected. The beads were excited with circulary polarized light with an intensity of 10 nW generated by a laser operating at 488 nm. Behind the dicroic mirror, a 500 nm long pass filter was used to filter out the remaining laser light. An area of 5 µm by 5 µm was raster-scanned using the piezo-driven scanning stage with a resolution of 128 by 128 pixel with an integration time of 2 ms per pixel. Three intensity images were obtained (data not shown, see section 5.2 for comparison) for each scan representing $I_{0,c}$, $I_{90.c}$ and I_r, which were used to calculate pixel by pixel the θ- and ϕ-values according to the equations 5.9 and 5.8. Figure 5.13 **a)** and **b)** show the corresponding values of θ and ϕ after applying an intensity threshold of 50 photons per pixel and appropriate correction. Each fluorescent latex bead contains a large number of randomly orientated fluorophores. In this case, as discussed in section 5.1, the expected average orientation values are known and can be used for correction as follows. To correct for the calculation of ϕ, the weighting of photons detected in one of the two detection channels for I_c ($I_{0,c}$ and $I_{90,c}$) can be changed in such a way that the histogram of ϕ-values shown in figure 5.13 **d)** is centered at $\phi_{avg} = 45^\circ \pm 4^\circ$. Here, the detected number of photons in the detector of $I_{90,c}$ was multiplied with 1.1 (in the following written as $I'_{90,c} = 1.1 \cdot I_{90,c}$) . To correct for the calculation of θ, a different approach was used. The ratio of the inner and the outer intensity (I_c and I_r) is determined by the diameter of the elliptical aperture of the mirror. Therefore, instead of weighting the number of detected photons, the

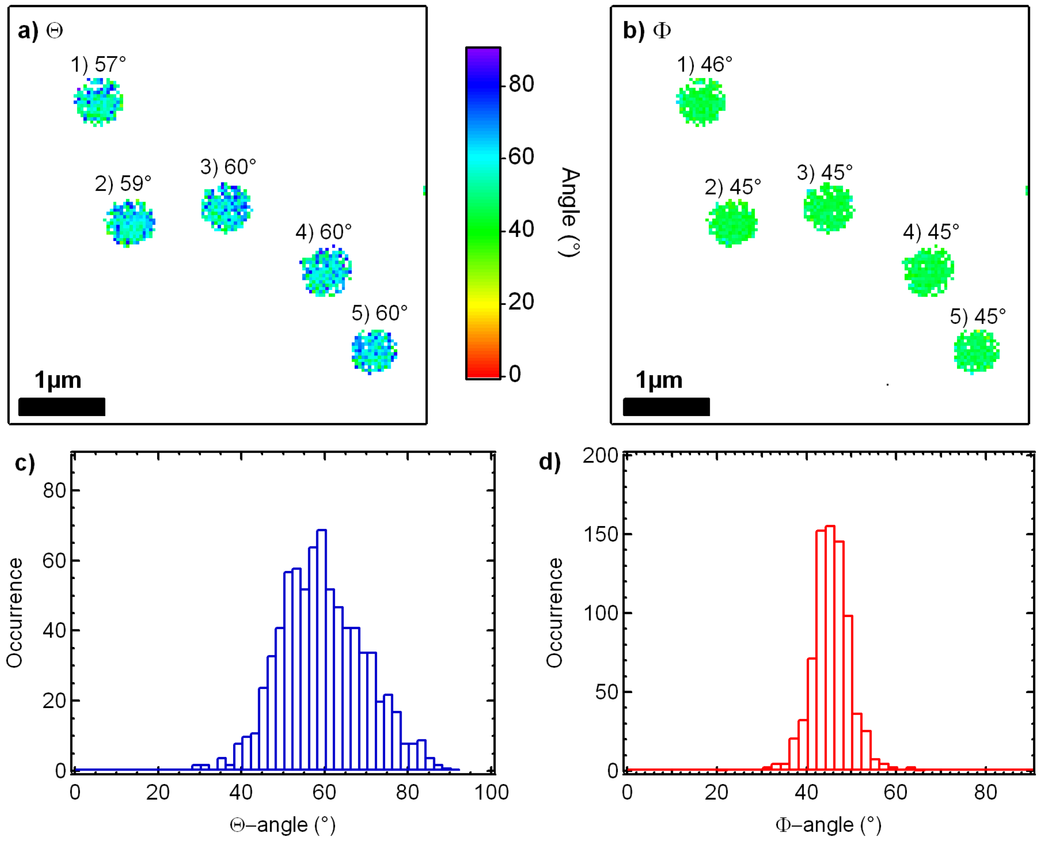

Figure 5.13: Calculated orientation patterns for five fluorescent latex beads immobilized on a cover glass surface. Three recorded intensity images (data not shown) were used for determination of **a)** θ-values and **b)** ϕ-values after applying a certain intensity threshold. The average angle of each single bead is appended. Histograms (pixel by pixel) of both images showing the appearance of **c)** θ-values and **d)** ϕ-values.

cutoff angle α_c, which is used for the calculations, was set to $\alpha_c = 41°$ so that the average θ-value of the histogram is $\theta_{avg} = 59° \pm 10°$. Using this approach, the initial calculated center angle $\alpha_{c,1} = 41°$ was verified. According to the relationship of the three detetctable intensities, correcting the θ-value will effect the ϕ-value and vice versa so careful tuning is necessary. By setting the (sum-)intensity threshold for the calculation of the orientation to 50 photons, the calculated patterns in figure 5.13 **a)** and **b)** do not show fringes with different color coding than the center of each bead as shown in figure 5.5. This indicates that the threshold value is sufficient to suppress the influence of the background luminescence and the shot-noise. Moreover, even if the detected intensity per pixel is increasing from the rim to the center of each bead, no further enhancement of the accurracy of the calculation according to the expected values is visible.

In order to evaluate the behavior of a single bead, the focus was placed in the center of the first bead (as indicated in figure 5.13). Time traces of the three detectable intensities were recorded for several seconds with a time resolution of 100 µs. The recorded time traces were further binned to a time resolution of 1 ms. The overall count rate was around 150 kHz, so each bin contained about 150 photons, distributed among the three detection channels. The calculation of the orientation was performed using the corrections determined above ($\alpha_c = 41°$ and $I'_{90,c} = 1.1 \cdot I_{90,c}$). Figure 5.14 **a)** and **c)** shows sections of the complete calculated θ- and ϕ-

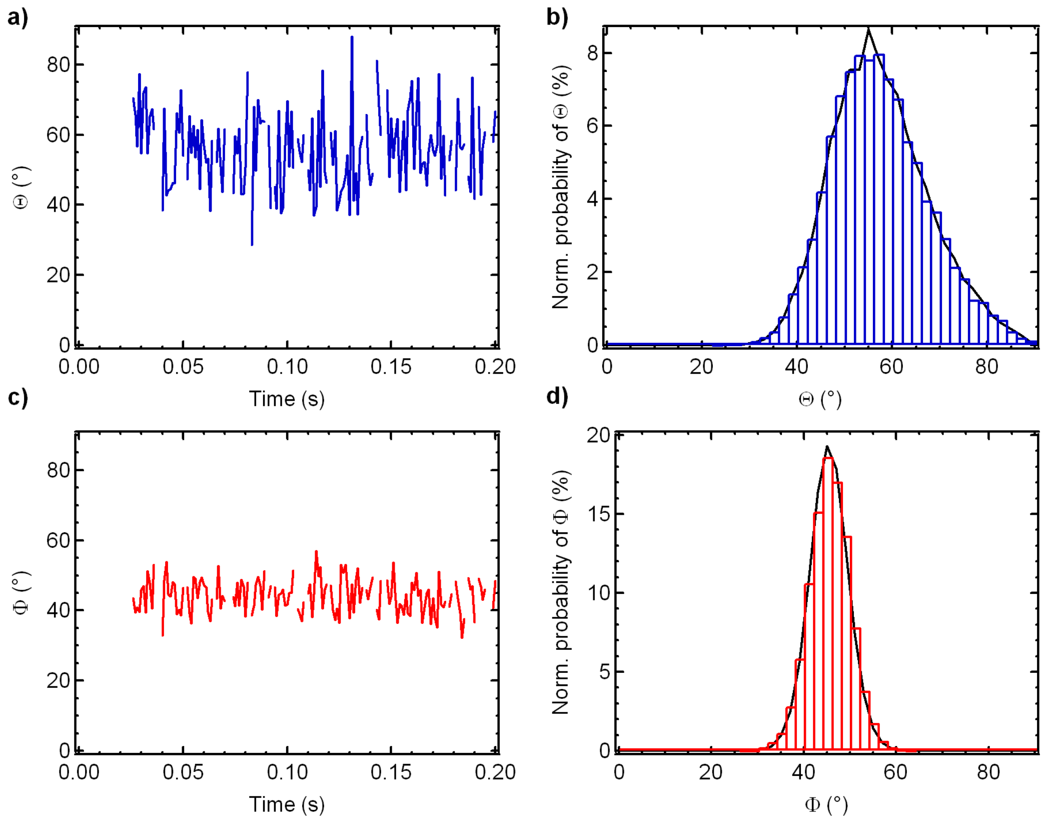

Figure 5.14: Calculated orientation time-traces of a single bead immobilized on a cover glass. The shutter of the laser opened 25 ms after starting the recording. The binwidth of the detected intensity traces was set to 1 ms. **a)** calculated θ-values as a function of time (small cutout of the whole trace), **b)** corresponding histogram (normalized) of calculated θ-values. The solid black line represents a histogram obtained from MC-simulation using the values determined by the experiment as initial seeds. **c+d)** orientation time-traces and corresponding histogram for ϕ-values.

traces as a function of time. Note that the laser shutter opened 25 ms after starting the recording and that the traces are interrupted. These voids correspond to ill-defined intensity ratios that do not allow attributing angles to these ratios, as discussed in section 5.2. The average θ- and ϕ-values were determined to $\theta = 57° \pm 10°$ and $\phi = 45° \pm 4°$ respectively. These values are in perfect agreement with the values determined by averaging over the single bead as shown in figure 5.13. The normalized histograms of the calculated θ and ϕ-values are shown in figure 5.14 **b)** and **d)** with a scalewidth of 2°. The histograms are rather smooth. In addition to the histogram of the calculated experimental data, a black line in both figures represents the normalized histogram of re-calculated θ- or ϕ-values obtained from MC-simulations using $\theta_0 = 57°$ and $\phi_0 = 45°$ as initial values. Additionally, α_c was set to 41° and each bin with a width of 1 ms was calculated using $I_{tot} = 750$ photons per bin. Taking into account that, according to figure 5.4, only around 20% of the overall number of emitted photons can be detected, this corresponds to the number of 150 photons per bin as detected in the experimental case. No further background was added. The normalized histograms of the experimental data coincide almost perfectly with those obtained by MC-simulations, because the applied model for calculation is the same in both cases. This is indicative of proper alignment and correction for the experimental data. However, this coincidence leads to additional conclusions. According to the literature, the emission dipole of a fluorophore placed directly at the interface of two media with different refractive indeces (here: water and glass), exhibits a significantly modified emission profile as compared to a dipole in a homogeneous medium [22]. Nevertheless, at least after applying the correction, the simplified model of the undistorted emission dipole allows recovering the theroretical predicted orientation ($\theta = 60^\circ$ and $\phi = 45^\circ$ for a superposition of a large number of fluorophores as it is the case for a fluorescent latex bead) with high accuracy, indicating that most of the fluorophores in the latex bead are sufficently far away from the interface. Moreover, the coincidence, even without applying background luminescence to the simulated data, evidences the very high obtainable signal-to-noise ratio.

Perylene monoimide

Even if some of the characteristics of the proposed method for orientation determination can be determined using fluorescent latex beads, the real challenge is the determination of the orientation of the emission dipole of a single fluorophore. For this purpose, different samples were prepared by spin-casting a polymer film from a co-solution of poly(methyl-methacrylate) (PMMA) and perylene monoimide (PMI) in toluene onto a microscope cover slip. The ratio of PMMA/toluene was 5 g/l. The resulting approximately 50 nm-thick polymer film contains the PMI chromophores in arbitrary orientations. Circularly polarized light with a power of 5 µW was used for excitation, and the sample was covered by immersion oil to fulfill the requirement of a homogeneous refractive index in the vicinity of the dipole using an oil-immersion objective for excitation/detection. An area of 5 µm by 5 µm was raster-scanned (128 by 128 pixels) with a dwell time of 2 ms. Figure 5.15 **a-d)** shows the three detected intensities $I_{0,c}$, $I_{90,c}$ and I_r and their caluclated sum (I_{sum}) thus obtained. A comparison of individual spots in figure 5.15 **a)** and figure 5.15 **b)** reveals differences in the measured intensities, which can be directly attributed to different azimuthal angles. As described in the previous section, careful corrections are neccessary for calculating the orientation patterns. Here, an oil-immersion objective ($NA = 1.4$,100x magnification) was used for the experiments with PMI. In contrast to the water-immersion objective, the oil-immersion objective features a smaller detectable beam diameter of around 5 mm and an detection angle of $\alpha_r = 67^\circ$. Using the mirror with an ellipsoidal aperture projected as a circle 3 mm in diameter leads to $\alpha_c = 55^\circ$. Nevertheless, corrections using immobilized latex beads (data not shown) revealed that the effective cut-out angle is $\alpha_c = 41^\circ$. This relatively large discrepancy can be explained by the small beam diameter caused by the pupil of the oil immersion objective in conjunction with the suboptimal quality of the annular mirror (see figure 5.12). Potential improvements will be discussed in section 6. The detected number of photons in the detector of $I_{90,c}$ had to be multiplied with 1.15.

Applying these correction factors obtained from images of fluorescent latex beads in a first approximation, the scanned images of PMI can be used to refine the correction factors as long as some assumptions are fulfilled. If a sufficiently large number of molecules is imaged, and a random orientation of the molecules is assumed, the expected averaged orientation will be again $\theta_{avg} = 60^\circ$ and $\phi_{avg} = 45^\circ$. Based on these considerations, $\alpha_c = 43^\circ$ and $I'_{90,c} = 1.2 \cdot I_{90,c}$ were derived. The orientation was calcluated for each pixel above a fluorescence intensity threshold of 40 photons. Figure 5.15 **e+f)** shows the calculated θ- and ϕ- pattern. Note that

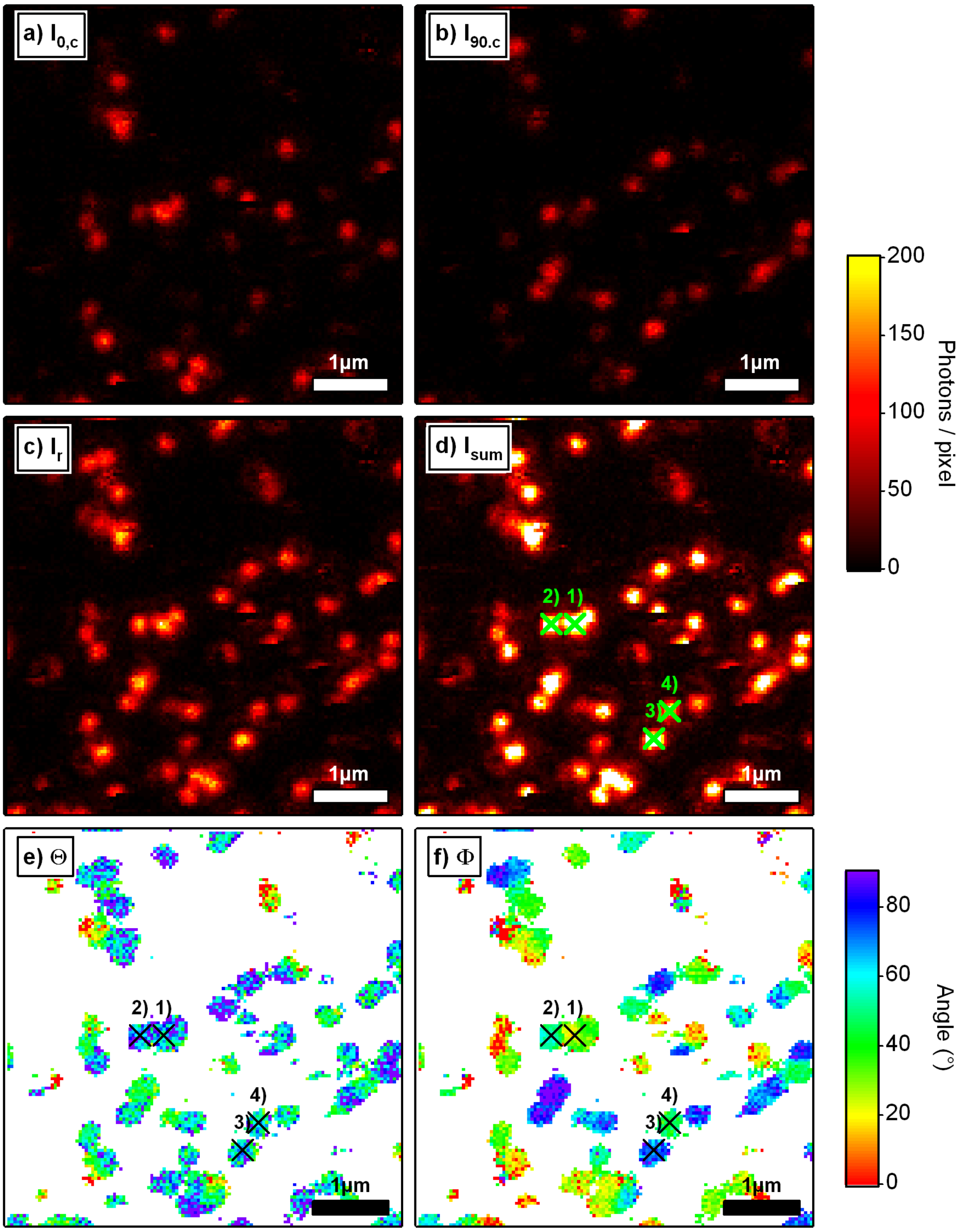

Figure 5.15: Single Perylenediimide molecules dispersed in a PMMA film. **a-d)** $I_{0,c}$, $I_{90,c}$ and I_r show the pseudo color-coded, detected fluorescence intensity obtained by scanning the sample. I_{sum} represents the sum of the previous intensities. **e+f)** after setting an appropriate threshold, the intensities were used to calculate the orientation patterns θ and ϕ pixel by pixel. Additionally, four molecules were selected for further recording of stationary time traces as indicated in **d)**, **e)**, and **f)**.

non-valid ratios were converted to the closest valid ratios. The different colors of the various spots representing single dye molecules reflect their arbitrary orientations. The colors of the pixels in individual spots vary due to shot noise. The low incidence of spots with a low θ, representing molecules oriented close to the optical axis, can be understood keeping in mind that the surface area element in polar coordinates scales with the sine of the polar angle. Com-

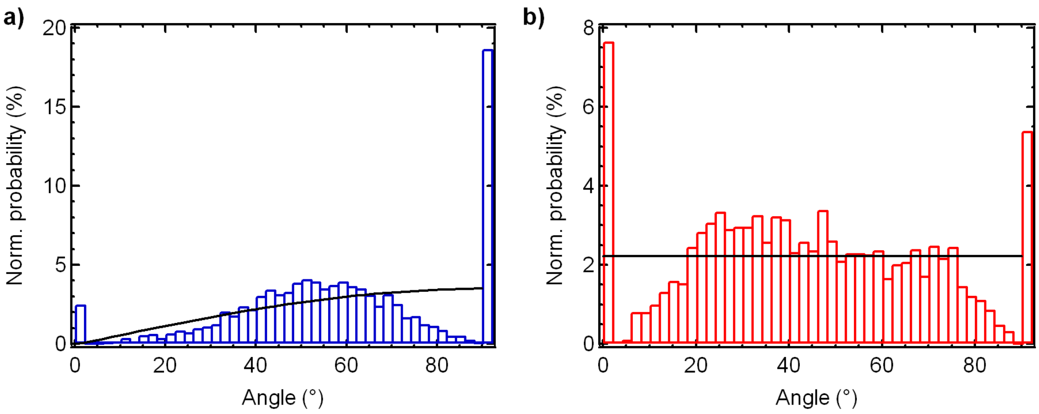

Figure 5.16: Normalized histograms of the calculated angles **a)** θ (blue) and **b)** ϕ (red). The pixel by pixel histograms were calculated using figure 5.15 **e+f)**. The solid black lines represent the expected probality distributions of θ- and ϕ- values, assuming a sinusoidal distribution of the polar angles θ and an equal distribution of the azimuthal angles ϕ.

paring the intensity image in figure 5.15 **d)** with the θ-pattern of figure 5.15 **e)** one notices that molecules oriented close to the optical axis show a rather weak fluorescence. This is because the component of the exciting electrical field in the focus parallel to the optical axis is small compared to the perpendicular component and hence, according to figure 5.4 **b)**, the detectable emission intensity is smaller than for large values of θ.

The probability distributions of calculated θ- and ϕ-pixels are shown in figure 5.16. In addition, the theoretically expected distribution is plotted within the figures. The distributions resemble those features expected for arbitrarily oriented molecules: The azimuthal angle ϕ is evenly distributed, and the polar angle θ shows an approximately sinusoidal distribution. The lack of θ-angles around 75° to 85° can be attributed to shot noise, resulting in non-valid intensity ratios. As discussed above, these ratios were fixed to the next possible ones, resulting in apparent large number of pixels of $\theta = 90°$ and therefore depleting the distribution in the vicinity of the limiting values. The same argument holds for ϕ-values around $\phi \sim 0°$ and $\phi \sim 90°$.

The markers shown in figure 5.15 define the position of the focus for recording stationary, individual time traces of PMI molecules which are shown in figure 5.17 and 5.18. The time traces were used to study the dynamics of these molecules as a function of time. Orientation traces were calculated from the recorded time traces, using the same correction factors as for the scanning images in figure 5.15 and applying a threshold criterion of 40 photons per bin. In order to avoid the rapid bleaching of the molecules, the laser power was decreased to 1 µW. The obtainable time resolution is mainly limited by the decreased count rate and was fixed to 5 ms for each time trace. The recording of the intensity time traces started shortly before opening the shutter for the laser light. For this reason, all measurements starting at time zero show an increase in intensity at the beginning.

Figure 5.17 **1)** shows a time trace where the mean intensity drops after 32 s by a factor of two. The common explanation of such a behaviour is that initially two molecules are within the excitation/detection focus, one of which bleaches after a certain time, whereas the other remains in an active state. Here, the calculated orientations are plotted as dots. The advantage

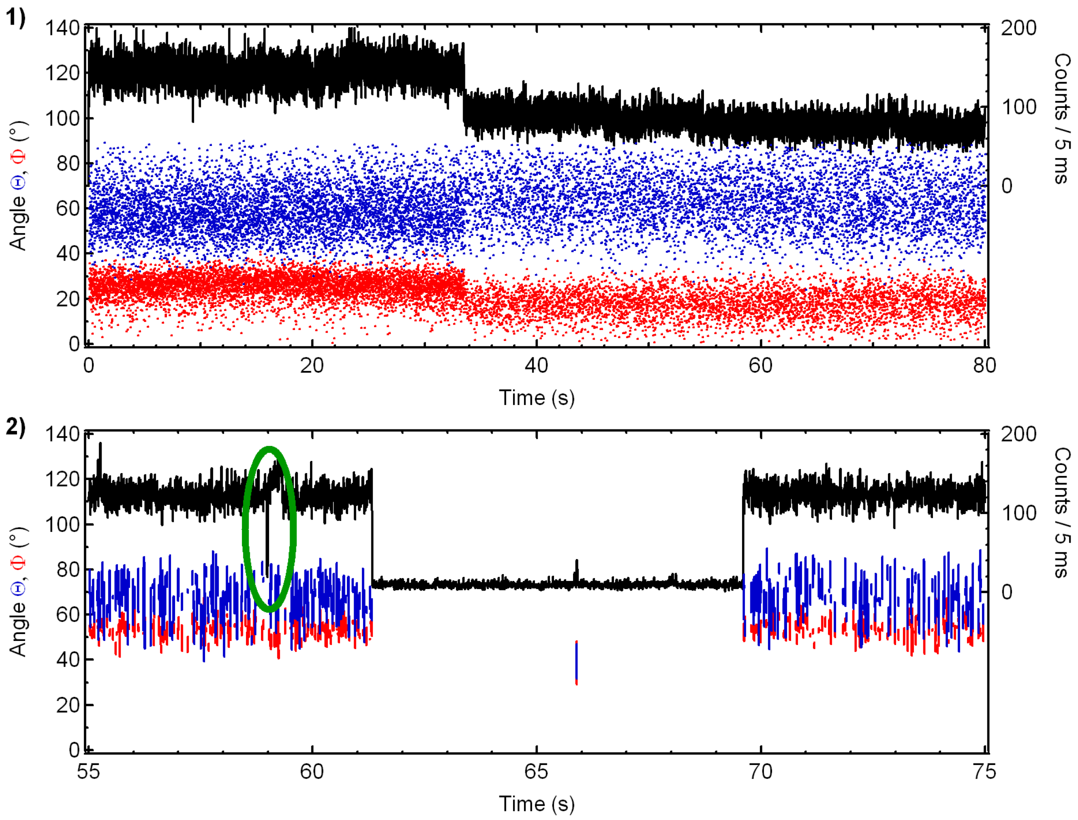

Figure 5.17: part 1: Stationary time traces of two selected positions in figure 5.15. The black lines (right axes) represent the overall number of photons detected per 5 ms. The blue lines (blue dots in panel 1) show the calculated θ-values, the red lines (red dots in panel 1) the ϕ-values for each bin with valid intensity ratios. The green ellipse highlights a special feature.

of this method is that the density of dots represents some kind of histogram as a function of time. If the time range with one active molecule is compared with the time range with two active molecules, a superposition of two molecules is clearly visible for the orientation time traces. The bleached molecule had a smaller θ-value and a larger ϕ-value than the remaining one. Moreover, a very slow decrease in the overall intensity can be detected for the remaining molecule but no visible change in the orientation occurs. This can be attributed to either a movement of the laser focus away from the moelcule or, but less likely, by a slow rotational motion of the molecule in the PMMA matrix.

Figure 5.17 **2)** shows a common feature of single fluorescent molecules namely blinking (for the blinking behavior of eGFP see, for example, references [39, 14], for PMI reference [37]). Fluorescent molecules can populate so called ”dark-states”, in which they are temporary not fluorescent. The case shown here is unlikely in the way that the lifetime of the dark state is quite long (around 8 s). Often, as indicated by the green ellipse, the apparent lifetime of the dark state is much shorter. As expected, the calculated orientation remains unchanged even after the dark state. The short interuption of the dark-state (at around 66 s) is impossible to interpret. It could originate from a very short-lived fluorescent state or just from a fluctuation in the background intensity. Figure 5.18 **3)** shows a superposition of up to three molecules at the same place. The intensity time trace starts at a certain intensity level of around 350 photons per bin. After 1 s, the intensity increases to around 450 photons per bin and decreases suddenly to 200 photons per bin

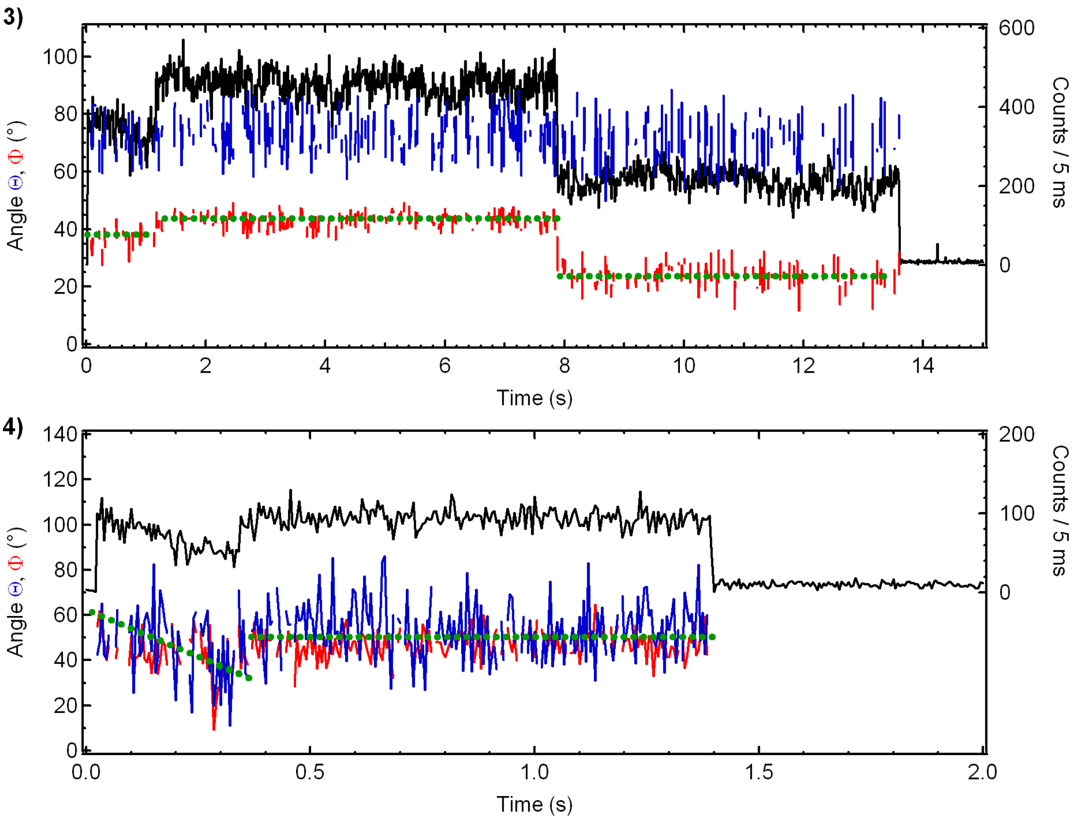

Figure 5.18: part 2: Stationary time traces of two selected positions according to figure 5.15. The black lines (right axes) represents the overall number of photons detected per 5 ms. The blue lines show the calculated θ-values, the red lines the ϕ-values for each bin with valid intensity ratios. The green doted lines highlight special features.

until all molecules are bleached. Translating this behavior in a number of active (fluorescent) molecules, this would read 2-3-1. The surprising step is the bleaching (or transition into a dark state) of two molecules at the same time. The orientation trace shows that θ remains constant the whole time, whereas all intensity steps cause changes in the corresponding calculated ϕ-values.

Another set of traces is shown in figure 5.18 **4)**. Here, the initial intensity decreases continuously and jumps back to the initial level. This continuos decrease of the intensity comes along with a change in the orientation represented by θ and ϕ. As shown in figure 5.4, the detectable intensity is a function of θ. In fact, θ seems to decrease along with the intensity. This indicates that the molecule is changing its orientation within the PMMA matrix. Nevertheless, the fast jump to the initial intensity and orientation is again surprising and hard to explain. These examples show clearly that every single molecule has its own characteristics in terms of orientation, blinking behavior, survival time etc. These individual features are averaged in ensemble measurements.

Polydiacetylene nanowires in porous alumina

Polydiacetylene (PDA) is a polymer with very interesting features: it can undergo a sharp color transition triggered by various kinds of external stimuli, including thermal annealing, *pH* change, organic solvent exposure and mechanical stress [52, 9, 29]. PDA is obtained by photopolymerization or thermal polymerization of crystalline diacetylene and shows strong fluorescence [9]. The emission dipoles of the chromophores are uniformly oriented within crystalline grains. In addition, if molten diacetylene monomers were infiltrated into porous alumina templates, the confinement is expected to cause oriented crystallization of diacetylene, leading in turn to uniform crystal orientation in the polymerized PDA. Therefore, this modell system is promising to demonstrate that the determination of the orientation of emission dipoles can be used to study the internal morphology of nanoobjects.

Molten diacetylene monomers were infiltrated into porous alumina templates with a pore diameter of around 400 nm, followed by photo-polymerization with UV light. After UV-exposure, the color of PDA turns from colorless to blue. Further heating above 80°C causes a color shift from blue to red. It was found that the red nanowires exhibit strong red fluorescence when excited with laser light with a wavelength of 544 nm.

How to make use of the proposed detection sheme for the emission dipole of single molecules in order to check the crystalline texture of the PDA inside porous alumina? As discussed above, the simultaneous detection of a large number of randomly oriented emitters will lead to $\theta \sim 60^\circ$ and $\phi \sim 45^\circ$ as long as the correction is done carefully. Even without correction, color-coded orientation images show uniformly colored areas, as long as the orientation of the emission dipoles is random (see figure 5.13 for comparison). The question arises if the infiltrated PDA contains randomly oriented emitters within the excitation/detection focus. For experiments with PDA-infiltrated porous alumina, the same experimental conditions were used as described in the previous subsection for the study of embedded PMI molecules. However, thanks to the bright fluorescence of PDA, the exciting laser intensity could be decreased to 8 nW. The aluminum substrate was removed from the porous alumina membrane by a selective wet-chemical etching step and the infiltrated alumina membrane was attached to the cover glass slide using immersion oil. Here, the requirement of a homogenous surrounding is not fulfilled if the focus is placed at the oil/membrane interface, because the refractive indices of both materials differ. Therefore, an adequate correction is almost impossible. Also, the interface might distort the emitted beam of light. For correcting the images, α_c was, more or less arbitrary, fixed to $\alpha_c = 48^\circ$, and the correction for the porization was chosen as $I'_{90,c} = 1.3 \cdot I_{90,c}$. The threshold for calculating the orientations was set to 220 photons per pixel. Figure 5.19 **a+b)** shows the pseudo-color coded accumulated intensity of PDA-infiltrated porous alumina. The three detected intensities $I_{0,c}$, $I_{90,c}$ and I_r were used to calculate I_{sum}. Whereas figure 5.19 **a)** represents a scanned area of 10 µm by 10 µm, the scanned area of figure 5.19 **b)** is 5 µm by 5 µm. Single infiltrated pores can be optically resolved using standard confocal optical microscopy. In figure 5.19 **a)**, the hexagonal ordering of the infiltrated PDA indicating the positions of the pores can be seen quite well. Note that the pores are attached to the cover glass with the closed side of the membrane. Therefore, if the polymer does not perfectly infiltrate a single pore, the luminescence might be much weaker than in the case of a completely filled pore. The three intensity images belonging to figure 5.19 **b)** were used to calculate the orientation patterns of θ and ϕ, as shown in figure 5.19 **c+d).** Surprisingly, the different areas corresponding to single pores do not have the same color, as one would expect for a large number of random emitters within the focus (see figure 5.13 for comparison). Nevertheless,

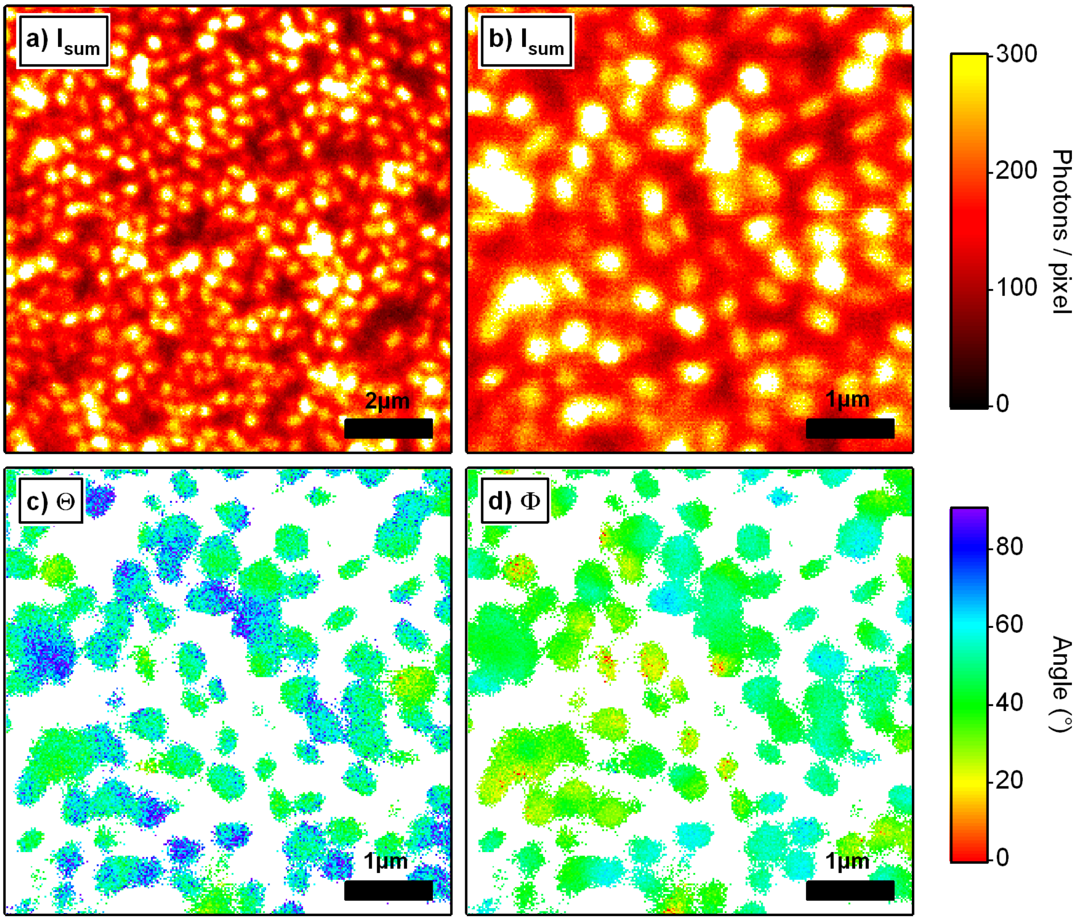

Figure 5.19: Polydiacetylene infiltrated porous alumina. **a)** I_{sum} represents the pseudo color-coded sum of the three detected intensities namely $I_{0,c}$, $I_{90,c}$ and I_r raster scanned over an area of 10 µm by 10 µm and **b)** over an area of 5 µm by 5 µm. **c+d)** after setting an appropriate threshold, the intensities behind **b)** were used to calculate the orientation patterns of θ and ϕ pixel by pixel.

the calculated color range is not broad. To check the distribution of angles in more detail, each pattern was histogrammed pixel by pixel. The distributions of θ-values and ϕ-values are shown in figure 5.20 **a+b)**. Both distributions do not follow the expected distributions of randomly oriented emitters for which one would expect a sinusoidal distribution of θ-values and equal distributions of ϕ-values. Especially the distribution of the ϕ-values is much broader than in the case of an averaged emitter like the fluorescent latex bead in figure 5.14. However, the single spots corresponding to one PDA-nanowire are uniformly colored. Following the results, the polymerized PDA in a single pore is acting as a single emitter with a defined orientation of the emission dipoles and not as an averaged emitter consisting of a large number of randomly oriented emitters. Apparently, there are preferred orientations of the emitters in one pore. Additionally, it might be the case that this preferred orientation is a composition of a certain number of orientations. However, complete randomness would result in patterns much more unifom like those observed for fluorescent latex beads (figure 5.13). As a next step, it would be interesting to record intensity time traces of individual pores and to compare the histograms of the obtained orientations with the simulated ones.

It has to be considered that the infiltrated alumina membrane has a periodic structure close to

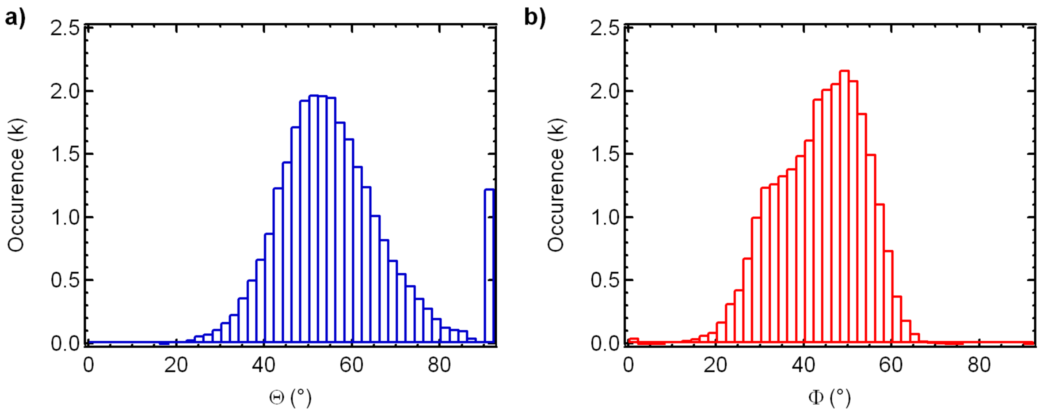

Figure 5.20: Histograms of **a)** the calculated θ- pattern (blue) and **b)** the calculated ϕ- pattern (red) of figure 5.19 **c+d)** representing the angular distributions averaged over an ensemble of pores, each of which in turn represents an ensemble of emitters.

the wavelength of the emitted light, which might lead to further distortions. It might be helpful for future experiments to remove the cone-shaped pore bottoms of the alumina membrane and to record images in different depths of the PDA infiltrated membrane.

In conclusion, resolving the orientation of fluorescent polymers confined in nanoporous alumina offers a new possibility to determine textures of embedded fluorescent materials and probing ensembles of nanoobjects while resolving single nanoobjects simultaneously. This approach can also be applied to materials under shear stress or to drawn materials to probe their degree of anisotropy.

5.4 Discussion

The proposed method for orientation determination of the emission dipole of single fluorescent molecules, fluorescent latex beads or ensembles of fluorescent nanoobjects does not aim at determining the orientation with high accuracy. However, the main advantage is the obtainable time resolution. The presented scheme uses every single photon for the orientation determination, whereas the detection scheme proposed by Fourkas [26] rejects photons by using three different polarizations for detection. In comparison to CCD-chip based imaging techniques, as for example shown in reference [7], the proposed detection sheme has a number of advantages. For CCD-based imaging techniques the obtainable time resolution is limited by the frame rate of the camera (in the millisecond range). Furthermore, the photons from a molecule have to be distributed over a number of pixels reducing the signal-to-background ratio significantly. Finally, time-consuming fitting procedures have to be applied to the recorded images in order to obtain the orientation making a real-time determination impossible.

The method proposed in this work is straightforward. The time resolution is mainly limited by the countrate of the probe of interest. Using fluorescent latex beads, a time resolution of 500 µs was achieved. For single fluorescent molecules (PMI) the time resolution had to be decreased to 5 ms. Here, the countrate was decreased to about 100 photons per 5 ms by using a lower excitation intensity to prevent the rapid bleaching of the dye. The calculated orientation can be used to study the local viscosity around the fluorescent probe as shown in section 5.3.

In addition, the determination of oriented ensembles of emitters in crystals of fluorescent materials allows for analyzing the texture of these materials. Even if the relation of the transition dipole and the texture is not known so far, the proposed method can potentially be used as a complementary approach with X-ray diffraction methods and polarized infrared-spectroscopy to elucidate the supramolecular structure in the material under investigation. Moreover, the orientation distribution of the emission dipoles can be quasi simultaneously detected for a large number of fluorescent entities with high spatial resolution.

Chapter 6

Conclusion and outlook

Three goals were aimed at with the experiments presented in this thesis: First, can nanoporous alumina be applied to single molecule fluorescence detection of probes under nanoscale confinement, second, are there benefits of this confinement with respect to single-molecule detection, and third, how does the confinement affect physical properties of a range of model systems. For this purpose, not only well-known concepts from the field of single molecule detection were applied, but a variety of new concepts and tools were developed.

Self-ordered nanoporous alumina was used to create a two-dimensional geometrical confinement for either single diffusing molecules or fluorescent polymerized nanowires. The membranes for measurements of single molecule diffusion featured a pore diameter of 35-40 nm, a porosity (volume fraction of the pores) of 20-25%, and a thickness of 35 µm. Thus, the aspect ratio of the pores is $\simeq$1000. In comparison, the size of the diffraction limited laser focus is roughly 2 µm in height (long axis) and 0.5 µm in diameter (short axes), resulting in an aspect ratio of 4. Therefore, if the long axis of the pores is aligned with the long axis of the confocal microscope, the probe molecules are forced to diffuse parallel to the long axis of the laser focus.

Apparent one-dimensional diffusion within nanoporous alumina was shown for different probes such as Alexa Fluor 488 and the enhanced green fluorescent protein (eGFP). As compared to three-dimensional diffusion in free solution, the mean diffusion time through the focus increases within the pores. The factor of increase was theoretically derived as the squared aspect ratio of the laser focus resulting in a value of 16. Indeed, for Alexa Fluor 488 an increase in the mean diffusion time by a factor of 19 was found. In the case of eGFP a factor of 14 was obtained. The excellent agreement with the theoretically proposed model leads to the conclusion that the diffusion coefficient remains constant within the pores. In contrast to methods proposed in literature [58], this method combines a prolonged diffusion time with a decreased detection volume by replacing 80% of the solution with the well-defined porous solid.

The dynamics of molecules on a timescale which coincides with the timescale of free diffusion in solution can now easily be separated in the auto-correlation function. As mentioned above, the auto-correlation function provides an access to the mean particle number within the focus. By using Alexa Fluor 488, which in contrast to eGFP has no tendency to stick to the pore walls at a *pH*-value of 7, the porosity of the membrane can be determined by comparing the mean particle number in solution and within the membrane. For eGFP, the ratio of freely diffusing and immobilized molecules was estimated to be almost one.

The detected decrease in the fluorescence lifetime within the membranes could be well described by the different environmental refractive index in porous alumina compared to water. Thus, the first evidence for successful probing of porous materials in terms of porosity, refractive index, and analyte to porewall interactions on a single molecule level was demonstrated.

Buffers with different pH-values were used to evaluate the adsorption of eGFP on the porewalls. It was shown that only between pH 8 and pH 11 a significant fraction of mobile molecules can be detected within the pores. Therefore, the permeabillity of the membrane could be controlled by changing the pH-value of the buffer solution. It is of great interest to determine the diffusive behavior of probes as a function of ionic strength and different buffers.

In order to develop a more robust strategy for the detection of single molecules diffusing through alumina nanopores, two objectives, namely a water-immersion objective and an oil-immersion objective, were compared. For studies with membranes having closed pore bottoms, the oil-immersion objective should be used (optionally combined with an increased porosity of the membrane in order to match the effective refractive index perfectly), whereas the water-immersion objective is the best choice for translocation studies and for direct comparison of measurements in solution and in confinement.

Monte-Carlo simulations were performed to evaluate the influence of the geometrical confinement on the diffusive behavior of single fluorescent molecules. A variety of parameters such as pore lengths, pore diameters, diffusion coefficients, and excitation/detection probabilities were accessible. It was shown that the simulations perfectly fit with the experimental results. The simulations were further expanded to allow calculating the diffusion of molecules containing two or more fluorophores for FRET studies. To this end, rate constants for conformational changes and resulting changes in the distance between the fluorophores were included. The simulations showed massively increased burst widths in the case of one-dimensional diffusion, which allows for precise FRET measurements within the membranes.

Nevertheless, the experimental realization is not trivial. Tentative experiments showed that FRET can be detected within nanoporous membrane. The obtainable information was mainly limited by the properties of the probe, namely the disadvantageous stoichiometry of the degree of labeling and the poor quantum yield of the acceptor. Moreover, it has to be checked for each labeled probe protein if the surface charges and other possible interactions with the pore wall allow free diffusion of the proteins within the membrane. In addition, for designing of new probe proteins, attention should be paid to the acceptor dye. Acceptor dyes, which can be directly excited using pulsed lasers, pave the way for new strategies for the evaluation of FRET data [51]. Another important point to consider for future experiments is the modification of the pore walls. Even if the initial coating with BSA prevents the adsorption of the probe molecules at least partially, the complete prevention of adsorption is crucial to diffusion experiments, as discussed in section 4.1.

By addressing all these points, the most interesting feature of nanoporous alumina can be exploited: the pores are highly parallel. Even if other matrices, as for example solid state nanopores [13] or zero mode waveguides [59], show tiny holes, there is no other method available for the production of nanopores with such a high aspect ratio, and with a pore density of 10^9 pores per square centimeter. Combination of self-ordered alumina membranes with lithographic methods, for example, by covering the whole membrane surface with a polymer and using electron beam lithography to thrill small holes into the polymer with distances in the micrometer range might yield to single pores within the detection focus. This would be the ultimate goal for high concentration measurements (see section 2.7) with long detection times of freely diffusing molecules.

The second major topic of this thesis was the three-dimensional orientation determination of the emission dipole of single molecules with the perspective of studying the confinement effects on rotational anisotropy. A new detection scheme was proposed, which allows a shot-noise-limited orientation determination. This method uses a sophisticated distribution of the detected fluorescence into a set of three detectors. In fact, as shown by various simulations and experiments, several hundreds of detected photons are sufficient to determine the orientation with appropriate accuracy. Thus, the time resolution of the orientation determination is only limited by the count rate of the fluorophores. For fluorescent latex beads, which feature a large number of fluorophores, a time resolution down to 500 µs was shown for orientation determination, making this detection scheme in principle fast enough to detect changes in the orientation of macromolecules. Moreover, the detected intensity can be directly used to calculate the orientation and no time-consuming fitting procedures are neccessary, as it is the case for most methods proposed in literature [7].

In addition, the orientation-resolved study of fluorescent probes confined to nanoporous alumina might provide new insights in the impact of geometric constrains and interfacial interactions on the internal dynamics of macromolecules. Therefore, the detection scheme was used for probing the texture of fluorescent polymer rods embedded in nanoporous alumina with original pore diameters of 400 nm. Whereas the averaging about a large number of randomly oriented fluorophores will lead to a magic angle detection, the polymer rods showed different but uniform orientations. Even if the overall distribution of orientations was very narrow, the confinement by the pores leads to different preferred orientations within the single pores. Thus, the method of orientation determination can be potentially used in conjunction with X-ray diffraction methods and polarized infrared-spectroscopy for texture analysis of fluorescent materials. In future experiments the rotation of fluorescent probes embedded in confined materials could be studied with high time resolution.

As discussed in section 5.3, the accuracy of the method is limited by the annular mirror, which is used to separate the fluorescent light. To improve the accuracy, a telecentric lens system could be used to broaden the beam behind the pupil of the objective, which is normally limiting the diameter of the detectable beam. By broadening the beam, effects related to the small hole in the mirror would become less relevant and the adjustment would be simplified. Moreover, by using a telecentric lens system in conjunction with epi-fluorescence microscopy, the method of orientation determination could be parallelized. Instead of raster-scanning a sample, images could be taken at one shot using CCD-based detection. Therefore, the annular mirror has to be placed in a conjugate image plane to separate the light emitted into the rim of the objective from the light emitted to the center. If the three obtainable images are mapped into one CCD-detector, the dipole orientation of several molecules can be determined at the same time only limited by the time-resolution of the camera.

Another perspective is the idea of super-resolution beyond the diffraction barrier of an optical microscope [40]. The orientation-resolved measurements reveal information which is not accessable by conventional experimental designs. In conventional confocal microscopy, the diffraction limit is given by the size of the focus and the question of separability in the intensity patterns of adjacent molecules. In the case of adjacent molecules, the orientation patterns can be used to filter the intensity patterns. This could be done by plotting, for example, only the intensity pattern which corresponds to a given dipole orientation.

In conclusion, this work is focused on the development of new tools and concepts in optical confocal microscopy and single molecule detection in tight interplay with materials science. These methods show a high potential and can be easily applied to a wide range of scientific areas.

Bibliography

[1] D. Axelrod. Carbocyanine dye orientation in red-cell membrane studied by microscopic fluorescence polarization. *Biophys. J.*, 26:557–573, 1979.

[2] A. P. Bartko and R. M. Dickson. Imaging three-dimensional single molecule orientations. *J. Phys. Chem. B*, 103:11237–11241, 1999.

[3] T. Bayes. An essay towards solving a problem in the doctrine of chances. *Philos. Trans.*, 53:270–418, 1763.

[4] A. Benda, M. Hof, M. Wahl, M. Patting, R. Erdmann, and P. Kapusta. TCSPC upgrade of a confocal FCS microscope. *Rev. Sci. Instrum.*, 76:033106 (1–4), 2005.

[5] E. Betzig and R. J. Chichester. Single molecules observed by near-field scanning optical microscopy. *Science*, 262:1422–1425, 1993.

[6] K. Brejc, T. K. Ixma, P. A. Kitts, S. R. Kain, R. Y. Tsien, Ormö M., and J. S. Remingtion. Structural basis for dual excitation and photoisomerization of the Aequorea Victoria green fluorescent protein. *Proc. Natl. Acad. Sci. USA*, 94:2306–2311, 1997.

[7] M. Böhmer and J. Enderlein. Orientation imaging of single molecules by wide-field epifluorescence microscopy. *J. Opt. Soc. Am. B: Opt. Phys*, 20:554–559, 2003.

[8] M. Böhmer, M. Wahl, H. J. Rahn, R. Erdmann, and J. Enderlein. Time-resolved fluorescence correlation spectroscopy. *Chem. Phys. Lett.*, 353:439–445, 2002.

[9] S. K. Chae, H. Park, J. Yoon, C. H. Lee, D. J. Ahn, and J.-M. Kim. Polydiacetylene supramolecules in electrospun microfibers: Fabrication, micropatterning, and sensor applications. *Adv. Mat.*, 19:521–524, 2007.

[10] A. H. A. Clayton, Q. S. Hanley, D. J. Arndt-Jovin, V. Subramaniam, and T. M. Jovin. Dynamic fluorescence anisotropy imaging microscopy in the frequency domain (rFLIM). *Biophys. J.*, 83:1631–1649, 2002.

[11] B. P. Cormack, R. H. Valdivia, and S. Falkow. FACS-optimized mutants of the green flourescent protein (GFP). *Gene*, 173:33–38, 1996.

[12] A. Debarre, R. Jaffiol, C. Julien, D. Nutarelli, A. Richard, P. Tchenio, F. Chaput, and J. P. Boilot. Quantitative determination of the 3D dipole orientation of single molecules. *Europhys. J. D*, 28:67–77, 2004.

[13] C. Dekker. Solid-state nanopores. *Nat Nano*, advanced online publication:–, March 2007.

[14] R. M. Dickson, A. B. Cubitt, R. Y. Tsien, and Moerner W. E. On/Off blinking and switching behaviour of single molecules of green fluorescent protein. *Nature*, 388:355–359, 1997.

[15] K. Dörre, J. Stephan, and M. Eigen. Highly efficient single molecule detection in different micro and submicrometer channels with cw-excitation. *Single Molecules*, 2:165–175, 2001.

[16] L. Edman, U. Mets, and R. Rigler. Conformational transitions monitored for single molecules in solution. *Proc. Natl. Acad. Sci. USA*, 93:6710–6715, 1996.

[17] C. Eggeling, S. Berger, L. Brand, J. R. Fries, J. Schaffer, A. Volkmer, and C. A. M. Seidel. Data registration and selective single-molecule analysis using multi-parameter fluorescence detection. *J. Biotech.*, 86:163–180, 2001.

[18] M. Eigen and R. Rigler. Sorting single molecules: Application to diagnostics and evolutionary biotechnology. *Proc. Natl. Acad. Sci. USA*, 91:5740–5747, 1994.

[19] E. L. Elson and D. Magde. Fluorescence correlation spectroscopy: 1. Conceptual basis and theory. *Biopolymers*, 13:1–27, 1974.

[20] S. A. Empedocles, R. Neuhauser, and M. G. Bawendi. Three-dimensional orientation measurements of symmetric single chromophores using polarization microscopy. *Nature*, 399:126–130, 1999.

[21] J. Enderlein and I. Gregor. Using fluorescence lifetime for discriminating detector afterpulsing in fluorescence-correlation spectroscopy. *Rev. Sci. Instrum.*, 76:033102(1–5), 2005.

[22] J. Enderlein, T. Ruckstuhl, and S. Seeger. Highly efficient optical detection of surface-generated fluorescence. *Appl. Opt.*, 38:724–732, 1999.

[23] S. Felekyan, R. Kuhnemuth, V. Kudryavtsev, C. Sandhagen, W. Becker, and C. A. M. Seidel. Full correlation from picoseconds to seconds by time-resolved and time-correlated single photon detection. *Rev. Sci. Instr.*, 76:083104(1–14), 2005.

[24] M. Foquet, J. Korlach, W. R. Zipfel, W. W. Webb, and H. G. Craighead. Focal volume confinement by submicrometer-sized fluidic channels. *Anal. Chem.*, 76:1618–1626, 2004.

[25] J. N. Forkey, M. E. Quinlan, M. A. Shaw, J. E. T. Corrie, and Y. E. Goldman. Three-dimensional structural dynamics of myosin v by single-molecule fluorescence polarization. *Nature*, 422:399–404, 2003.

[26] J. T. Fourkas. Rapid determination of the three-dimensional orientation of single molecules. *Opt. Lett.*, 26:211–214, 2001.

[27] S. Fukuzaki, H. Urano, and K. Nagata. Adsorption of bovine serum albumin onto metal oxide surfaces. *J. Ferment. Bioeng.*, 81(2):163–167, 1996.

[28] T. Förster. Zwischenmolekulare Energiewanderung und Fluoreszenz. *Anal. Physik*, 2:55–75, 1948.

[29] Z. Gang, F. Kun, S. Xia, and P. S. He. Elasticity of 10,12-pentacosadiynoic acid monolayer and the polymerized monolayer at varying ph and temperatures. *Langmuir*, 18:6602–6605, 2002.

[30] A. Gennerich and D. Schild. Fluorescence correlation spectroscopy in small cytosolic compartments depends critically on the diffusion model used. *Biophys. J.*, 79:3294–3306, 2000.

[31] A. Gennerich and D. Schild. Anisotropic diffusion in mitral cell dentrides revealed by fluorescence correlation spectroscopy. *Biophys. J.*, 83:510–522, 2002.

[32] R. Golbik, G. Fischer, and A. R. Fersht. Folding of barstar C40A/C82A/P27A and catalysis of the peptidyl-prolyl cis/trans isomerization by human cytosolic cyclophilin (Cyp18). *Prot. Sci.*, 8:1505–1514, 1999.

[33] M. Gösch and R. Rigler. Fluorescence correlation spectroscopy of molecular motions and kinetics. *Adv. Drug Del. Rev.*, 57:169–190, 2005.

[34] F. Güttler, J. Sepiol, T. Plakhotnik, A. Mitterdorfer, A. Renn, and U. P. Wild. Single-molecule spectroscopy - fluorescence excitation-spectra with polarized-light. *J. Lumin.*, 56:29–38, 1993.

[35] T. Ha, T. Enderle, D. S. Chemla, P. R. Selvin, and S. Weiss. Single molecule dynamics studied by polarization modulation. *Phys. Rev. Lett.*, 77:3979–3982, 1996.

[36] T. Ha, T. A. Laurence, D. S. Chemla, and S. Weiss. Polarization spectroscopy of single fluorescent molecules. *J. Phys. Chem. B*, 103:6839–6850, 1999.

[37] M. Haase, C. G. Hübner, E. Reuther, A. Herrmann, K. Mullen, and T. Basche. Exponential and power-law kinetics in single-molecule fluorescence intermittency. *J. Phys. Chem. B*, 108:10445–10450, 2004.

[38] J. Han and H. G. Craighead. Separation of long DNA molecules in a microfabricated entropic trap array. *Science*, 288:1026–1029, 2000.

[39] U. Haupts, S. Maiti, P. Schwille, and W. W. Webb. Dynamics of fluorescence fluctuatuions in green fluorescent protein observed by fluorescence correlation spectroscopy. *Proc. Natl. Acad. Sci. USA*, 95:13573–13578, 1998.

[40] S. W. Hell. Toward fluorescence nanoscopy. *Nature Bio.*, 21:1347–1356, 2003.

[41] S. W. Hell and J. Wichmann. Breaking the diffraction resolution limit by stimulated-emission: stimulated-emission-depletion fluorescence microscopy. *Opt. Lett.*, 19:780–782, 1994.

[42] T. Hirschfeld. Optical microscopic observation of single small molecules, 1976.

[43] T. Hirschfeld. Quantum efficiency independence of time integrated emission from a fluorescent molecule. *Appl. Opt.*, 15:3135–3139, 1976.

[44] T. Hirschfeld. Fluorescence background discrimintaion by pre-bleaching. *J. Histochem. Cytochem.*, 27:96–101, 1979.

[45] H. Hofmann, R. P. Golbik, M. Wunderlich, C. G. Hübner, and R. Ulbrich-Hofmann. Coulomb forces control the density of the globul-state of barstar. *in preparation*.

[46] J. Hohlbein. Einzelmolekülfluoreszenzdetektion an eGFP in hochgeordnetem, porösem Aluminiumoxid. Master's thesis, MPI-Halle, 2004.

[47] J. Hohlbein and C. G. Hübner. Simple scheme for rapid three-dimensional orientation determination of the emission dipole of single molecules. *Appl. Phys. Lett.*, 86:121104(1–3), 2005.

[48] J. Hohlbein, U. Rehn, and R. B. Wehrspohn. In-situ optical characterisation of porous alumina. *Phys. Status Solidi A*, 203:803–808, 2004.

[49] http://probes.invitrogen.com/handbook/sections/0103.html.

[50] C. G. Hübner, V. Ksenofontov, F. Nolde, K. Mullen, and T. Basche. Three-dimensional orientational colocalization of individual donor-acceptor pairs. *J. Chem. Phys.*, 120:10867–10870, 2004.

[51] A. N. Kapanidis, N. K. Lee, T. A. Laurence, S. Doose, E. Margeat, and S. Weiss. Fluorescence-aided molecule sorting: Analysis of structure and interactions by alternating-laser excitation of single molecules. *Proc. Natl. Acad. Sci. USA*, 101:8936–8941, 2004.

[52] J. M. Kim, J. S. Lee, J. S. Lee, S. Y. Woo, and D. J. Ahn. Unique effects of cyclodextrins on the formation and colorimetric transition of polydiacetylene vesicles. *Macromol. Chem. Phys.*, 206:2299–2306, 2005.

[53] T. A. Klar, S. Jakobs, M. Dyba, A. Egner, and S. W. Hell. Fluorescence microscopy with diffraction resolution barrier broken by stimulated emission. *Proc. Natl. Acad. Sci. USA*, 97:8206–8210, 2000.

[54] D. E. Koppel. Statistical accuracy in fluorescence correlation spectroscopy. *Phys. Rev. A*, 10:1938–1946, 1974.

[55] D. E. Koppel, D. Axelrod, J. Schlessinger, E. L. Elson, and W. W. Webb. Dynamics of fluorescence marker concentration as a probe of mobility. *Biophys. J.*, 16:1315–1329, 1976.

[56] Joseph R. Lakowicz. *Principles of fluorescence spectroscopy*. Springer, Berlin, 3rd ed. edition, September 2006.

[57] K. H. A. Lau, L. S. Tan, K. Tamada, M. S. Sander, and W. Knoll. Highly sensitive detection of processes occurring inside nanoporous anodic alumina templates: A waveguide optical study. *J. Phys. Chem B.*, 108:10812–10818, 2004.

[58] T. A. Laurence and S. Weiss. How to detect weak pairs. *Science*, 299:667–668, 2003.

[59] M. J. Levene, J. Korlach, S. W. Turner, M. Foquet, H. G. Craighead, and W. W. Webb. Zero-mode waveguides for single-molecule analysis at high concentrations. *Science*, 299:682–686, 2003.

[60] A. P. Li, F. Müller, A. Birner, K. Nielsch, and U. Gösele. Hexagonal pore arrays with a 50-420 nm interpore distance formed by self-organization in anodic alumina. *J. Apl. Phys.*, 84:6023–6026, 1998.

[61] D. Magde, E. Elson, and W. W. Webb. Thermodynamic fluctuations in a reacting system - measurement by fluorescence correlation spetcroscopy. *Phys. Rev. Lett.*, 29:705–709, 1972.

[62] D. Magde, E. L. Elson, and W. W. Webb. Fluorescence correlation spetcroscopy: 2. An experimental realization. *Biopolymers*, 13:29–61, 1974.

[63] A. Malik, R. Rudolph, and B. Sohling. Use of enhanced green fluorescent protein to determine pepsin at high sensitivity. *Anal. Biochem.*, 340:252–258, 2005.

[64] J. T. Mannion and H. G. Craighead. Nanofluidic structures for single biomolecule fluorescent detection. *Biopolymers*, 85:131–143, 2007.

[65] H. Masuda and K. Fukada. Ordered metal nanohole arrays made by a two-step replication of honeycomb structures of anodic alumina. *Science*, 268:1466–1468, 1995.

[66] X. Michalet, S. Weiss, and M. Jäger. Single-molecule fluorescence studies of protein folding and conformational dynamics. *Chem. Rev.*, 106:1785–1813, 2006.

[67] S. Milon, R. Hovius, H. Vogel, and T. Wohland. Factors influencing fluorescence correlation spectroscopy measurements on membranes: Simulations and experiments. *Chem. Phys.*, 288:171–186, 2003.

[68] W. E. Moerner. New directions in single-molecule imaging and analysis. *Proc. Natl. Acad. Sci. USA*, 104:12596–12602, 2007.

[69] B. K. Müller, E. Zaychikov, C. Bräuchle, and D. C. Lamb. Pulsed interleaved excitation. *Biophys. J.*, 89:3508–3522, 2005.

[70] C. R. Narahari, L. Randers-Eichhorn, J. C. Strong, N. Ramasubramanyan, G. Rao, and D. D. Frey. Purification of recombinant green fluorescent protein using chromatofocusing with a ph gradient composed of multiple stepwise fronts. *Biotechnol. Progr.*, 17:150–160, February 2001.

[71] D. Nettels, I. V. Gopich, A. Hoffmann, and B. Schuler. Ultrafast dynamics of protein collapse from single-molecule photon statistics. *Proc. Natl. Acad. Sci. USA*, 104:2655–2660, 2007.

[72] E. Nir, X. Michalet, K. M. Hamadani, T. A. Laurence, D. Neuhauser, Y. Kovchegov, and S. Weiss. Shot-noise limited single-molecule fret histograms: Comparison between theory and experiments. *J. Phys. Chem. B*, 110:22103–22124, 2006.

[73] M. Ormö, A. B. Cubitt, K. Kallio, L. A. Gross, R. Y. Tsien, and S. J. Remington. Crystal structure of the Aequorea Victoria green fluorescent protein. *Science*, 273:1392–1395, 1996.

[74] N. Panchuk-Voloshina, R. P. Haugland, J. Bishop-Stewart, M. K. Bhalgat, P. J. Millard, F. Mao, W. Y. Leung, and R. P. Haugland. Alexa dyes, a series of new fluorescent dyes that yield exceptionally bright, photostable conjugates. *J. Histochem. Cytochem.*, 47:1179–1188, 1999.

[75] G. H. Patterson, S. M. Knobel, W. D. Sharif, S. R. Kain, and D. W. Piston. Use of the Green Fluorescent Protein and its mutants in quantitative fluorescence microscopy. *Biophys. J.*, 73:2782–2790, 1997.

[76] William H. Press, Brian P. Flannery, Saul A. Teukolsky, and William T. Vetterling. *Numerical recipes in C: The Art of scientific computing*. Cambridge University Press, 2. edition, 1992.

[77] M. Prummer. *Multi-parameter fluorescence spectroscopy: Illuminating single proteins*. PhD thesis, ETH-Zurich, 2002.

[78] M. Prummer, B. Sick, B. Hecht, and U. P. Wild. Three-dimensional optical polarization tomography of single molecules. *J. Chem. Phys.*, 118:9824–9829, 2003.

[79] E. Rhoades, E. Gussakovsky, and G. Haran. Watching proteins fold one molecule at a time. *Proc. Natl. Acad. Sci. USA*, 100:3197–3202, 2003.

[80] R. Rigler, U. Mets, J. Widengren, and P. Kask. Fluorescence correlation spectroscopy with high count rate and low-background - Analysis of translational diffusion. *Eur. Biophys. J.*, 22:169–175, 1993.

[81] R. Rigler and J. Widengren. Ultrasensitive detection of single molecules by fluorescence correlation spectroscopy. *Bioscience*, 3:180–183, 1990.

[82] K. T. Samiee, M. Foquet, L. Guo, E. C. Cox, and H. G. Craighead. Lambda-repressor oligomerization kinetics at high concentrations using fluorescence correlation spectroscopy in zero-mode waveguides. *Biophys. J.*, 88:2145–2153, 2005.

[83] I. Sase, H. Miyata, S. Ishiwata, and K. Kinosita. Axial rotation of sliding actin filaments revealed by single-fluorophore imaging. *Proc. Natl. Acad. Sci. USA*, 94:5646–5650, 1997.

[84] M. Sauer, B. Angerer, W. Ankenbauer, Z. Földes-Papp, F. Gobel, K. T. Han, R. Rigler, A. Schulz, J. Wolfrum, and C. Zander. Single molecule dna sequencing in submicrometer channels: State of the art and future prospects. *J. Biotechnol.*, 86:181–201, 2001.

[85] A. Schoppe, H. J. Hinz, V. R. Agashe, S. Ramachandran, and J. B. Udgaonkar. DSC studies of the conformational stability of barstar wild-type. *Prot. Sci.*, 6:2196–2202, 1997.

[86] B. Schuler. Single-molecule fluorescence spectroscopy of protein folding. *Chem. Phys. Chem.*, 6:1206–1220, 2005.

[87] B. Schuler, E. A. Lipman, and W. A. Eaton. Probing the free-energy surface for protein folding with single-molecule fluorescence spectroscopy. *Nature*, 419:743–747, 2002.

[88] C. Seebacher, C. Hellriegel, F.-W. Deeg, C. Bräuchle, S. Altmaier, P. Behrens, and K. Müllen. Observation of translational diffusion of single terrylenediimide molecules in a mesostructured molecular sieve. *J. Phys. Chem. B*, 106:5591–5595, 2002.

[89] P. R. Selvin. The renaissance of fluorescence resonance energy transfer. *Nat. Struct. Biol.*, 7:730–734, 2000.

[90] E. B. Shera, N. K. Seitzinger, L. M. Davis, R. A. Keller, and S. A. Soper. Detection of single fluorescent molecules. *Chem. Phys. Lett.*, 174:553–557, 1990.

[91] B. Sick, B. Hecht, and L. Novotny. Orientational imaging of single molecules by annular illumination. *Phys. Rev. Lett.*, 85:4482–4485, 2000.

[92] J. Siegel, K. Suhling, S. Leveque-Fort, S. E. D. Webb, D. M. Davis, D. Phillips, Y. Sabharwal, and P. M. W. French. Wide-field time-resolved fluorescence anisotropy imaging (TR-FAIM): Imaging the rotational mobility of a fluorophore. *Rev. Sci. Instrum.*, 74:182–192, 2003.

[93] T. E. Starr and N. L. Thompson. Total internal reflection with fluorescence correlation spectroscopy: Combined surface reaction and solution diffusion. *Biophys. J.*, 80:1575–1584, 2001.

[94] S. J. Strickler and R. A. Berg. Relationship between absorption intensity and fluorescence lifetime of molecules. *J. Chem. Phys.*, 37:814–822, 1962.

[95] K. Suhling, P. M. W. French, and D. Phillips. Time-resolved fluorescence microscopy. *Photochem. Photobiol. Sci.*, 4:13–22, 2005.

[96] K. Suhling, J. Siegel, D. Phillips, P. M. W. French, S. Leveque-Fort, S. E. D. Webb, and D. M. Davis. Imaging the environment of green fluorescent protein. *Biophys. J.*, 83:3589–3595, 2002.

[97] B. R. Terry, E. K. Matthews, and J. Haseloff. Molecular characterisation of recombinant green fluorescent protein by fluorescence correlation microscopy. *Biochem. Biophys. res. com.*, 217:21–27, 1995.

[98] P. Tinnefeld and M. Sauer. Branching out of single-molecule fluorescence spectroscopy: Challenges for chemistry and influence on biology. *Angew. Chem. Int. Edit.*, 44:2642–2671, 2005.

[99] W. Trabesinger. *Optical probing of single-molecule interactions*. PhD thesis, ETH-Zurich, 2002.

[100] R. Y. Tsien. The green fluorescent protein. *Annu. Rev. Biochem.*, 67:509–544, 1998.

[101] M. Vacha and M. Kotani. Three-dimensional orientation of single molecules observed by far- and near-field fluorescence microscopy. *J. Chem. Phys.*, 118:5279–5282, 2003.

[102] M. Wahl, R. Erdmann, K. Lauritsen, and H.J. Rahn. Hardware solution for continuous time-resolved burst detection of single molecules in flow. *Proc. SPIE*, 3259:173–178, 1998.

[103] R. H. Webb. Confocal optical microscopy. *Rep. Prog. Phys.*, 59:427–471, 1996.

[104] S. Weiss. Fluorescence spectroscopy of single biomolecules. *Science*, 283:1676–1683, 1999.

[105] S. Weiss. Measuring conformational dynamics of biomolecules by single molecule fluorescence spectroscopy. *Nat. Struct. Biol.*, 7:724–729, 2000.

[106] J. Widengren, Ü. Mets, and R. Rigler. Fluorescence correlation spectroscopy of triplet states in solution: A theoretical and experimental study. *J. Chem. Phys.*, 99:13368–13379, 1995.

[107] J. Widengren and P. Schwille. Characterization of photoinduced isomerization and back-isomerization of the cyanine dye Cy5 by fluorescence correlation spectroscopy. *J. Phys. Chem. A*, 104:6416–6428, 2000.

[108] B. H. Winkler and R. E. Baltus. Modification of the surface characteristics of anodic alumina membranes using sol-gel precursor chemistry. *J. Membr. Sci.*, 226:75–84, 2003.

[109] T. Wohland, R. Rigler, and H. Vogel. The standard deviation in fluorescence correlation spectroscopy. *Biophys. J.*, 80:2987–2999, 2001.

[110] X. S. Xie and R. C. Dunn. Probing single-molecule dynamics. *Science*, 265:361–364, 1994.

[111] C. Zander, K. H. Drexhage, K. T. Han, J. Wolfrum, and M. Sauer. Single-molecule counting and identification in a microcapillary. *Chem. Phys. Lett.*, 286:457–465, 1998.

[112] C. Zander, J. Enderlein, and R. A. Keller. *Single-molecule detection in solution - Methods and applications*. VCH-Wiley, Berlin/New York, 2002.

[113] M. Zhao, L. Jin, B. Chen, Y. Ding, H. Ma, and D. Chen. Afterpulsing and its correction in fluorescence correlation spectroscopy experiments. *Phys. Appl. Opt.*, 42:4032–4037, 2003.

Eidesstattliche Erklärung

Ich erkläre, dass ich keine anderen als die von mir angegebenen Quellen und Hilfsmittel zur Erstellung meiner Dissertation verwendet habe. Den benutzten Werken wörtlich oder inhaltlich entnommene Stellen sind als solche gekennzeichnet.

Johannes Hohlbein

Halle (Saale), am 05. 11. 2007

Curriculum vitae

Personal data:

name	Johannes Hohlbein
address	Rudolf-Haym-Strasse 14, 06110, Halle (Saale)
date of birth and place	20. Mai 1980, Wippra (Germany)

Education:

09 / 1986 - 07 / 1991	Konrad-Wolf-Schule in Halle (primary school)
09 / 1991 - 07 / 1998	Elisabeth-Gymnasium in Halle, (degree: high school diploma)
08 / 1998 - 08 / 1999	civilian service at Universitätsklinikum Halle
10 / 1999 - 07 / 2004	study of medical physics at the Martin-Luther-University Halle-Wittenberg (degree: Diplom Physiker (Medizinphysik)
09 / 2004 –	phd-student at the Max Planck Institute of Microstructure Physics

Johannes Hohlbein

Scientific contributions

Publications (peer reviewed)

- ”Confined diffusion in ordered nanoporous alumina membranes”, J. Hohlbein, M. Steinhart, C. Schiene-Fischer, A. Benda, M. Hof and C. G. Hübner, Small, 3, 380, 2007
- ”A simple scheme for rapid three-dimensional orientation determination of the emission dipole of single molecules”, J. Hohlbein and C. G. Hübner, Appl. Phys. Lett., 86, 121104, 2005
- ”Recurrence and photon statistics in fluorescence fluctuation spectroscopy”, G. Zumofen, J. Hohlbein, and C. G. Hübner, Phys. Rev. Lett., 93, 260601, 2004
- ”In-situ optical characterisation of porous alumina”, J. Hohlbein, U. Rehn, and R. B. Wehrspohn, Phys. Stat. Sol.(a), 204, 803, 2004

Talks

- ”Up or down? One dimensional diffusion of single molecules in alumina nanopores”, ”5th Prague Workshop on Photoinduced Molecular Processes”, Prague, 2006
- ”Single molecule detection in ordered porous Alumina Membranes”, Picoquant ”11th Workshop on Single Molecule Spectroscopy and Ultrasensitive Analysis in the Life Sciences”, Berlin, 2005

Poster

- ”FRET of individual proteins confined in elongated nanopores”, J. Hohlbein, H. Hofmann, M. Steinhart, E. Hinze, C. Schiene-Fischer, C. G. Hübner, and U. Gösele, Picoquant , ”13th Workshop on Single Molecule Spectroscopy and Ultrasensitive Analysis in the Life Sciences”, Berlin, 2007
- ”Confined diffusion of the enhanced Green Fluorescent Protein in ordered nanoporous alumina membranes”, J. Hohlbein, M. Steinhart, E. Hinze, C. Schiene-Fischer, C. G. Hübner, and U. Gösele, 234th ACS national meeting, Boston 2007
- ”Monte-Carlo simulations of dye-labeled proteins diffusing in nanopores”, J. Hohlbein, M. Steinhart, E. Hinze, C. Schiene-Fischer, C. G. Hübner, and U. Gösele, 234th ACS national meeting, Boston 2007

- ”Confined diffusion in ordered nanopores alumina membranes”, J. Hohlbein, M. Steinhart, C. Schiene-Fischer, A. Benda, M. Hof and C. G. Hübner, Picoquant ”12th Workshop on Single Molecule Spectroscopy and Ultrasensitive Analysis in the Life Sciences”, Berlin, 2006
- ”A simple scheme for rapid 3D-orientation determination of the emission dipole of single molecules”, J. Hohlbein and C. G. Hübner, DPG-Frühjahrstagung, Berlin 2005
- ”Single molecule fluorescence detection on eGFP in ordered porous alumina”, J. Hohlbein, M. Steinhart, C. Schiene-Fischer, U. Gösele, and C. G. Hübner, 334. WE-Heraeus-Seminar ”Biofunctional Interfaces: Basic Science and Applications”, Tutzing, 2004
- ”Towards single molecule detection in artificial nanopores”, J. Hohlbein, U. Rehn, M. Steinhart, R. B. Wehrspohn, and C. G. Hübner, DPG-Frühjahrstagung Regensburg 2004

Scholarship

- DAAD (German Academic Science Exchange) scholarship, September 2005 until February 2006, J. Heyrovsky Institute of Physical Chemistry, Biophysics Group of M. Hof, Prague

Acknowledgment

Die letzten Zeilen dieser Arbeit sind all jenen gewidmet, die mich auf ganz unterschiedliche Art und Weise in den letzten drei Jahren bei meinem Promotionsvorhaben unterstützt haben.

Prof. Ulrich Gösele möchte ich für sein Vertrauen in das Thema meiner Arbeit und damit auch in meine Person herzlich danken. Er gewährte mir unter anderem meinen Wunsch, ein halbes Jahr in Prag zu arbeiten. Prof. Christian Hübner danke ich für seine ansteckende Begeisterungsfähigkeit insbesondere für die Einzelmolekülspektroskopie. In ihm hatte ich zu jeder Zeit einen Ansprechpartner für wissenschaftliche Fragestellungen und weit darüber hinaus. Dr. Martin Steinhart sei gedankt für viele aufmunternde Worte in Zeiten der nahenden Verzweiflung und für immer wieder schnelles Korrekturlesen von Publikationen und Postern.

Silko Grimm und Cornelia Sklarek danke ich für die vielen hergestellten Proben die ich verschleissen musste, bis die Moleküle endlich in die Poren hinein wollten.

Der Arbeitsgruppe von Dr. Martin Steinhart und manch anderem sei gedankt für die freundliche Atmosphäre während der letzten drei Jahre und den Zerstreuungen auch außerhalb der Arbeitszeit (TAB mit den Jungs).

Ein großes Dankeschön auch an die netten Menschen der Infrastruktur am MPI, die dafür gesorgt haben, dass das Internet auf den Computer kommt, dass die Poster rechtzeitig fertig werden und dabei gut aussehen, dass sich mein Konto regelmäßig freut, dass auch von verschollenen Publikationen man noch eine Kopie bekommt und vieles mehr.

Bei Dr. Martin Hof und seiner Arbeitsgruppe möchte ich mich für die freundliche Aufnahme während meines Aufenthalts in Prag bedanken. Die dortige Zeit hat sich trotz oder wegen mancher Annehmlichkeiten als äußerst wichtig für meine Arbeit erwiesen.

Der Arbeitsgruppe von Prof. Christian Hübner danke ich für viele fachliche Diskussionen und natürlich auch für Zerstreuungen auch außerhalb der Arbeitszeit...

Meinen Freunden außerhalb der Wissenschaft sei gedankt für ihre manchmal stoische Ignoranz gegenüber meiner Arbeit.

Zum Schluss möchte ich vor allem meiner Familie danken, die mich immer daran erinnert, dass sich die wesentlichen Dinge dieser Welt nicht in Aluminiumoxidmembranen abspielen.